Title

PHOTOEMISSION, FLUORESCENCE AND PHOTOCHEMICAL STUDIES OF MOLECULAR ADSORBATES ON METAL AND SEMICONDUCTOR SURFACES

Author

Parsons, C.A.

Publication Date

1987-03-01

Lawrence Berkeley Laboratory
UNIVERSITY OF CALIFORNIA

Materials & Chemical Sciences Division

PHOTOEMISSION, FLUORESCENCE AND PHOTOCHEMICAL STUDIES OF MOLECULAR ADSORBATES ON METAL AND SEMICONDUCTOR SURFACES

C.A. Parsons
(Ph.D. Thesis)

March 1987

Prepared for the U.S. Department of Energy under Contract DE-AC03-76SF00098

DISCLAIMER

Photoemission, Fluorescence, and Photochemical Studies of Molecular Adsorbates on Metal and Semiconductor Surfaces

Craig Alan Parsons

Ph.D. Thesis

Lawrence Berkeley Laboratory
University of California
Berkeley, California 94720

March 1987

Photoemission, Fluorescence and Photochemical Studies of Molecular Adsorbates on Metal and Semiconductor Surfaces

by

Craig Alan Parsons

Abstract

Three different pathways have been studied for the relaxation of an optically excited adsorbate/surface system.

The first of these, photoemission, is characterized via the molecular coverage dependence, and time response of the total photoyield. The observed increase in the yield for the initial adsorbed monolayer is attributed to a lowering of the work function of the Ag(111) surface while the monotonic decrease in the photoyield upon further adsorption is interpreted as attenuation of the metal photoelectrons by the multilayers. Evidence of the structural phase transition for pyridine on Ag(111) is seen in both the coverage dependence and photoyield thermal desorption spectra. Long (≈100 ns) photoyield decay times are observed for multilayer films. Models which account for the effects of trapping and diffusion of electrons in the molecular film under the influence of the image potential are discussed.

Radiative emission as a relaxation mechanism for an excited molecule is difficult to observe when adsorbed on a non-insulator surface because of damping by efficient energy transfer to the solid. The first detection of fluorescence from a molecular monolayer on such a surface is reported for the system of tetracene/Si(111). The observed changes in the fluorescence spectrum as a function of

coverage are interpreted in terms of aggregate formation.

Photochemistry is a third path by which an excited adsorbate may relax, although it's reactivity is also expected to be severely limited by competition with nonradiative energy transfer. Photodecomposition for a variety of aromatic molecules adsorbed on roughened Ag surfaces is reported here using continuous radiation in the near-uv/visible. The enhanced fields at the surface provide the driving force for the reaction and also allow it to be monitored via the Raman spectrum of the graphitic carbon product. A 2-photon initial absorption step is implicated by the intensity dependence of the decomposition rate for most cases. Energy transfer considerations and possible decomposition mechanisms following absorption are discussed.

Table of Contents

Acknowledgements

I wish to thank my research director, Charles Harris, for support and especially for his unique style in maintaining this research group. Although admittedly frustrating at times, I have profited by learning to think both creatively and critically in scientific evaluations. This group has been the source of several very good friends as well as some truly amazing scientists. Paul Alivisatos shared an office with me, and was always willing to wrestle with a scientific problem. Dor Ben-Amotz was similarly very helpful. I have great respect for Alex Harris and Mark Berg for the example they provided. Gary Goncher was my co-worker on the surface photochemistry project, and introduced me to the lab. Jack Morgan helped in the initial set-up of the photoemission experiment. Keenan Brown is a store-house of knowledge, and he contributed to the modelling of the experimental photoemission data. Dan Russell, Walt Merry, Mike Arndt, and Michael Prisant could usually be persuaded into spending an afternoon discussing a troublesome scientific point. Thanks to all the rest of the Harris group for putting up with my psychotic behavior during the writing of this thesis, and to Mark Paige and Karen Schultz for the great going-away present. The skilled employees of the Department also deserve mention, specifically Marcia Bogart, who more than once expedited purchase orders Friday at 3 pm.

There are of course many others who are responsible for my random-walk which brought me to this point. I owe, and thank, my parents for everything. My high school science teacher, Mrs. J.

Heiden achieved the impossible by teaching at the introductory level and still conveying the intrinsic excitement involved in science. Finally, I thank Ruth (-Ann) who supported me through countless lab difficulties, and made it worthwhile living in the Bay Area for 5 years.

This work was supported by the Director, Office of Energy Research, Office of Basic Energy Sciences, Chemical Sciences Division of the U.S. Department of Energy, under Contract No. DE-AC03-76F00098.

Chapter 1.

Adsorbate Induced Changes in Photoemission

I. Introduction

Although the subject of study for many years, the behavior of electrons in condensed matter is still receiving considerable attention as evidenced by some very recent work.[1] As an example, the question of trapping of electrons by water is one subfield with which much current theoretical and experimental work is concerned.[2] The system studied here is thin films of molecular adsorbates condensed on a Ag(111) surface. Low energy electrons are generated via photoemission from the metal at energies just above the work function with both pulsed and continuous radiation. This configuration has been used in the past, especially with respect to determination of a characteristic attenuation (or mean free path) of the photoemitted electrons by the film.[3,4] Usually relatively thick films were studied. The data presented here is for film thicknesses ranging from zero to tens of monolayers. At these low coverages, i.e. for the initial monolayer, the photoyield data is sensitive to the change of the work function caused by adsorption. This fact has been documented by the surface science community,[5] but the studies have not, in general, been extended to the multilayer regime. This of course can only be accomplished for physisorbed layers; most of the surface studies are concerned with chemisorbed molecules for which multilayers don't exist. The other unique contribution presented here is time-resolved photoyield data, which reveals that a small population of electrons survive in the film for very long times (hundreds of nanoseconds) after the photoexcitation. In light of the very strong image potential which exists for an electron near a

metallic surface, this is a surprising result.

This work will be divided into four remaining parts. Parts II and III are reviews of the two main areas implicated by this data: electrons in condensed phases, and work function shifts upon adsorption. In part IV the experimental procedure is given, and part V is the presentation and discussion of the results. Finally, part VI summarizes the conclusions.

II. Review of Low Energy Electrons Interactions in Condensed Phases

A. Studies in Condensed Films

The topic of electrons in condensed phases is a very old one dating from the first studies of alkali metal ammonia solutions in the 1800's. After many years of experimental and theoretical work from a variety of different angles, there are still a great many basic questions awaiting answers. The types of scattering processes an electron will encounter in a molecular solid or liquid, their energy dependencies, and especially the dynamics of such mechanisms are, to a large extent, still under discussion and in some cases have not yet been thoroughly investigated. A summary of some of the pertinent work will be given here. No attempt has been made to include studies using electron energy loss spectroscopy (EELS), where an incident monochromatized electron beam is energy analyzed after scattering from a molecular layer to determine the characteristic losses. This technique is now used routinely to observe vibrational and sometimes electronic transitions of adsorbed molecules. Experiments where the total yield of scattered electrons is collected

will be focussed on here. These experiments consist largely of electron transmission experiments which have been performed on condensed molecular films, and photoconductivity measurements and the related theory of trapping, done mostly on bulk liquids and solids. This review will be divided between these two areas.

A technique known as low energy electron transmission spectroscopy (LEETS), developed independently by Hiraoka[6] and Sanche,[7] has provided the best information to date on the interaction of low energy electrons with condensed molecular films. LEETS is just the extension of gas phase electron transmission spectroscopy to condensed phase. A beam of electrons is directed at an electrically isolated metal substrate cooled to 77 K onto which the film has been condensed. The current transmitted through the film to the substrate is monitored as the energy to the electron beam is swept, typically between 0-15 eV. Hiraoka[8] simply uses an electron gun as his excitation source, but Sanche achieves higher resolution by employing a trochoidal monochromator resulting in an electron beam of 10^{-9} A with a FWHM of 40 meV.[7] A schematic of Sanche's apparatus is shown in Figure 1.

While the data obtained in these experiments show many interesting features, it is not trivial to relate the observed spectral structure to their underlying physical events. The transmitted current has contributions from electrons that have undergone both elastic and inelastic collisions in the film, as well as a portion of unscattered electrons. In gas phase experiments of this type, this ambiguity can be removed by biasing the detector to measure only the elastically scattered electrons, for example. This

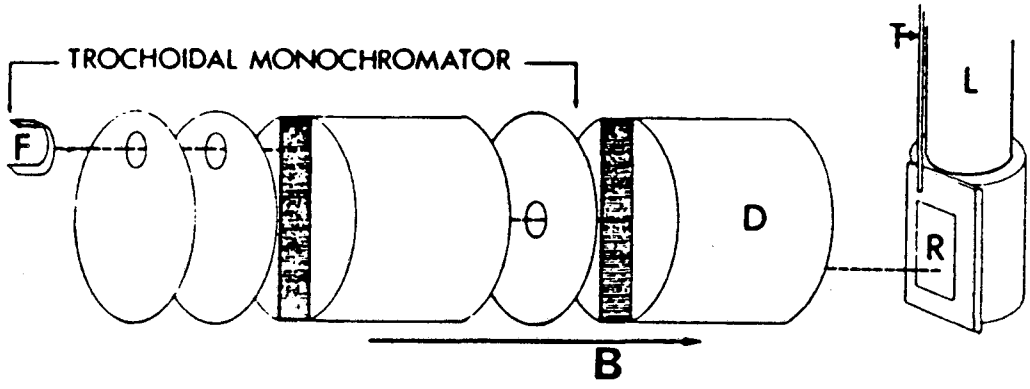

XBL 872-508

Figure 1. The set-up used by Sanche for low energy electron transmission spectroscopy. Electrons emitted by filament F are monochromatized and then pulled off axis by the crossed E and B fields in D before impinging on the molecular film condensed on the metal ribbon R. The metal surface is cooled by the cryotip L from which it is electrically insulated. Molecules are dosed through tube T. The transmitted current to the metal ribbon is detected as a function of the incident electron energy. From ref. 7.

separation is not possible for the transmitted current through a film, and thus the data is more difficult to interpret. Manifestations of inelastic losses will be considered first.

Sanche reasons[7] that because electrons suffering inelastic losses will be at lower energy, their probability of reflecting back out of the film will decrease. Thus inelastic losses are expected to contribute to an increase of the transmitted current (I_t). His plots of I_t vs. electron energy (V) show broad maxima with much smaller features superimposed. These small peaks are enhanced by displaying $-d^2I_t/dV^2$ vs. V, the physical meaning of which will be discussed below. Hiraoka has compared transmitted to back-reflected (I_r) currents for several systems. He has shown that for plots of dI_r/dV vs. V losses in the film are represented as minima, and observes that the curves dI_r/dV and dI_t/dV vs. V are "mirror images" of each other. The conclusion is that inelastic film losses will show up as maxima in plots of dI_t/dV vs. V. He cautions, however, that only sharply resonant structure can be interpreted as energy losses. In addition, Cheng and Funabashi[9] have pointed out that relating these maxima to inelastic events is only valid as long as the elastic scattering cross section remains relatively constant, since elastic processes also affect the total transmitted current.

Despite these precautions, LEETS has been shown to display features which correlate to gas phase molecular transitions. Hiraoka first reported[8] this for four aromatic molecules - one of which, benzene, has become the classic test case for this method. Sanche later duplicated this work, assigning six states in the range of 3.9-7.0 eV by comparison to gas phase threshold electron impact

data.[7] A LEETS spectrum of condensed benzene is shown in Figure 2, along with the gas phase spectrum for comparison. Excitation of optical transitions by electrons takes place via the long-range dipole potential. Optical selection rules are relaxed, however, and forbidden transitions such as triplet state excitations are allowed by spin exchange, often with much larger cross sections than singlets.[10] The correspondence to gas phase spectra has not been observed for saturated compounds such as pentane and cyclohexane. Sanche has noted[11] a lack of structure and broader peaks for these molecules, and advances a theory to explain this which will be presented below.

Perhaps as a consequence of their slightly different data collection techniques, Sanche's and Hiraoka's data differ, leading to opposing interpretations and assignments. Although, as mentioned already both workers assign benzene transmission peaks to gas phase transitions, they each do so with a different shift of the electron energy scale with respect to the gas phase spectra.

Hiraoka is able to assign this shift directly to a physical parameter V_0, the energy of a quasi-free electron in the film.[10] V_0 is related to the bulk electron affinity of the film, and is defined as the energy difference between the vacuum level and the conduction band of the organic film. Reported V_0's are typically on the order of 1.0 eV. Negative values of V_0 indicate that electrons in the film are at energies below the vacuum zero. Experimentally, a negative V_0 is determined from the alignment shift required in comparing the film peaks to gas phase data. Positive V_0's create a barrier for the electron entering the film from the vacuum. This is manifested in

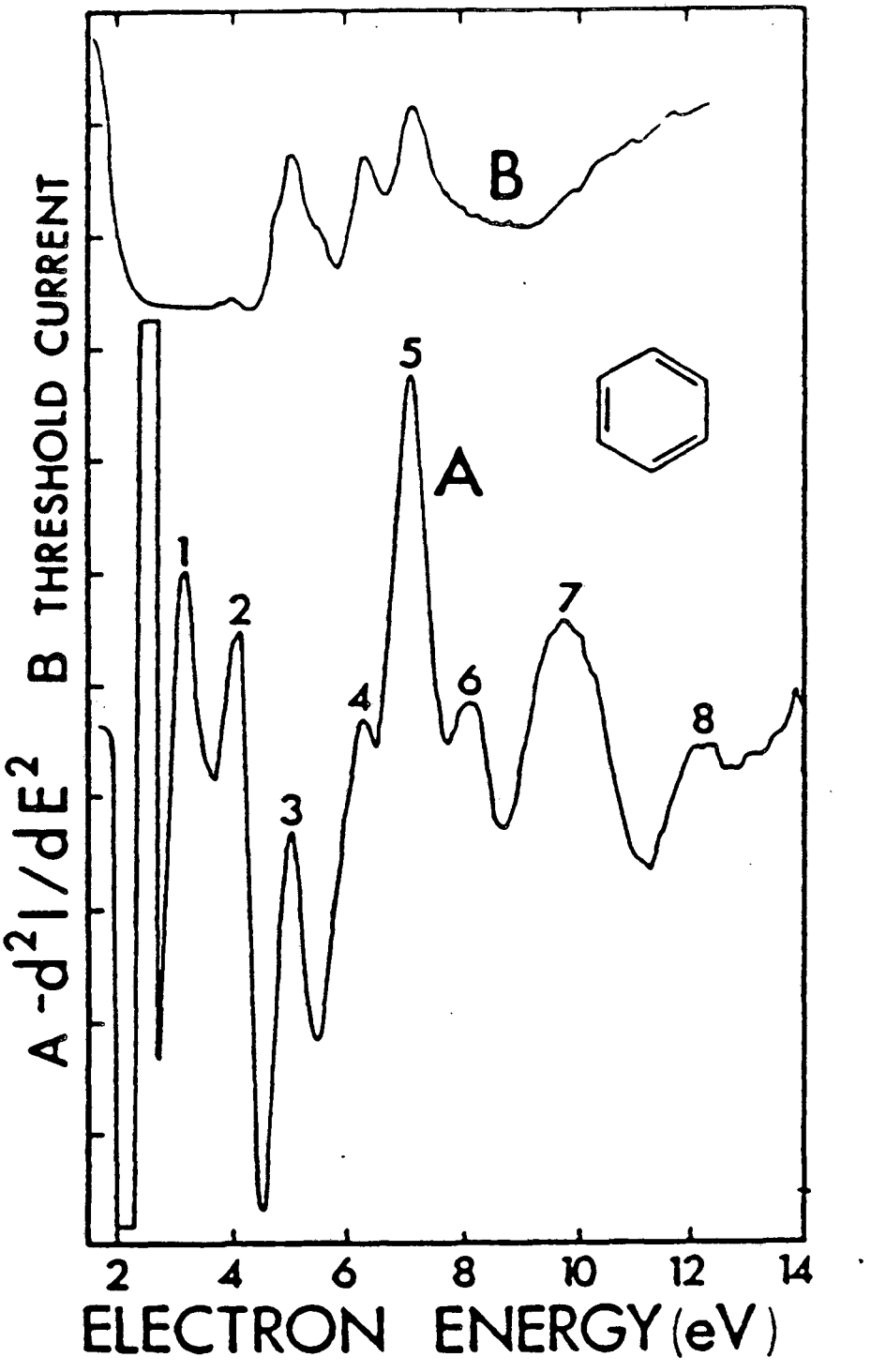

XBL 872-512

Figure 2. A LEETS spectrum (A) for a condensed film of benzene compared to similar data (B) taken in the gas phase. Features 2-5 in (A) correspond to peaks also seen in (B). Features 6-8 were also assigned to benzene transitions. From ref. 7.

the spectra by the growth of a second electron injection peak with increasing film coverage, shifted by V_0 from the bare metal injection peak (the "zero" energy peak). Thus Hiraoka can determine both positive and negative values for V_0. The results are quite interesting: the aromatic molecules tested have negative values of V_0, and therefore have an additional means of trapping sufficiently low energy electrons in the film, while almost all other molecules had positive values. These trends are generally reflected in the liquid phase values of V_0 (no other measurements exist for the solid phase) which Hiraoka presents[12] for comparison.

Returning to benzene as an example, Hiraoka obtains a V_0 (or alignment shift) of -0.3 eV. Sanche reports a shift of 2.25 eV to bring his spectra into coincidence with those from gas phase experiments.[7] In an attempt to understand this shift, Sanche[11] proposes the formation of electron-exciton complexes as an explanation of the molecular-related resonances. These complexes correspond to core-excited negative ion resonances - the capture of an electron by an excited state molecule. He supports this theory by using a Wigner-Seitz (WS) model of the molecules as close-packed spheres each having a potential which is the sum of an infinite "hard core" and a longer range dipole potential which is screened outside the sphere. To consider the total potential within one WS sphere, the screened part of the dipolar potential must be summed over all neighboring spheres. This results in the polarization of a given sphere through the influence of its neighbors. Solving this problem variationally with a trial wave function and appropriate boundary conditions results in a ground state energy E_0 = -1.6 eV, when

parameters for benzene are used. A Frenkel exciton is now added to the picture via the addition of some fraction of the same dipole potential used for the ground state calculation. The variational calculation is repeated to see what effect the proximity of the exciton has on the total ground state energy. The new energy for the complex is found to be E_c = -2.2 eV, therefore the electron is bound to the exciton by 0.6 eV. E_c is also the shift required to bring the condensed phase spectra into coincidence with the gas phase values, which is in remarkable agreement with Sanche's observed shift of 2.25 eV. Although admittedly crude (it assumes crystalline order, while the organic films are known to be amorphous), the WS model appears successful at explaining many of the observed features of Sanche's data. The model predicts that the binding energy (E_0-E_c) of the complex is proportional to the molecular polarizability, thus molecules with more polarizable π orbitals should show more structure due to molecular resonances, which also agrees with experiment. Finally, the energy of the complex E_c in the WS model goes inversely with the "hard core" diameter, and the data shows that for larger molecules the alignment shift required to match gas phase results does indeed become smaller.

Caron and Bader[13] strengthen the electron-exciton complex theory by proving that maxima in the transmitted current are consistent with excitation via creation of a complex. Using the same kinetic equation approach as will be outlined in the discussion below of mean free path (MFP) determinations, they confirmed that either a longer MFP for the complex compared to the free electron, or a larger vacuum/film interface reflection coefficient for the complex compared

to the electron leads to a transmitted current maximum.

The results discussed above have been concerned with transmitted electron current features which primarily occur at greater than 1.5 eV, which Sanche calls the molecular regime. Below 1.5 eV, in the 'collective regime', Sanche and Hiraoka again offer conflicting theories to explain the observed structure. Hiraoka[14] has compiled an impressive list of peaks observed for seven aromatic molecules and finds correspondences between many of these and gas-phase temporary negative ion resonances. These so-called "shape" resonances are the result of the capture of an electron by the ground state of a neutral molecule (this is contrasted with the core-excited resonance mentioned above). For a typical molecule with a negative electron affinity the resulting negative ion is unstable, and estimated lifetimes are 10^{-12} to 10^{-15}s. These states have been well documented by gas-phase electron transmission experiments.[15] Most of the features assigned by Hiraoka as due to negative ion resonances occur in the < 1.5 eV range, although some as high as 5 eV were assigned on the basis of their correspondence to gas phase results. There still remain undetermined peaks, and in one case a gas phase negative ion resonance is observed with no corresponding feature in the film data. He suggests that since transmission peaks reflect the states of the conduction band, the observation of negative ion resonances shows that the vacant molecular orbitals are responsible for forming the conduction band upon condensation.

Sanche[7] has a much different view of these low energy bands. He argues against the existence of negative ions based on the fact that such resonances have never been reported for saturated molecules in

the gas phase, but similar structure is still observed in the low energy region for condensed phase electron transmission experiments. He also finds that these low energy peaks appeared only at higher film thicknesses, and were dependent on such experimental parameters as the deposition rate, and beam position.[11] Sanche also claims to be able to find correspondences between condensed and gas phase negative ion data for only a couple of the molecules tested. Instead, he suggests that these peaks are due to structure-related coherent scattering effects. The reasoning is based on the results of Cohen-Lekner[16] scattering theory which states that the differential elastic scattering cross section will be given approximately by the product of the cross section per molecule with a structure factor which reflects the order of the scattering system. That a structure sensitive factor should be important correlates with the deposition rate dependence, and was also suggested earlier by Cheng and Funabashi.[9] Sanche was able to predict resonances in this low energy region with a calculation using a known structure factor of a liquid. Dramatic effects of structure sensitive elastic scattering have been presented by Perluzzo et al..[17] For inert gases there exists a wide range of electron energies (< 8 eV) in which no inelastic events can occur. In this region, strong structure was observed in the LEETS spectra that changed with deposition of the first few monolayers. These peaks were interpreted as interference phenomena from coherent electron reflection from the two interfaces of the film. A theory to quantitatively relate both inelastic and elastic events to transmission spectra will now be reviewed.

The model discussed here is that of Chantry et al.[18], revised to

apply to condensed films by Bader et al..[19] The key assumption is to treat the scattering of electrons in all directions with a one-dimensional model of just two counter-propagating currents, which is referred to as the two-stream approximation. This allows two simple kinetic equations to be written for each type of process (i.e. unscattered, elastically scattered and unscattered electrons), where the transitions between the various processes are controlled by a cross section, which is the inverse of the mean free path (MFP). For example, the elastic electron population moving in the +x direction is depleted by both elastic and inelastic events, but supplemented by elastic scattering from the population moving in the -x direction, and also by elastic scattering from previously unscattered electrons. The equation is:

$$(1) \qquad \frac{dI^+}{dx} = -\epsilon \left[\frac{1}{2l_e} + \frac{1}{l_i} \right] I^+ + \frac{\epsilon}{2l_e} I^- + \frac{1}{2l_e}(S^+ + S^-)$$

where e is a parameter between 1 and 2 relating to the two-stream approximation, le is the elastic MFP, I is the elastic electron population and S is the unscattered electron population. Three pairs of such coupled linear differential equations are generated which must be solved under the appropriate boundary conditions for the film. These deal with the reflection conditions at the vacuum/film (R) and the film/metal interfaces. The solution for the transmitted current is the sum of the unscattered, elastic, and inelastic currents. Bader's final solution is rather complex, but certain limits will be discussed. For the constraints of no inelastic losses, and no reflection of the unscattered beam at the film/metal

(R') interface, the transmitted current becomes:

$$(2) \qquad I_{trans}(th) = I_0 \frac{\rho'(\rho + 1) - \rho(\rho'-1)e^{-th/l_e}}{\rho + \rho' + \rho\rho' th/l_e}$$

where $\rho = \epsilon(1-R)/(1+R)$, $\rho' = \epsilon(1-R')/(1+R)$, and th = film thickness. All of the parameters may be electron energy dependent. This equation has both an exponential and inverse dependence on the film thickness. For the opposite case, where the inelastic losses dominate ($l_i \to 0$), the transmitted current equals the incident current, as expected, since none of the electrons entering the film is permitted to reflect back out. Finally, in the large thickness limit I_t will depend only on l_i, i.e. it becomes thickness independent, a result which corroborates the experimental observation of constancy of the spectral features for multi-layer films.

Bader et al.[19] use the full equation to fit the data for Xe films. This data is for much thicker films than the interference reflection phenomena mentioned earlier.[17] They find the data fit well using only an elastic MFP when below the first transition in Xe at 8 eV. The results for the energy dependence of the elastic MFP determined by such a fit are shown in Figure 3. The surprising result is that below 2 eV the MFP rises quickly to hundreds of angstroms. They speculate that although their assumption of no specular reflections becomes worse as the electron energy drops, the rise in MFP is a real effect, as is also seen in gas phase measurements. This trend can be qualitatively explained as a consequence of the film appearing more continuous as the wavelength

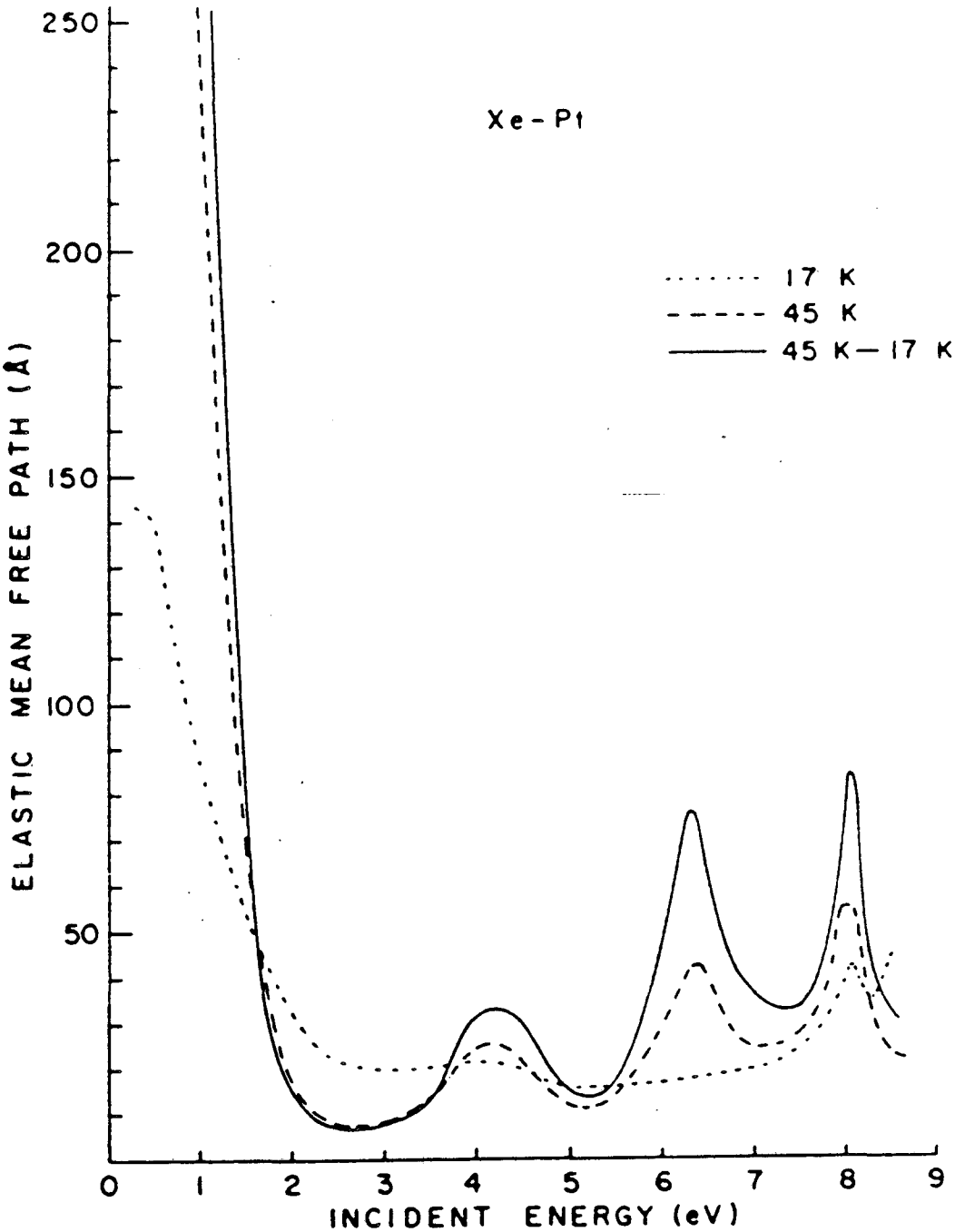

XBL 872-511

Figure 3. The energy variation of the MFP as determined by a fit of eqn. (2) to LEETS data for Xe films by Bader et al.. The structure between 2-8 eV is attributed to variation of the effective mass of the electron in xenon. Note the large increase in MFP for low energy electrons. From ref. 19.

of the electron increases. This result shows that MFP's can be highly energy dependent, especially at low energy.

Returning to Figure 3, the structure seen by Bader et al. in the MFP between 2-8 eV has since been explained in a recent paper by Plenkiewicz et al..[20] They find that the energy dependence of the effective mass as calculated from the Xe band structure, fluctuates considerably over the same 2-8 eV region. In fact they are able to reproduce the observed energy dependence of the MFP utilizing a theory for electron scattering by phonons. Another observation of phonon-mediated MFP's will be described below.

In another MFP determination Sanche[7] fit his benzene data to eqn. (2) at 3.3 eV where he considered the losses to be only elastic. He obtained a good fit for a MFP l_e = 7 Å. It should be noted that for inelastic losses (in this case due to excitation of an electronic benzene transition), Sanche found the peak intensity of the transmission curve to be insensitive to coverage and could not be fit with eqn. (2). The entire spectral range for benzene of 0-10 eV was fit separately by Goulet and Jay-Gerin[21]. Their theoretical procedure employed an energy-independent MFP, but used a Monte Carlo algorithm for applying the various collisional processes weighted appropriately. A value of 8 Å was found for benzene's MFP, in good agreement with Sanche's result at 3.3 eV. Comparisons will now be made to other literature determinations of electron MFPs.

Much of the early work on electrons in molecular films was carried out by photo-injection experiments. That is, electrons were produced via uv-excited photoemission from a suitable substrate. Typically the total yield of emitted electrons was collected and

monitored versus successive deposition of a film on the emitting substrate. One problem with such an arrangement is the broad energy spread in the photoemitted electrons due to production of secondary electrons during the emission process. If Sanche's fitted data is correct, there could be large differences in the MFP for electrons at energies of < 2 eV. Another difficulty is distinguishing between the electrons from the substrate and electrons possibly generated in the molecular film itself. This of course depends on the relative photoemissive yields of the film versus substrate at the excitation wavelength used.

Table 1 summarizes the measurements that have been made of MFPs in condensed organics with low energy electrons. The first four of these entries are photo-injection experiments. Most of these workers analyzed their data assuming an exponential dependence of the yield on the film thickness. Referring back to eqn (2), which described the transmitted current (or electron yield) for the case of only elastic losses, it can be seen that the yield becomes an exponential function of film thickness in the limit $\rho' - 0$. This requires $R' = 1$, which states that only those electrons which haven't suffered any collisions may be collected in the transmitted current. Thus it seems a little surprising that a simple exponential fit works so well, since it carries with it the restriction of only elastic collisions, and that only unscattered electrons can emerge from the film. Several workers did see deviations at larger thicknesses, however, which may indicate a breakdown of these assumptions. When observed, these discrepancies at larger thicknesses were attributed to a variety of effects such as photoelectron production in the film

TABLE 1. Summary of electron photoinjection MFP determinations

Molecule	Photon Energy (eV)	Electron Energy (eV)	MFP (A)	Comments	Ref.
Cu-phthalocyanine	7.8	1.5	11.	yield measurement CuI substrate, 300 K	23
n-pentane	4.8, 6.7	< 2.	45.	yield measurement Ag, Au substrate, 77 K	3
cyclopentane			39.		
neopentane			82.		
n-hexane			18.		
cyclohexane			25.		
neohexane			30.		
3-methyl pentane			24.		
heptane			13.		
octane			12.		
nonane			7.		
2,3 dimethyl pentane			19.		
1-pentene			26.		
1-hexene			12.		
pentacene	7.75		75.	yield measurement CuI substrate, 300 K	22
napthacene			75.		
perylene			800.		
coronene			250.		
violanthrene			13.		
Cu-phthalocyanine			27.		
napthacene	7.75	0-2.47	150.	crude energy analysis of electrons; CuI substrate, 300 K	29
		0.4-2.47	140.		
		0.9-2.47	120.		
		1.4-2.47	120.		
		1.9-2.47	100.		
	8.61	0.-3.33	110.		
		0.8-3.33	100.		
		1.3-3.33	90.		
		1.8-3.33	80.		
perylene	7.75	0.-2.38	360.		
		0.4-2.38	360.		
		0.9-2.38	370.		
		1.4-2.38	350.		
		1.9-2.38	350.		
	8.16	0.-2.79	360.		
		0.8-2.79	340.		
		1.3-2.79	340.		
		2.3-2.79	280.		
ferrocene	21.2	0.4	60.	energy analyzed emitted electrons; Au substrate, 77 K	26
		1.5	23.		
		5.6	7.2		
		14.6	3.0		
		16.2	2.4		
TTF	10.2	5.8	0.7 ML[a]	energy analyzed emitted electrons; Au substrate, 77 K	24
TCNQ		4.7	0.49		
		2.7	0.65		
TTF-TCNQ	5.5-11.8		< 10.	energy analyzed emitted electrons; Au substrate, 77 K	25
napthacene (tetracene)	4.43, 5.9	≈1.	6.-10.	energy analyzed emitted electrons; Ag substrate, 120 K	28
hexatriacontane $n\text{-}C_{36}H_{74}$	4.4-6.8	2.0	46.	energy analyzed emitted electrons; Pt,Ir substrate, 300 K	27
		0.5	29.		

[a]ML=monolayer

or a physical change in the film structure itself.[25]

A slightly different approach to the analysis of yield vs. film thickness data is taken for the data shown in the second entry in Table 1.[3,4] These authors view the data as a reflection of the steady-state spatial distribution of electrons along the surface normal in the film. They consider both an exponential and a Gaussian distribution; it can be shown that the exponential spatial distribution leads to an exponential dependence of yield on film thickness, while the Gaussian spatial distribution results in an error function dependence relating these parameters. They find the exponential function to fit the data best, and that is the one for which MFPs in Table 1 are shown for. Chang and Berry[3] also have obtained some electron energy dependent MFP data and find that for all the molecules studied, the cross section for scattering electrons of < 1 eV is somewhat larger than the scattering cross section for < 2 eV electrons.

More data concerning the dependence of the MFP on the electron's energy has been collected in experiments which energy analyze the photoejected electrons. The trend, agreeing with that observed by Chang and Berry, is longer MFP's for lower energy electrons. The most dramatic demonstration of this is in the data of Ritsko et al.[26] on ferrocene, where the MFP was observed to vary between 2.4-60. Å over the energy range of 16.2-0.4 eV. This again suggests that the dependence on energy may be especially pronounced for low energy (< 1 eV) electrons.

A different interpretation is given by Pfluger et al.[27] for their energy-resolved MFP data on attenuation by a 36 member alkane

deposited on Pt and Ir surfaces. They include scattering by LO-phonons, a mechanism they feel will be dominant for polymeric dielectrics. Their analysis, which involves solving a simplified form of the Boltzmann equation, predicts that exponential attenuation with film thickness should only be realized at large thicknesses. Experimentally they observe exponential attenuation for thicknesses greater than 80 Å. In the kinetic energy range of 0.5-2.0 eV they observe MFP's of approximately 35 Å. However, they see a slight increase (< factor of two) in MFP from 2.0 to 0.5 eV which they attribute to the expected resonance with the phonon at 0.36 eV. This is opposite to the other results discussed thus far where lower energy electrons were found to have longer MFP's.

Grechov[28] makes an argument in an attempt to account for some of the apparently large deviations which exist in the MFP data as demonstrated in Table 1. His data for napthacene, shown in the second to last entry of Table 1, had to be taken on films prepared at 120 K to ensure that the film was homogenous and did not grow via island formation. Grechov maintains that MFP's are on the order of a molecular monolayer, and MFP values obtained at room temperature (such as the result of Hino and Inokuchi[29] who obtained a MFP of ≈100 Å for napthacene), may be erroneously too large because of inhomogeneous film growth which leaves areas of bare substrate exposed even after several "monolayers" have been deposited. This observation taken together with the possibility of a sharp dependence of the MFP on electron energy should be considered when attempting to compare the results from the different experiments collected in Table 1.

B. Bulk Solid and Liquid Studies

A considerable body of data concerning the interaction of low energy electrons with molecular condensed phases dates from G.N. Lewis' work in the 1940's. These investigations have proceeded through basically two types of experiments. The first is photoconductivity, whereby light is used to excite excitonic transitions of the bulk, or in some cases in combination with the photoejection of electrons from a contact electrode, as discussed in the experiments above. The sample is usually sandwiched between two electrodes and the current across them monitored as a function of time after a light pulse. A time of flight effect for arrival of the charge carriers at the far electrode is observed and the time delay (τ) for build-up to a constant current is interpreted as a measure of the mobility (μ) of the generated charge carriers, given as[30]:

$$\mu = \frac{d^2}{V \tau} \tag{3}$$

where d is the gap between the electrodes, and V the applied voltage. The term "charge carriers" is used here since when excitons are formed there is both a positive ionic carrier as well as the electron. In liquid studies separate mobilities associated with each are observed, but in glasses at 77 K the ionic motion is frozen out and the electron is left as the remaining mobile charge carrier. This situation still differs somewhat from the photoinjection studies discussed previously since the field of the ionic "hole" is also felt by the electron, and may limit its excursion in the bulk.

A second method for investigating electrons in condensed phases is pulse radiolysis. Irradiation of a sample with γ or x rays, or even electrons, produce high energy electrons in the sample which eventually lead to secondary electrons of low energy. The information from these studies comes primarily from spectroscopy of the electrons themselves. Optical spectroscopy reveals broad absorptions in the near infrared extending well into the visible which have been assigned to unbound electrons. An example of such a spectrum is shown in Figure 4. The changes of the electron's spectral response with respect to applied field, light intensity, and bleaching effects are used to follow the electrons in time after the pulse radiolysis. ESR and differential thermal analysis have also been successfully used to characterize the electron population.

The results from both types of experiments focus on one central point: the electrons are seen to move slowly through the bulk medium due to the presence of energy states which are capable of capturing the electron for some period of time. These states are called traps, or sometimes in the case of a liquid, equilibration of the electron with the trap states is referred to as solvation. Since traps are postulated to be responsible for most of the observed phenomena of electrons in condensed phase materials, a large number of models exist relating the details of the electron trapping process. A review of these models will now be given along with an attempted reconciliation of these ideas with the resonant scattering and loss mechanisms proposed by Sanche and Hiraoka in the last section.

The most general classification of traps has been given in a review by Lesclaux and Jussot-Dubien,[31] where they divide traps into

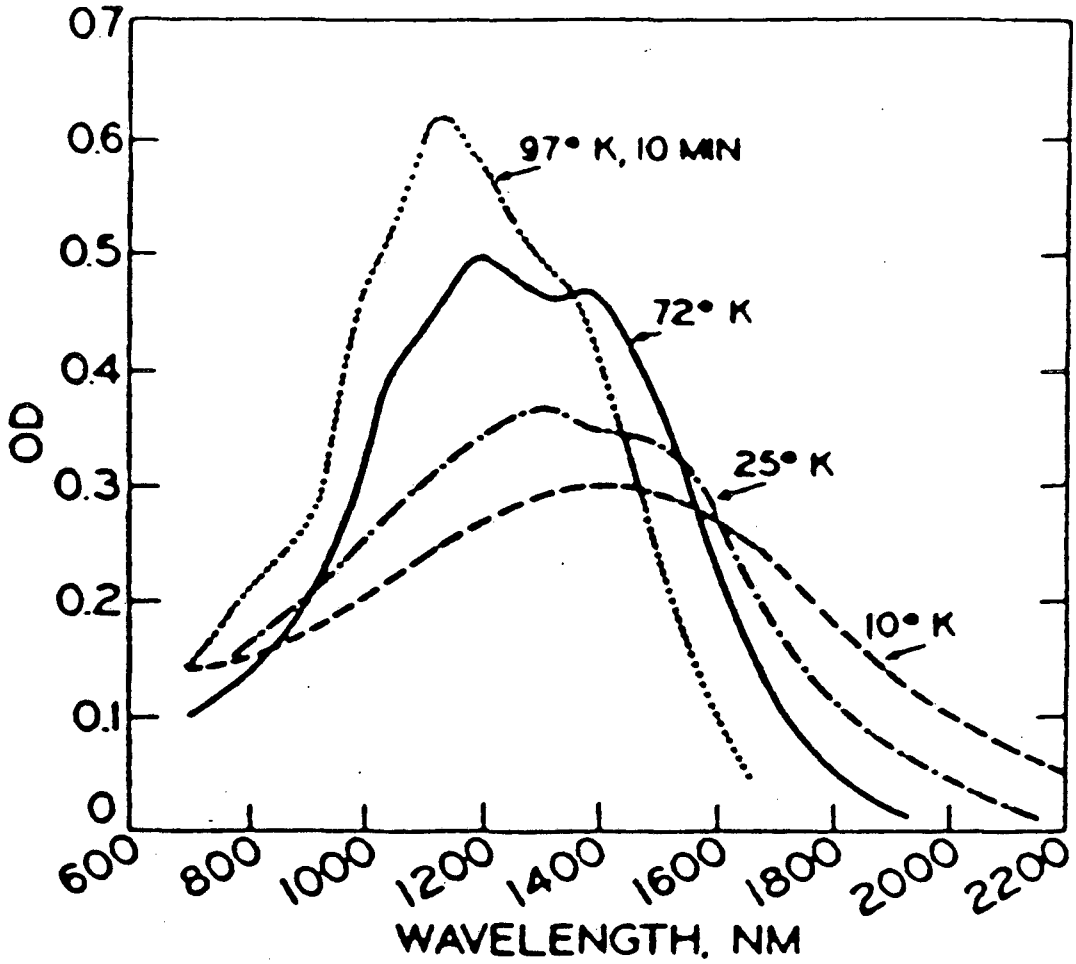

XBL 872-516

Figure 4. Absorption spectra of trapped electrons in 2-methyltetrahydrofuran (MTHF) produced by photoionization, at various temperatures. The electrons are very long-lived - these spectra were taken several minutes after the ionization. From ref. 39.

chemical and physical categories. Chemical trapping requires the presence of another species to act as an electron acceptor. Although postulated to represent a scavenger molecule or an impurity, the resonant molecular losses reported by Sanche and Hiraoka would presumably fit into this category. Physical traps refer to states created by the presence of the matrix structure itself, or matrix-molecule interactions. Such a description would include trapping at sites like crystal imperfections, grain boundaries, and the empty states associated with the surface itself.[30]

Perhaps the most widely accepted explanation of trapping is that of the electron interacting with the bulk polarization of the medium to provide a stable, low energy site. This idea was quantitatively modelled by Jortner in 1959.[32] Borrowing on an idea from Landau, he calculated bound energy levels for an electron in a spherical cavity immersed in a continuous dielectric medium. This model has become known as the "electron digging it's own hole" interpretation since it relies on no previously existing matrix conditions - merely the fact that the electron exists in the dielectric. Jortner defines a permanent polarization P_D of the bulk by the charged cavity as:

$$P_D = \frac{e}{4\pi r^2}\left[\frac{1}{D_{op}} - \frac{1}{D_s}\right] \tag{4}$$

where D_{op}, D_s are the optical and static dielectric constants. Thus the permanent polarization is that part of the total polarization which can't follow the motion of the electron, and this creates the potential well. Jortner finishes with a variational calculation of the bound state energies assuming a hydrogen-like trial wave

function. He was able to explain some of the features of the optical absorption of alkali/ammonia solutions with this simple picture.

Repeated attempts to improve on Jortner's basic theory have appeared.[33] One of the more rigorous calculations is that of Fueki et al.,[34] where the application is now to irradiated organic glasses at 77 K. They improve the model by allowing the first solvation sphere around the cavity to interact via a short range dipole potential, while all others past this first shell are represented by a bulk dielectric constant as before. They also allow theoretically for incomplete alignment of the dipoles around the charge cavity and in this manner are able to account for the blue shift seen in the optical absorption upon warming from 4 K to 77 K. This suggests that the shift on warming is due to a more complete dipole stabilization of the electron by the more facile movement of the solvent molecules.

While many features of the trapped electron's absorption profile were successfully explained, the theories of Jortner, and later Fukei, failed to reproduce the broad width and extended high energy tail of the spectra. This prompted Funabashi, Carmichael and Hamill[35] to propose quite a different formulation of the problem in 1978. In their theory the absorption of light by a trapped electron is responsible for moving that electron into another solvent site. They point out that the failure of Jortner's model stems from not allowing the excited states to experience all the different sites available for the photo-induced electron transfer. The electron transfer lineshape function is defined as:

$$W(\nu) = \int P(R)\ |M(R)|\ I_R^2(\nu)\ d\tau \tag{5}$$

where M(R) is the transition moment of the absorption, P(R) the electron transfer probability for a given site, and $I_R(n)$ is the Frank-Condon factor including coupling of the electron to both the high frequency molecular modes, and the low frequency solvent modes. The function $I_R(n)$ was shown to depend on a solvent reorganizational energy and a short-range molecular deformation energy, values for which could be estimated from experiment. Then, assuming a hydrogenic wavefunction the transition moment was calculated, and P(R) becomes the hydrogenic density of states. With these approximations, and evaluating only nearest neighbor electron transitions, reasonable agreement was obtained in the calculated absorption profile as compared to experiment. When the added refinement of site interactions past the first solvent shell were included, a higher energy feature appeared in the absorption profile, finally resulting in a calculated absorption lineshape which fits quite well the experimental one. Thus, the conclusion is reached that the long wavelength (I_R) energy absorption is due mostly to short range solvent interactions, while the visible absorption is ascribed to long range interactions that involve coupling to both the solvent and the molecular modes - i.e. a solvated electron.

The theory of Funabashi, Carmichael and Hamill doesn't provide a description of the physical mechanism of the trap itself, and so doesn't necessarily conflict with the solvent dipole alignment idea postulated earlier. In fact, direct experimental evidence exists for such charge-dipole structures acting as electron traps. Kevan[36] has employed electron magnetic resonance techniques, primarily electron spin-echo to determine the geometrical structure surrounding the

trapped electrons produced by pulse radiolysis. He is able to discriminate against the phase relaxation part of the decay and look only at the modulation function which relates to the geometry of the hyperfine-coupled nearby protons with respect to the electron. Figure 5 shows the structure he finds for a solvated electron in a glass. Results are similar for a variety of other systems investigated, in each case showing that the electron was trapped at the center of a dipole cage of aligned solvent molecules.

Minday et al.[37] first attempted to fit their mobility data on electrons in liquid hydrocarbons with the free electron theory of Cohen and Lekner[16] which models the electrons as free particles encountering both coherent elastic and inelastic collisions. An implied restriction is that the Coulomb field of the electron doesn't affect the structure of the scatterers the electron moves through. In light of the charge-dipole explanation of traps, this appears to be a serious restraint. In fact, Minday et al. find the mobility calculated from Cohen-Lekner theory to be too high by a factor of 100, and an incorrect temperature dependence prediction for their data. They conclude that the motion of an electron through liquid hydrocarbons can't be described with free-electron like collisions. Instead they invoke a phenomenological trapping model whereby the electron is "free" (i.e. for a solid it is moving in the conduction band), only part of the time, and upon collision it is trapped for some time t_a. The actual mobility is now given by:

$$\mu \approx \frac{\mu_0}{\nu \tau_a} \tag{6}$$

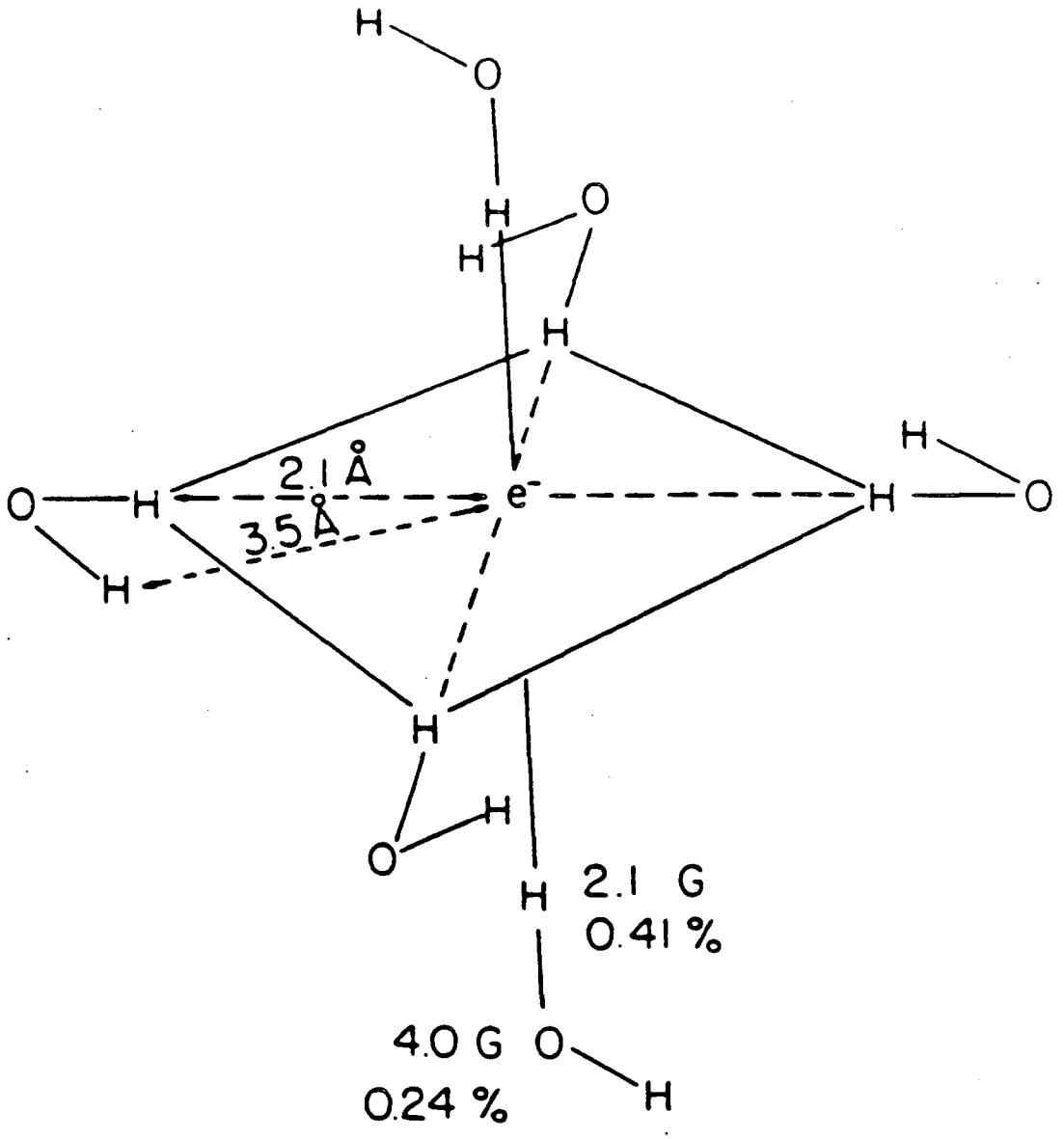

XBL 872-510

Figure 5. The structure of a solvated electron in a 10 M NaOH glass at 77 K determined by the spin-echo ESR technique by Kevan. The trap is defined by the alignment of the H_2O dipoles around the electron. From ref. 36.

where ν is the frequency of the trapping event, and μ_0 is the mobility of a "free" electron. In addition they allow the trapping/detrapping to be a thermally activated process:

$$\tau_a = \tau_0 e^{E_a/k_B T} \tag{7}$$

with t_0 being a vibrational period ($\approx 10^{-13}$ s) and E_a the trap depth. Equations (6) and (7) fit their data fairly well. They were able to calculate values for E_a from Arrhenius type plots of their data. This gave τ_a's of $\approx 10^{-10}$ s in hexane, and also predicts, using eqn. (6), the correct ratio of the "free" mobility (estimated from Cohen-Lekner theory) to the measured. They concluded that this trapping mechanism is most likely related to a dipole-charge interaction, since they could rule out the possibility of impurities. This thermally activated model has become known as the diffusion model since it allows the electron to diffuse in a "quasi-free" state between the times spent in trapping states.

Funabashi and Kajiwara[38] qualitatively describe a similar theory for electron trapping, but they take the perspective that it is the fluctuations in the electronic polarizability of the medium by which the electron is stabilized. This leads to the prediction that a more nonspherical molecule should exhibit better electron trapping since the fluctuations in it's polarizability will be greater. Experimental evidence supporting this is mentioned by Willard, who states that both the dipole moment and structure of the molecule correlate with trap depths.[39] Funabashi and Kajiwara also include another interaction in their trap model. Since the electron can

exist on any of the solvent molecules, a resonance interaction term is generated which depends on the similarity and spatial separation between two different sites. This term is also called a transfer integral and dictates how fast it takes an electron to "hop" from site to site. This "hopping" motion is different from the two-state diffusion model just discussed, because no quasi-free state exists, the electron merely travels from one trap to another. This model is discussed by Schmidt[40] who uses it to fit his temperature dependent mobility data in liquid hydrocarbons. An activation energy is associated with the hopping frequency (ν):

$$\nu = \nu_0 e^{-E_a/k_B T} \tag{8}$$

This leads to the following expression for the mobility:

$$\mu = \frac{e}{k_B T} R^2 \nu_0 e^{-E_a/k_B T} \tag{9}$$

where R is the mean hopping distance. The temperature dependence of this equation is slightly different than the pure Arrhenius form of Minday et al. (eqns. (6) and (7)), but it appears that both diffusion and hopping models are in reasonable agreement with experimental data, and Schmidt concludes that both models fit sufficiently well. A photoionization study in liquid hexane has offered indirect proof that the two-state model with diffusion is incorrect.[41]

A more rigorous test of electron mobility theories has been presented by Krebs and Heintze.[42] They obtain time-of-flight

mobility measurements in ammonia over four orders of magnitude of density, spanning it's critical point. They find that density is the crucial parameter to consider in choosing a model, and identify three different density ranges in their data. For the first, at relatively low gas phase pressures, the mobility of electrons is given by a simple single scatterer theory where collisions are characterized by a mean free path. In the next density regime, that approaching the critical point, a faster fall of mobility with density is found. Although they admit that the low density part of this regime might be fit with the two-state diffusion model, they find quantitative agreement with a more detailed version of the trap-hopping model. Following a similar model for amorphous semiconductors, they include two populations of traps: one (N_1) at lower energy (by ΔE) than the other (N_2), but still close enough in energy to allow for thermally activated hopping to occur as in eqn. (8). The physical explanation underlying the existence of these two states will be deferred until later. Their expression for the apparent mobility is:

$$\mu_{app} = \mu N_2 \left[N_2 + N_1 e^{\Delta E/k_B T} \right]^{-1} e^{-2\alpha R} \tag{10}$$

where μ is the mobility used by Schmidt in eqn. (9) and the last exponential is a correction to eqn. (9) where $1/\alpha$ is a distance characterizing the spatial overlap between sites (this corresponds to the transfer integral as defined by Funabashi and Kajiwara). Krebs and Heintze find good agreement with their data up to the critical point by this equation.

After the critical point the mobility turns around and begins to

rise with density, and here they use a small polaron description of the trapped electron to explain their data. A small polaron is a particle constructed from an electron and it's induced polarizability in the medium, coupled through the longitudinal optical phonons of the matrix. Thermally activated movement of the polaron is allowed by exchange with it's nearest neighbors. Krebs and Heintze found they can achieve some agreement with this model by postulating overlap between polarons, leading to the charge transport.

Movement of trapped electrons by quantum mechanical tunneling has been proposed to explain time dependent data of the scavenging of electrons in NaOH glasses at 77 K by an added ionic impurity. Miller[43] develops this theory by assuming a rate for tunneling to be given by the product of a frequency factor ($\approx 10^{15}$ s^{-1} for electronic motion) and a barrier transmission coefficient. The fraction of remaining (unscavenged) electrons is then given by:

$$\frac{N(t)}{N_0} \propto e^{M[a_0 + B^{-1/2}(\text{const.} + \log t)]^3} \tag{11}$$

where M is the concentration of scavenger molecules, a_0 is the radius of the acceptor, and B is the barrier height. Miller has achieved reasonably good fits to his data for the decay in the absorption of the electrons over the tremendous time range of 10^{-6} to 10^{3} s. His results imply tunneling of electrons through tens of angstroms of solvent molecules. Besides the fits to the data, other observations supporting this model include a virtual independence of the absorption decay rate on temperature, a strong dependence of trapped

electron lifetimes on concentration of scavengers, and Miller's belief that diffusion must be severely quenched in matrices at cryogenic temperatures.

A compelling argument against this barrier tunneling model has been advanced by Hamill and Funabashi.[44] They maintain the results can be equally well represented by a non-Gaussian diffusion model, and they begin with the simple rate equation:

$$\frac{dN(t)}{dt} = -Mk(t)N(t) \tag{12}$$

with N representing the electron population, k(t) the time dependent rate constant, and N, and M are defined as before. They show, based on a random-walk argument that k(t) can be written as:

$$k(t) = Ct^{\alpha-1} \tag{13}$$

where C, and a are constants; α varying between zero and one. After solving eqn. (12) with (13) these authors proceeded to fit Miller's data and achieved good agreement for different scavengers over the entire decay range with constant value of α. The experimental observation of the lack of temperature dependence would still appear to be a problem with this picture since detrapping of electrons should be thermally activated, but the argument is presented that the prediction of a temperature dependence is obscured by the counterbalancing effect that higher temperatures might have in further lowering the trap depths by allowing better dipole alignment around the electron. This lower trap depth will decrease the hopping

rate out of the trap, thus opposing and perhaps offsetting the increase in hopping due to the increasing k_BT.

Although it has been alluded to already, the basic question concerning the formation of a trap has not been addressed. It has been shown that alignment of solvent molecule dipoles can trap an electron, but a mechanism is still required to slow the electron down or hold it long enough for the solvent dipoles to form the trap. The theory of Jortner[32], where the potential well is formed through the difference in the static and optical bulk dielectric constants evidently ignores this question. However, Funabashi and Kajiwara[38] provide an answer by virtue of the polarization fluctuations they propose as the basis of trapping. According to their theory, an electron travels until it hits a sufficiently formed potential which can then develop into a trap in response to the presence of the electron. Albrecht[45] also endorses this picture as an explanation for his studies of electrons trapped in TMPD. He views the solid as full of physical cavities stemming from uncertainty principle considerations applied to the electronic polarization of the medium. Further stabilization of the trap is believed to occur due to the slower timescale of solvent relaxation around the electron. Experimental evidence in support of this has been found in annealing studies where a shift in the electron's absorption spectrum,[39] and differences observed in it's ESR linewidth are seen.[36] This fact also gives credence to the postulated existence of the two discrete trap states at different energies in the model of Krebs and Heintze[42] discussed above.

There are other distinct mechanisms besides the solvent dipole

stabilized structures which would also give rise to electron trapping. A classical image potential exists for an electron in the vicinity of a dielectric surface given by:

$$V_I(x) = \frac{-e^2(\epsilon - 1)}{4(\epsilon + 1)d} \tag{14}$$

where d is the distance of the electron from the surface of a material of dielectric constant ϵ. This formula becomes infinite at the surface, so obviously it breaks down at some finite distance away, on the order of a few angstroms.[46] While Sanche[7] and Hiraoka[12] both acknowledge the existence of such a potential, their discussion of its possible effect on their data is cursory. Huang and Magee[4] conclude the effect of the image potential will be manifested in films of positive V_0 (i.e. the zero electron energy level in the film is above the vacuum level) by introducing a small effective barrier for electron escape. Chang and Berry[3] point out that a quantitative assessment of the image potential's effect on the attenuation of photoejected electrons is difficult since the dielectric constant of the molecular films increases with film thickness especially for the initial growth.

Minday[37] provides quantitative evidence of an image potential effect in his work on photoinjected electrons in liquids. It can be shown for a surface in an applied field that a maximum in the barrier potential exists at:

$$d_m = \left[\frac{e}{4E}\right]^{1/2} \tag{15}$$

where E is the applied field. This maximum occurs due to the decrease of the image potential and the increasing value of the applied field with distance from the surface. Minday argues that if d_m were assumed to be a cut-off such that for electrons at $d < d_m$ none were transmitted to the detector, while for $d > d_m$ all were transmitted, then the collected photoelectron current would be expected to be exponential with respect to d_m and therefore also exponential with $E^{-1/2}$. He verified this dependence experimentally, thus proving the existence of image field effects in these experiments. Further discussion of image potential effects will be presented in part V.B..

Actual quantum mechanical trapping of electrons by the image potential was treated by Cole and Cohen in 1969.[47] They examined the case of a potential well confined by a combination of the electron's image field and the surface barrier which exists for a material with positive V_0. This well should produce quantized hydrogenic states for a bound electron. For liquid helium they estimated the ground state energy of a bound electron to be 0.6 meV. Absorption spectra for transitions to two excited bound states verified this prediction five years later.[48] The energy levels agreed fairly well with Cole and Cohen's simple image potential model. A few years later Echenique and Pendry theoretically predicted the existence of image bound states on metal surfaces.[49] They took a slightly different view by picturing the image state as being formed by repeated Bragg reflections between the bulk crystal potential and a surface barrier. Thus two types of surface states emerge: one associated with the crystal surface potential, and the other due to the image potential.

The former are the well documented surface states that are often thought as occurring due to dangling bonds at surfaces. The others, bound hydrogenic electron image potential states, were postulated to have spatial wavefunctions localized well on the vacuum side of the surface. Echenique and Pendry predict it is this separation from the surface that should allow these states to be observed - if they were right at the surface they would presumably be too broadened to resolve. The direct experimental verification of these image states had to wait for the development of inverse photoemission spectroscopy (IPS) which is sensitive to states lying between the Fermi and vacuum level. In 1984, quantitative agreement was found[50] for a feature in the IPS spectrum with the calculated n=1 level of an electron bound by the image potential of a metal. By demonstrating that the same peak 0.6 eV below the vacuum level was observed on both Au and Cu surfaces, it was shown that this peak was not associated with a material property, but rather was a general characteristic of a metal surface. Figure 6 displays the potential energy and spatial extent of these image potential states near a metal surface. Later, another study[51] compared IPS features due to a dangling bond type surface state with that associated with the image potential. The measured dispersion curves verified the difference by exhibiting a curvature indicative of a free electron for the image potential state, while showing considerably higher curvature for the crystal potential state. Echenique et al.[52] have predicted the widths of these states to be about 8 meV (≈8 ps). Most recently,[53] Bausells and Echenique have examined the binding energy dependence for electrons at higher energy (i.e. a finite momentum parallel to the surface), and found

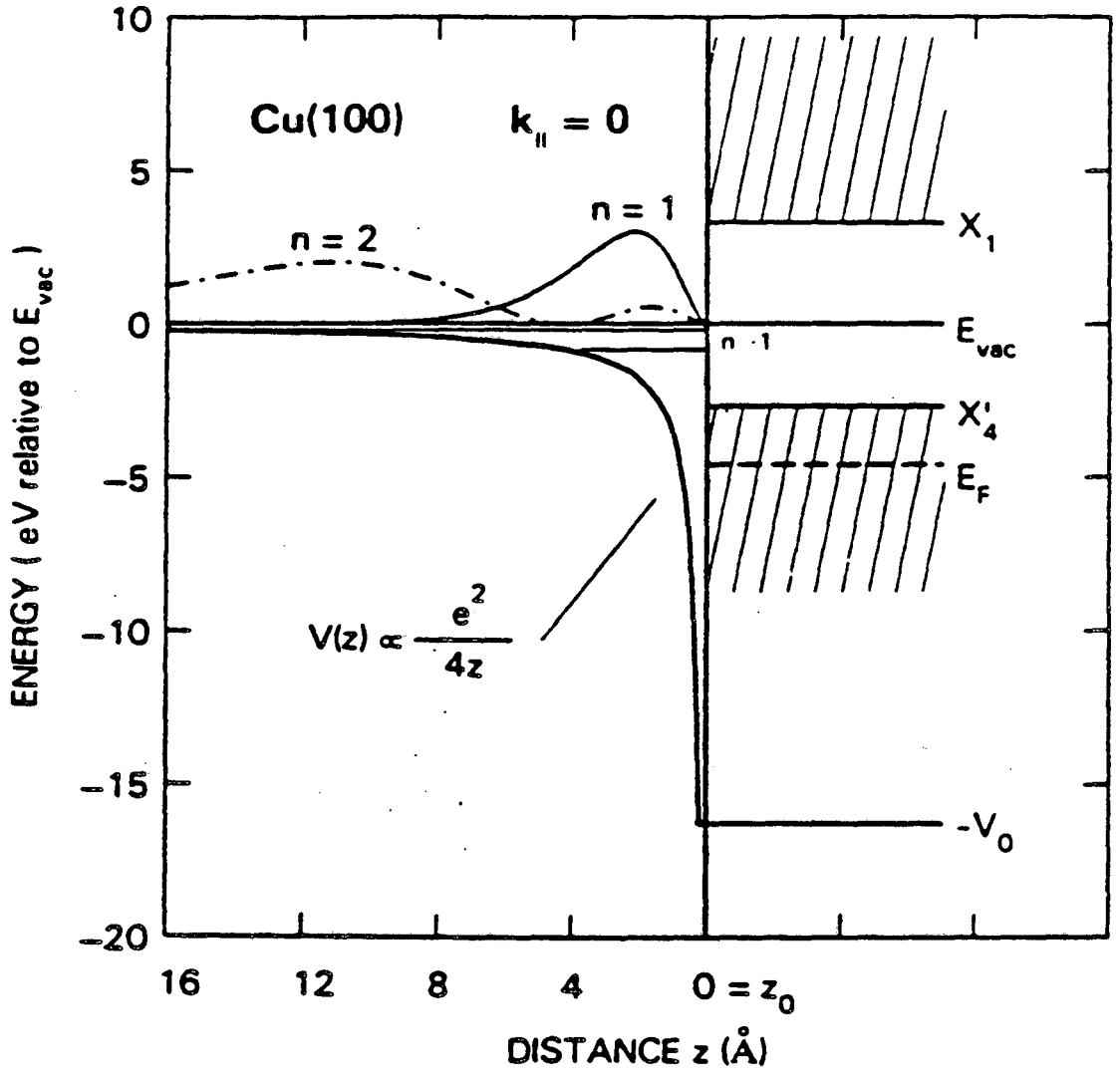

XBL 872-515

Figure 6. Potential energy diagram for the electron image potential, and it's associated bound states near Cu(100). The spatial extent of these states is also shown. From D. Straub, F.J. Himpsel, Phys. Rev. B, 33, 2256 (1986).

that quite a large range exists over which these energetic electrons could be bound in image potential states.

An independent study revealing a similar effect was reported recently for liquid Krypton.[54] These authors interpret their time of flight mobility data as suggesting that the electrons exist and travel in a quasi-free state ($V_0 < 0$ for Krypton) along the liquid/gas interface. This behavior was observed at low applied fields; at higher fields the surface barrier was overcome and the electrons left the condensed fluid.

Another image potential related idea was proposed by Antonicwicz et al..[55] They considered the trapping of an electron by a dielectric sphere, such as might be formed if clusters of molecules were imagined. They used an image potential for an electron both outside and inside the sphere, each potential falling (rising) as the sphere surface is approached. The potential is fixed at some critical value near the surface to prevent it from going to infinity. Finally, the potential jump at the surface of the sphere is determined by the characteristic value of V_0 for the material, which may be positive or negative. A diagram of such a potential is shown in Figure 7. Using a dielectric constant for H_2O ($\epsilon = 1.76$), they find the number of bound levels increases with sphere diameter, as does the binding energy of a given level (bound levels are on the order of 0.1 eV). Binding energy was also found to increase when V_0 was more negative, and to increase linearly with the dielectric constant. It is conceivable that such a mechanism could play a part in the total solvation process. If a cluster were responsible for the initial electron capture, it conceivably could then be further

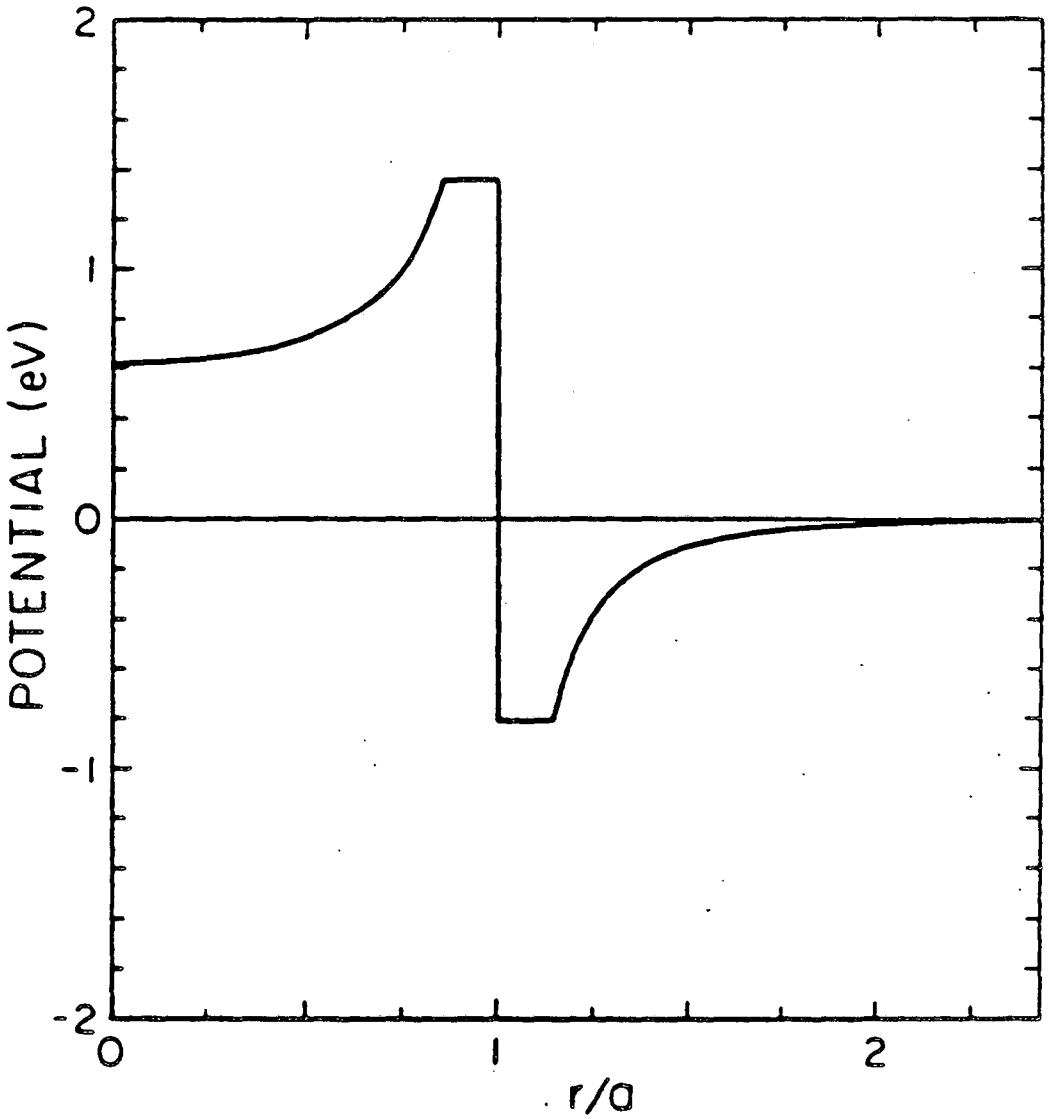

XBL 872-509

Figure 7. The potential used by Antoniewicz et al. to model the trapping of an electron by a dielectric sphere of radius r. It falls off both inside and outside the sphere as an infinite sum of $(a/r)^n$ terms. n is odd outside, and even inside the sphere. From ref. 55.

stabilized by solvent dipole reorientation.

A different sort of electron trapping associated with solvent dipoles was discussed in a series of three papers by Belmont.[56] He considers the case of a single dipole capturing the electron itself, unaided by any concerted solvent rearrangement. His first observation is to note that there exists a critical value for a dipole moment p above which it is capable of trapping an electron. He states this value will be given approximately by the known critical gas phase value of 1.65 D multiplied by the dielectric constant of the medium. Thus, it seems relatively large dipole moments are required to activate this mechanism. To make this concept quantitative Belmont calculates an effective cross section based on an Onsager-type length, i.e. he solves to find a distance at which the attractive potential due to the dipole is just equal to the electron's thermal energy. In order to then state that an electron approaching a dipole any closer than this distance will be captured, the energy loss required for the electron to fall into the trap must also be considered. As long as the electron's MFP is sufficiently short to allow for this energy loss, the model will be valid. Belmont uses the long range part of the dipole potential with the assumption that an electron is far away compared to the dipole separation. After solving the above problem he applies a geometrical argument to provide for some screening effect of the attractive (positive) end of the dipole by the negative end. The final solution for the cross section (in units of m^2) is:

$$\sigma = \frac{ep}{32k_B T \epsilon_0 \epsilon_r} \tag{16}$$

where p is the dipole moment, ϵ_0 is the permitivitty of free space, and ϵ_r is the relative permitivitty of the medium. Although Belmont doesn't comment on the magnitude of the values obtained from eqn. (16), the calculated cross sections are surprisingly large. For the modest values of p = 1.0 D, and ϵ_r = 2.0, at room temperature, the cross section is 25 $Å^2$ - comparable to a molecular area. These results, if correct, imply that such a trapping mechanism could be very important for molecules with a significant dipole moment.

C. Summary

A review has been given of the interactions that a low energy electron in a condensed organic phase might encounter. A simple comprehensive picture does not appear to exist at this time, due to the seemingly disparate results for the LEETS type of experiments as compared to the bulk photoconductivity investigations. The former have almost all their observed losses ascribed to discrete molecular resonances, while the discussion of trapping in the latter revolves mainly around physical solvent structure. A number of possibilities to reconcile these differences can be postulated. If the traps exist over a broad range of energies, as certainly appears plausible, then perhaps the LEETS curves simply don't resolve structure due to trap losses. Another is that the losses due to traps are a very small fraction of the total losses, so that only the resonant losses are observed. A third scenario involves the electrons first suffering a loss via a resonant mechanism, and then being subsequently trapped. The LEETS spectra in this case would be expected to show structure corresponding only to the resonant losses. It is obvious further

study, possibly incorporating a new type of experiment, is required to unify these observations and to provide a better understanding of an electron in condensed media.

III. Review of Work Function Shifts with Adsorbed Molecules

A. Theoretical Treatments of Work Function Shifts

The work function is defined as the energy required to extract an electron from the bulk of a solid. It was Lang,[57] in 1971 who showed rigorously that this definition is equivalent the following often used expression:

$$\phi = \Delta V + \mu \tag{17}$$

In this equation μ is the chemical potential of the solid which is solely a property of the bulk. The surface contribution to the work function is given by the ΔV term which is the change in potential energy across the surface. This latter term is a direct result of the abrupt loss of symmetry which occurs at the surface. This causes a perturbation of the lattice positions of the surface atoms with respect to those in the bulk, and more importantly, a smearing of the electron distribution into the vacuum. This charge asymmetry at the surface can be represented as a layer of dipoles and is often referred to as the "double layer". A simple electrostatic argument[58] shows that ΔV term in equation (17) can be related to the concentration of dipole moments on the surface by:

$$\Delta V = -4\pi epN \tag{18}$$

where e is the charge on an electron, p is the dipole moment normal to the surface (positive for a dipole with it's positive end outward), and N the concentration of dipoles per unit area. Together with equation (17), these equations relate the surface dipole moment density to the work function. The smeared electron distribution at the surface also creates a large electric field. This field can act to polarize molecules adsorbed at the surface, thus changing the effective surface dipole layer. As a consequence the ΔV surface term is quite sensitive to adsorption via the associated effects of alignment of permanent molecular dipole moments, creation of induced moments via the polarizability of the molecular adsorbate by the surface field, and charge transfer between the molecules and the surface resulting in an image dipole moment. These three contributions to work function shifts upon adsorption are sketched in Figure 8. The work function change upon adsorption is given by:

$$\Delta\phi = \phi_{ads} - \phi_{clean} = -4\pi e p_{eff} N \tag{19}$$

where p_{eff} now represents the sum of the adsorbate contributions to the dipole layer via the schemes delineated above. This relation is called the Helmholtz equation, and almost every theory for adsorbate induced $\Delta\phi$ shifts is based on this simple equality. A review of these theories will be given in this section. Theories based on electrostatic grounds will be discussed first, followed by more elaborate models. An excellent review of both the theoretical and experimental aspects of this topic was published in 1979 by Holzl and Schulte.[5] Kiejna and Wojciechowski[59] have also reviewed this field,

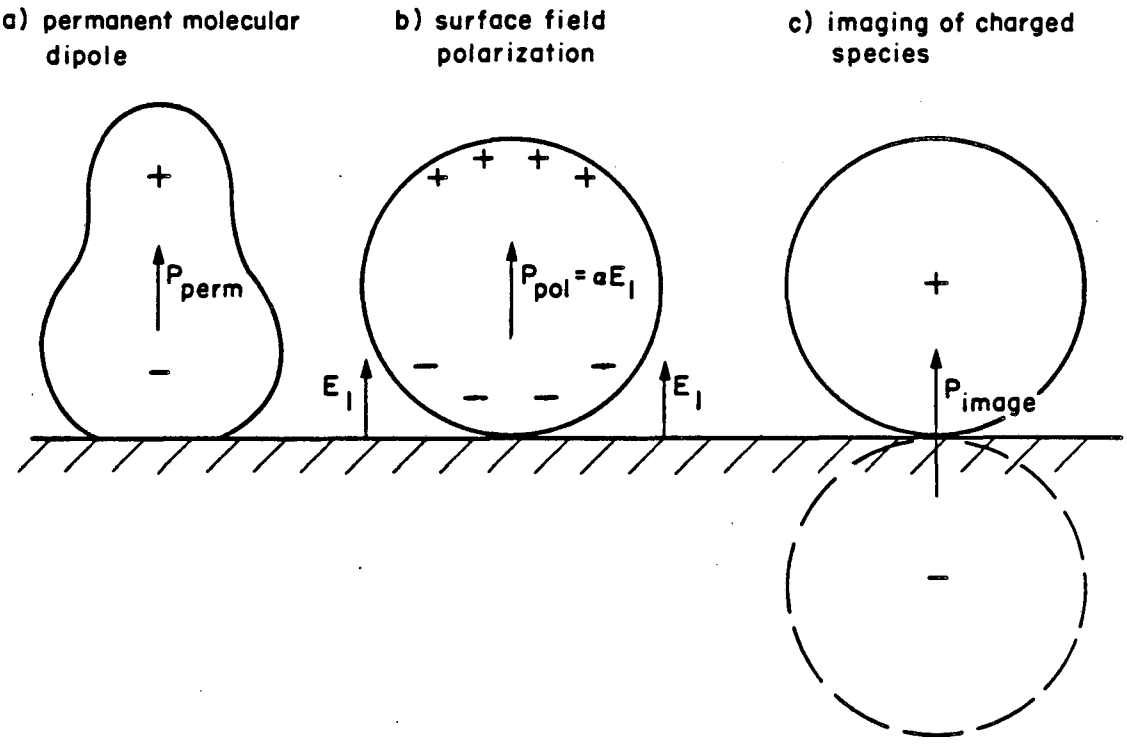

Figure 8. Schematic representation of three contributions to the $\Delta\phi$ induced by molecular adsorption. a) Alignment of a permanent molecular moment along the surface normal. b) Dipole creation via polarization of the adsorbate by the surface field. c) An image dipole due to adsorption of a charged molecule - either by charge transfer from a neutral to/from the surface, or by ionic adsorption. As drawn, all cases cause a reduction in the work function.

and both of the above articles discuss theories for bare metal photoemission and work function, a topic which won't be explored here. The classic paper by Herring and Nichols[60] also deserves mention with respect to the work function of bare metals.

A relatively straightforward, although rather phenomenological classical treatment which contains most of the elements of the problem is due to McDonald and Barlow[61]. They consider the three adsorbate contributions to $\Delta\phi$ already mentioned: a permanent dipole moment, polarization due to surface fields, and dipole moments created by imaging of charged adsorbates by the substrate. The charged species is due either to direct adsorption of an ion, or charge transfer from the adsorbate to the substrate. Using the Helmholtz equation (equation (19)), the work function shift may be expressed as:

$$\Delta\phi = -4\pi e N_1 \theta (p + \alpha E_1 - zed) \tag{20}$$

where θ is the fractional surface coverage, N_1 is the number of molecules per unit area in one monolayer, α is the adsorbate polarizability, z is the valence of the adsorbed species, and d is the separation of the charge from the surface. E_1 is the effective total surface field, which is composed of two parts. The natural surface field (E_{n1}) is a property of the bare metal surface as explained above. The other contribution to E_1 is the depolarization field resulting from the interaction of one adsorbate with the combined field of its neighbors. This depolarization field contains terms relating to each of the specific polarization mechanisms

represented in equation (20). E_1 is therefore given by:

$$E_1 = E_{n1} - (p + \alpha E_1 + 2zed) \sum_i r_i^{-3} \tag{21}$$

with r_i the distance between a given adsorbate and the i^{th} adsorbate. Topping[62] evaluated this infinite sum for the case of adsorption onto a regular 2-d lattice, and expressed it as a constant ($\Lambda \approx 9$) times the nearest neighbor distance of the adsorbate lattice. The sum then becomes $\Lambda\delta(\theta N_1)^{3/2}$, where δ is either 1 or $\theta^{-1/2}$ for the case of mobile adsorption or immobile adsorption, respectively. This expression may now be substituted for the lattice sum in equation (21), and solved for E_1.

$$E_1 = \frac{-\Lambda\delta(\theta N_1)^{3/2}(p + \alpha E_{n1})}{1 + \alpha\Lambda\delta(\theta N_1)^{3/2}} \tag{22}$$

Substitution of equation (22) into equation (20) gives the final result:

$$\Delta\phi = -4\pi e\theta\left[\frac{p + \alpha E_{n1} + 2zed}{1 + \alpha\Lambda\delta(\theta N_1)^{3/2}} - zed \right] \tag{23}$$

In theory this equation could be used to predict a change in work function for a given system. It becomes difficult in practice, however, to assign a priori, values for the various parameters such as polarizability and valence charge since these might well be expected to differ considerably from their gas phase values due to

surface interactions. Practical use of this theory will be discussed in the following paragraphs. Further work by McDonald and Barlow[63] has included the additional interactions resulting from imaging of the permanent and induced dipoles of the adsorbate by the surface. This is reflected in equation (23) in the $\alpha\Lambda\delta(\theta N_1)^{3/2}$ term in the denominator, which has added to it another θ-dependent term plus a constant.

If the adsorbate is constrained to remain neutral ($z = 0$ in equation (23)), and $(p + \alpha E_{nl})$ is replaced by an effective dipole moment, p_{eff}, then the following equation can be obtained.

$$\Delta\phi = \frac{-4\pi e\theta N_1 p_{eff}}{1 + \alpha\Lambda\delta(\theta N_1)^{3/2}} \tag{24}$$

This equation is named after Topping due to his early solution[62] of the energy of a 2-d matrix of dipoles. It was this result which was used earlier in equation (21) for the infinite series summation. The Topping equation has been widely used in the discussion of $\Delta\phi$ shifts.

Gomer and co-workers have made repeated use of the Topping equation with $\delta=1$, the case for mobile adsorption. This implies the adsorbates can move around on the surface after sticking, and requires that they maintain themselves equally spaced, on a 2-d lattice at all coverages. For both Na[64] and Cs[65] on W single crystalline surfaces good agreement was found between the experimentally measured $\Delta\phi$ points, and the Topping equation. Values of p_{eff} obtained from the fitted data ranged from 10-16 D for Na and polarizabilities from 26-35 $Å^3$ depending on the crystallographic face

of W. Likewise values for Cs varied between 15-24 D and 40-67 $Å^3$. That these values are much larger than gas phase values illustrates the limited predictive power of this model for $\Delta\phi$ behavior. Since alkali adsorption is often interpreted as ionic due to charge transfer, it is instructive to note that these relatively large dipole moments given here correspond to approximately half an electron of transferred charge into the metal. Wang and Gomer[66] have also used this equation for a classic physisorption case, Xe/W, but reported poor agreement with the data. By contrast, Palmberg[67] found that his $\Delta\phi$ coverage data for Xe/Pd(100) could be fit well by the Topping equation with a p_{eff} of 0.95 D and a polarizability of 8.2 $Å^3$. An example of equation (24) with $\delta = \theta^{-1/2}$, (immobile adsorption), is CO/Ir(110).[68] Good agreement was found for $\Delta\phi$ data collected at both 90 K and 300 K. Reflecting the smaller degree of charge transfer as compared to the alkalis, a dipole moment of only 0.1-0.3 D and polarizability of 6-20 $Å^3$ was determined for the adsorbed CO from the theoretical fits.

Heras and Albano[69] have derived a similar expression to the full treatment result obtained by McDonald and Barlow. Consistent with the latter, they include dipolar imaging in their depolarization formula. They differ in that they treat only the immobile adsorption case, and do not include the charge transfer mechanism ($\delta = \theta^{-1/2}$, $z = 0$ respectively in equation (23)). They are the first to define an effective coverage, making use of the fact that in the case of immobile adsorption, there exists an ever increasing probability that an adsorbing molecule will impinge and stick on a previously populated site. Therefore the second layer begins to grow before

completion of the first. The complete expression given by Heras and Albano is:

$$(25) \qquad \Delta\phi = 4\pi e\theta_1 N_1 (N_1 + \alpha E_{n1})/\epsilon$$

$$\epsilon = 1 - \alpha\left[\frac{1}{16\pi d^3} - \frac{(3/4)^{3/4}}{4\pi} N_1^{3/2}\theta_1 [15.81 - 12.0(3/4)^{1/2} N_1 d^2] \right]$$

$$\theta_1 = \frac{e^{2\theta} - 1}{e^{2\theta} + 1}$$

where all terms are defined as before and θ_1 = fractional coverage of the first monolayer. This equation is of the same form as the comparable result of McDonald and Barlow, with differences appearing in the denominator (ϵ). Heras and Albano use equation (25) to fit $\Delta\phi$ vs. θ data they have collected for H_2O/Co films. H_2O adsorbs dissociatively on clean Co films and for this phenomenon poor agreement is seen between the experimental data and equation (25). However, after "passivating" the surface with successive adsorption/desorption runs, they found H_2O dissociation to be impaired and application of equation (9) gave satisfactory fits to the data. The value for the surface field E_{n1} obtained by fitting is 10^8 V/m with a surprisingly large polarizability of $\approx$300 $Å^3$, which they explained as consistent with the large value found for the surface field.

Bradshaw and Scheffler[70] follow a similar approach as Heras and Albano and apply the result to the system Xe/Pd(100) from Palmberg's work mentioned above. The inclusion of the effect of imaging the dipoles in the substrate, absent in the Topping equation, allowed for

a good fit using the gas phase value of 4 $Å^3$ for α and p_{eff} = 0.93 D. Palmberg had to assume a higher α of 8 $Å^3$ for a successful fit.

A more rigorous quantum mechanical calculation is presented by Antoniewicz[71]. He considers only the dispersion forces that arise for a molecule near a surface. This problem of a dipole interacting with its surface image was originally solved by Lennard-Jones, who showed that the energy varies as d^{-3}, d being the molecule-surface separation. Antoniewicz includes another term in the expansion which goes as d^{-4} and uses these two terms to form a Hamiltonian for a molecule near a surface. He then adds a second oscillating dipole and includes interactions between each of the two dipoles with each of the image dipoles. The total Hamiltonian thus formed is used in a variational calculation which ultimately yields an expression for $\Delta\phi$. Interestingly, he shows that for the case of a spherically symmetric adsorbate, the Topping equation is obtained. For an anisotropic molecule, however, a significant new term appears in the equation which Antoniewicz estimates provides a 20% reduction in the $\Delta\phi$ shift compared to the Topping equation. Unfortunately, this prediction does not appear to have been experimentally tested. Another result of this work is an explicit formula for the polarizability of the adsorbed molecule in terms of the gas phase α, and the molecule-surface distance. This is the first quantitative prediction of the effect of the surface on the polarizability of the molecule.

Most of the theories examined thus far have been based on electrostatic polarization of the molecule by the surface field. A conceptually different approach is the charge-transfer no-bond (CTNB) theory borrowed from Mulliken's[72] work on donor-acceptor complexes.

Mignolet[73] suggested that differences in the electron configuration of the solid at the surface would allow for charge-transfer to occur from the molecule to the surface, which is the required direction to produce a lowered $\Delta\phi$, consistent with experiment. This is opposite to what might first be predicted on the basis of simply comparing the ionization potential (IP) of the molecule to the smaller value of ϕ for the substrate.

In the CTNB theory, the wavefunction for the adsorbate/surface system (ψ_T is written as a linear combination of ψ_{NB}, the separated ("non-bonded") molecule and surface wavefunction, and ψ_{CT} the wavefunction for the system after charge transfer.

$$\psi_T = a\psi_{NB} + b\psi_{CT} \tag{26}$$

By applying second order perturbation theory an expression is obtained for the energy of adsorption (Q_{CTNB}) and similarly the dipole moment of the complex can be shown to be proportional to $(a/b)^2$, which is intuitive, since this represents the degree of charge asymmetry. The relation between the energy of adsorption and the work function (related, as usual, through the dipole moment) is:

$$Q_{CTNB} = \left[(IP - \phi - \frac{e^2}{4d})/4\pi e\theta N_1 d \right] - \Delta\phi \tag{27}$$

where e^2/d is the image potential term for a charge a distance d above the surface. This equation was used by Nieuwenhuys[74] et al. to test the CTNB theory against the simple surface polarization model

already discussed for adsorption of Xe on a series of five transition metals. The comparison is complicated by the fact that in both theories the adsorption energies also contain a contribution from dispersion interactions with the surface as was treated in the model of Antoniewicz above. In this instance the formulation of the dispersion interaction given by Mavroyannis[75] is more appropriate since he computed the effect on the adsorption energy itself. Mavroyannis also improved on Antoniewicz's model by replacing the assumed perfect reflectivity of the substrate with the dielectric constant for a free electron gas. This dispersion term must therefore be subtracted from Q_T so that the true Q_{CTNB} can be used in equation (27). After applying this correction, Nieuwenhuys et al. conclude that CTNB describes the data better than the prediction given by surface polarization. However, considering the uncertainty involved in determining the correct energy of adsorption, and the somewhat small differences between the two theories, this conclusion is rather tenuous. Indeed, a similar comparison performed by Gundry and Tompkins[76] for a series of four noble gases adsorbed on W, concluded that either theory provided a satisfactory fit to the $\Delta\phi$ data.

Charge transfer between the metal and adsorbate was considered via an entirely different mechanism by Gurney[77] in 1935. He conjectured that as the adsorbate approaches the substrate any discrete adsorbate valence levels of the adsorbate near the Fermi energy of the solid will begin to broaden in energy due to interactions with the solid. Gurney postulates that the Fermi level of the solid will determine the occupancy of this broadened molecular

state for a directly adsorbed molecule. That is, the level's population is determined by the fraction of that level which falls below the Fermi level when the molecule is on the surface. The degree and direction of the net charge transfer is then the difference between the population of the adsorbate level in the gas phase minus it's population after adsorption. For the case when the adsorbate level is less occupied than it's gas phase value, a dipole moment is formed which points towards the surface, causing a decrease in the work function. This raises the Fermi level relative to the molecular level and in turn causes charge transfer from the metal back into the molecule, which has an opposite effect on the work function. As more molecules are adsorbed, each will have an increasingly smaller effect on $\Delta\phi$. It can be seen then, that $\Delta\phi$ with respect to coverage will in general be a nonlinear function, and may indeed go through a minimum, as is often observed experimentally. This theory of Gurney's accounts qualitatively for the trends seen in measured $\Delta\phi$ data for adsorbed alkalis and alkaline earths.

Muscat and Newns[78] quantify the ideas of Gurney and apply the theory to experimental results for Cs/Re(0001). They consider both the valence s and p_z orbital of a Cs atom as it approaches the surface. As is shown in Figure 9, they hold the energy difference (2E) between the two atomic orbitals fixed at their gas phase separation, but allow their mean energy (E_i) relative to the Fermi level to vary. The broadening (Δ) is assumed to be the same for each atomic level. The work function shift may now be expressed as:

$$\Delta\phi = 4\pi e\theta N_1[ed(n-1) + p] \tag{28}$$

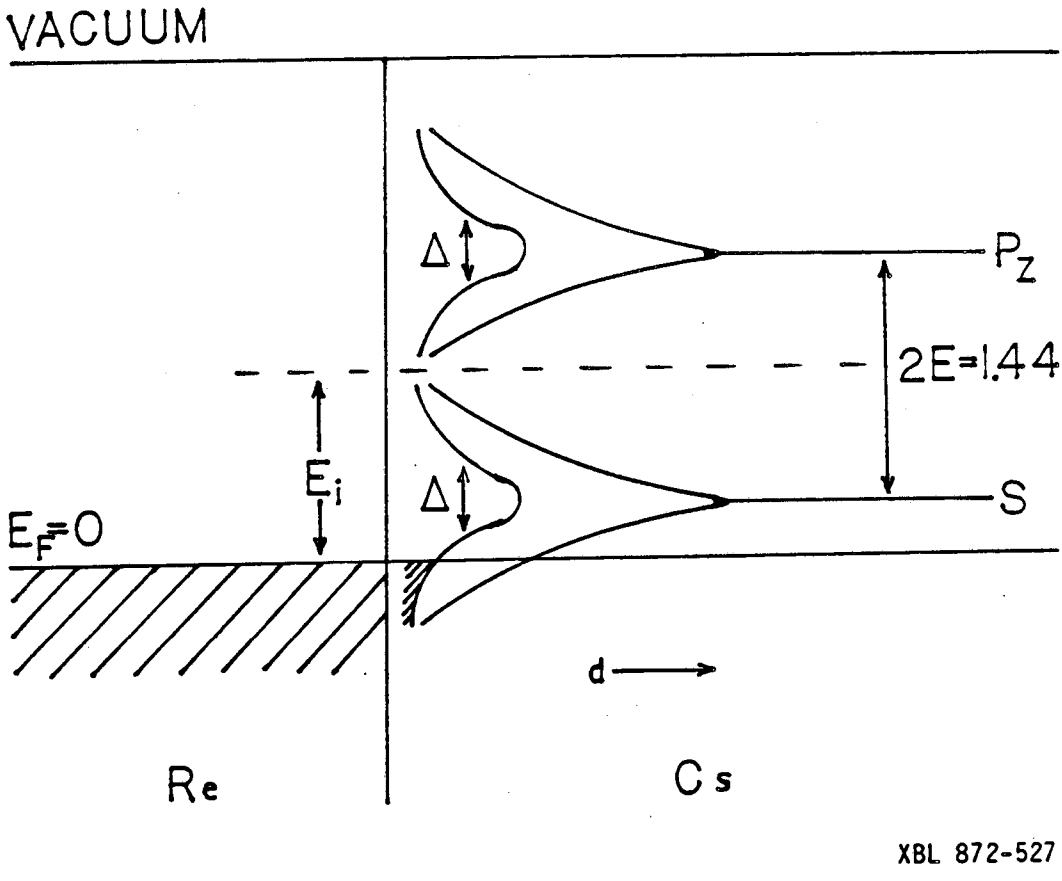

Figure 9. The model of Muscat and Newns for $\Delta\phi$ shifts. The s and p_z levels of a Cs atom broaden by Δ upon it's approach to the Re surface. The shaded portion of the broadened s orbital indicates it's population as determined by it's position relative to the Fermi level E_F. After ref. 78.

where p is the dipole moment of the Cs atom itself, and the first term is the dipole moment due to charge transfer. n is the total electron population in the s and p_z orbitals; the first term is therefore zero for the gas phase Cs configuration of a singly occupied s level. The Hamiltonian is written in terms of raising and lowering operators and consists of two parts. The first considers the interaction of an adatom with the substrate. The second part includes the electrostatic depolarization field from neighboring adatoms as has been encountered in theories already discussed. In the Newns-Anderson approach used, a Green's function is defined from which the population n and the dipole moment p are obtained. The general solution is quite complicated and in order to compare to experiment several steps are involved. The low coverage approximate solution is obtained, and a relation between Δ and E_i in terms of d and λ (a charge asymmetry parameter directly proportional to p), is obtained after solving for $p(\theta=0)$ and equating this to the experimentally determined dipole moment at low coverage. By choosing values for the parameters (Δ,E_i) and (d,λ) a plot of $\Delta\phi$ vs. θ can be generated and compared to the experimental curve. The fit is now optimized by first varying (Δ,E_i), and then by changing (d,λ) and reoptimizing with the first set. While the method doesn't yield one unique fit, one of the best fits obtained by Muscat and Newns is shown in Figure 10, along with two other curves for different values of Δ. Optimized values for the parameters are given in the caption for Figure 10. It should be noted that the levels have broadened to the point that they just intersect at their FWHM's, so considerable overlap exists between the adsorbed Cs s and p_z orbitals. Also, the

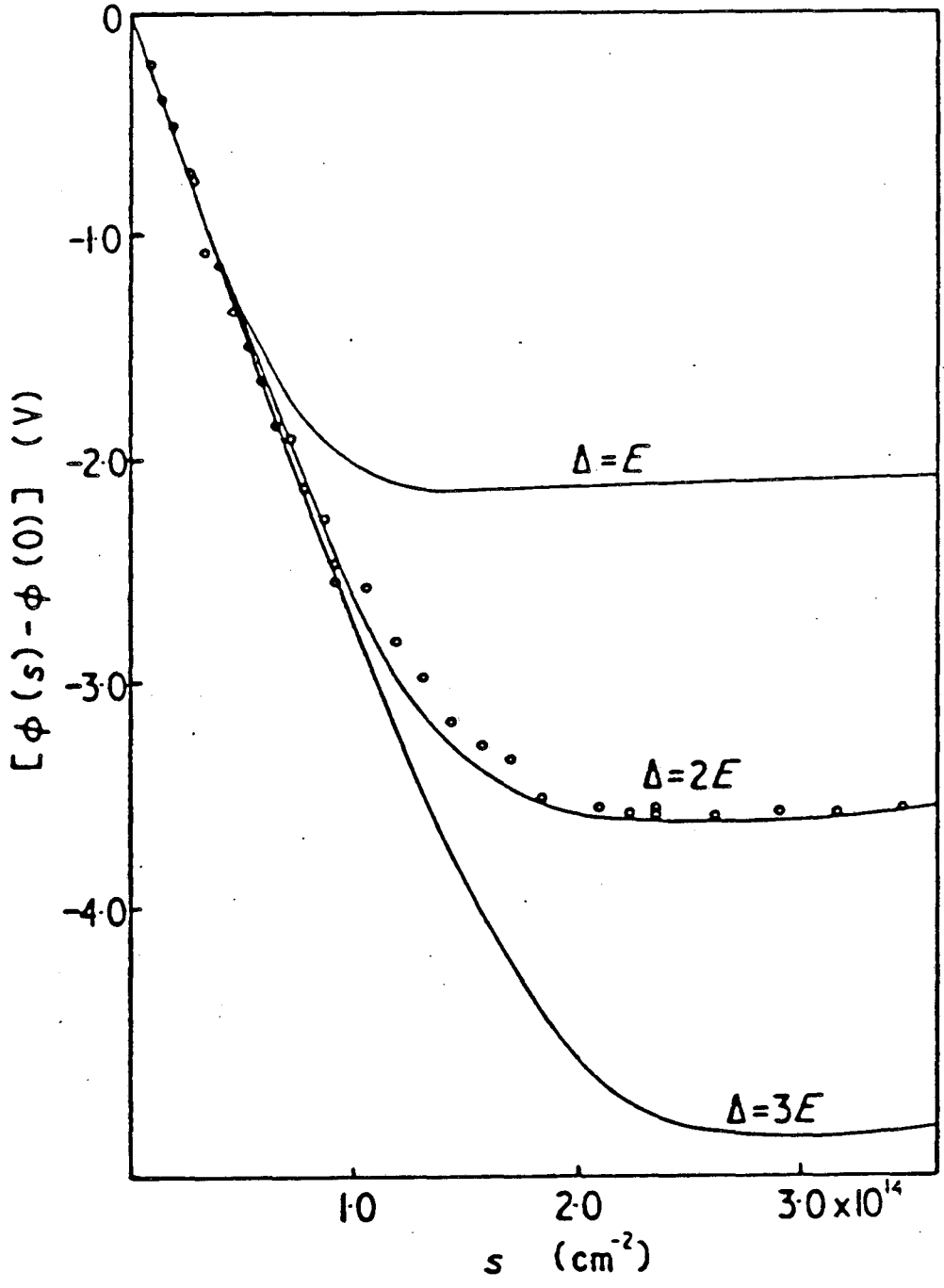

Figure 10. Fits of the level broadening model of Muscat and Newns (lines) to the $\Delta\phi$ vs. coverage data for Cs/Re(0001) for different values of Δ and E. Also used here are the values λ = -1.2 Å, and d = 2.2 Å. Parameters are defined in the text and Figure 9.

fact that E_i is 3.4E above the Fermi level indicates that only the tail of the broadened s orbital will fall below the Fermi level - reinforcing the idea of positive ionic adsorption of the Cs due to charge transfer to the substrate.

A simpler, more appealing quantum mechanical model was proposed by Lang[79], and is an extension of a theory used earlier by Lang and Kohn[1,80] to predict ϕ for a bare metal surface. The substrate is represented by a uniform positive charge (jellium) of density $n_+ = n_{sub}$ with a sharp boundary at the surface. The adsorbate, (Lang developed the theory specifically for alkalis), also has a uniform positive charge $n_+ = n_{ad}$ situated on top of the substrate as is shown in Figure 11. N_e electrons are added to produce charge neutrality in the system. To apply this to alkali adsorption, Lang simply used the bulk crystal spacing of the alkali to determine the thickness of the adsorbate layer, T. The coverage is allowed to vary through the parameter n_{ad}. The electron distribution ($n_-(x)$) is determined by solving Schroedinger's equation self-consistently for the electron wave functions, ψ_i, assumed to be plane waves. The work function is now evaluated according to equation (17). The chemical potential is a property of the bulk of the system, but the $\Delta\phi$ term is entirely determined by the electron distribution at the surface:

$$\Delta V = 4\pi \int_{-\infty}^{\infty} x[n_-(x) - n_+(x)]dx \tag{29}$$

Surprisingly good agreement has been found for this theory, which has no fitted parameters. When used to calculate ϕ's for bare surfaces 5-10% accuracy was achieved for simple ideal metals. The results for

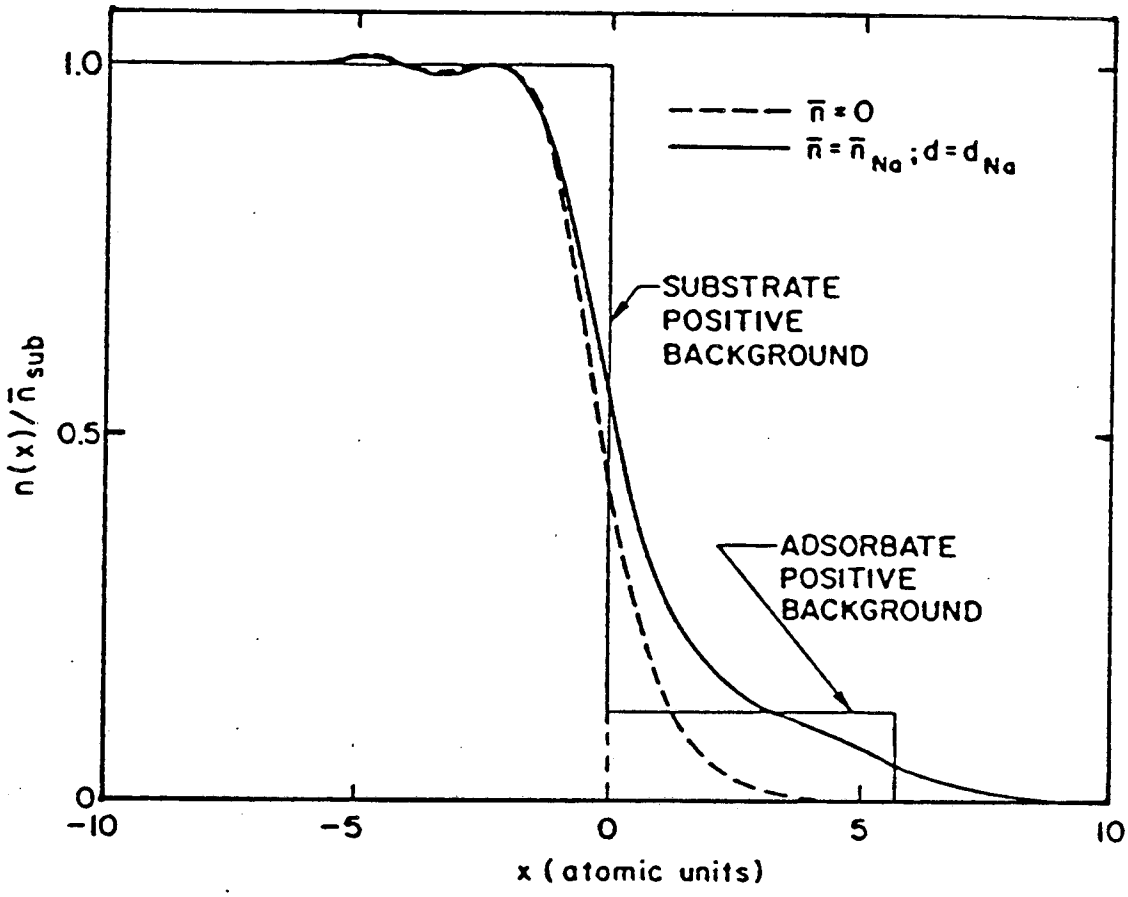

XBL 872-505

Figure 11. Lang's model for $\Delta\phi$ shifts for alkali adsorption. The rectangular blocks represent the constant positive charge background for the substrate and adsorbate. The smooth lines are the calculated negative charge density with (⊛⊛⊛⊛⊛⊛) and without (------) the alkali adsorbed. The oscillations in the electron charge density just inside the metal are expected on physical grounds and are one measure of the success of this model. From ref. 79.

alkali adsorption on metals were also quite impressive. The correct form of the $\Delta\phi$ vs. θ curve was obtained, i.e. a sharp initial decrease to a minimum, followed by a slight increase at θ=1. The value of the minimum for the various alkalis were all within the experimental range.

Lang was the first to raise the issue of how ϕ changes for the second layer of adsorbate atoms. He predicts a slight drop in ϕ at the start of the second monolayer, and he cites some experimental work purporting to see this effect, although Lang suggests that the experimental observation of this effect is probably complicated by second layer formation beginning before complete filling of the first. Lang also compares his calculated ϕ's after one full monolayer is adsorbed to ϕ's calculated for the bulk adsorbate. He finds these two values to differ by $\leq$0.05 eV which indicates that most of the $\Delta\phi$ occurs in the first monolayer.

The Lang jellium model has also been used by Yamauchi and Kawabe[81] to describe alkali adsorption. Instead of solving self-consistently for the electron wavefunction ψ_i each time, they proposed that a general analytical solution to the problem could be obtained by postulating a trial function for the electron population of the form:

$$(30) \qquad n_-(x,\beta) = \begin{cases} 1/2n_{sub}^2[2 - e^{\beta(x - \delta)}] & ; \quad x < \delta \\ 1/2n_{sub}^2 e^{-(x - \delta)} & ; \quad x > \delta \end{cases}$$

δ=th$\cdot n_{ad}/n_{sub}$ where th is the adsorbate layer thickness, and β governs the falloff of the electron population at the vacuum

interface, and is determined variationally. The expression for the work function change is:

$$\Delta\phi = 4\pi e n_{sub}(\beta^{-2} - \beta_0^{-2}) - 2\pi e n_{ad}(th - \delta)th \quad (31)$$

with β_0 the optimized value of β at zero coverage. As before, this expression can be understood as the formation of dipoles on the surface. The first term in $\Delta\phi$ is due to the spatial falloff of the electron population at the interface. The second term relates to dipole formation from imaging of the positive core charges in the surface. The application of this theory to alkali adsorption reproduces well both the initial dipole moment upon adsorption and the minimum in the $\Delta\phi$ vs. θ plot. However, it has a problem with coverages near a monolayer - instead of levelling out it continues to increase. Such behavior was ascribed to failure of the trial function to adequately describe the high coverage system. Lang's theory appears to fit the entire θ-range more reliably.

An ab initio calculation of Cs/W(001) has been presented by Wimmer et al..[82] They employ a refined approach to self-consistently solve the Schroedinger equation for lattices known as the full-potential linearized-augmented-plane-wave (FLAPW) method. Details of this calculation are given elsewhere[83], and the technique will only be briefly summarized here. In ab initio calculations, choice of basis set and potential ultimately determine the accuracy of the results. Augmented-plane-wave methods choose a basis made up of plane waves. If these functions are energy independent the resulting secular is linear, and the technique becomes LAPW. Finally

the potential is usually set constant in the interstitial region and a simple form is assumed within the region of the atomic core (known as a "muffin tin potential"). In FLAPW however, a better approximation is made for the full potential both in the interstitial region and within the cores by solving Poission's equation for assumed multipole charge distributions within each atomic core.

The model is constructed by considering a slab of W lattice atoms (in this case 5 layers), to represent the clean surface. The FLAPW method is now applied to give the electron density and ϕ for the bare surface. Cs is then added on the desired adsorption sites and the calculation repeated. In this manner either the change in electron density or the potential energy surface caused by Cs adsorption can be generated.

Some very definitive conclusions can be drawn from this calculation. The electron density difference plots show that rather than transferring electron density to the substrate the Cs nucleus actually gains electrons. This argues strongly in favor of a dipole induced mechanism for explaining $\Delta\phi$ for Cs adsorption, as opposed to the charge-transfer image dipole idea which has received much attention in the theories discussed thus far. By considering the effects on $\Delta\phi$ from the valence charge separately from those caused by the core charge, it was shown that the two contributions are opposing. The dipole moment from the valence charge provides a large dipole moment with it's positive end pointing outward, thereby lowering ϕ. A smaller dipole moment is contributed by the Cs core charge, pointing in the opposite direction. Both of these effects can be seen in a 3-d plot of the potential at the surface shown in

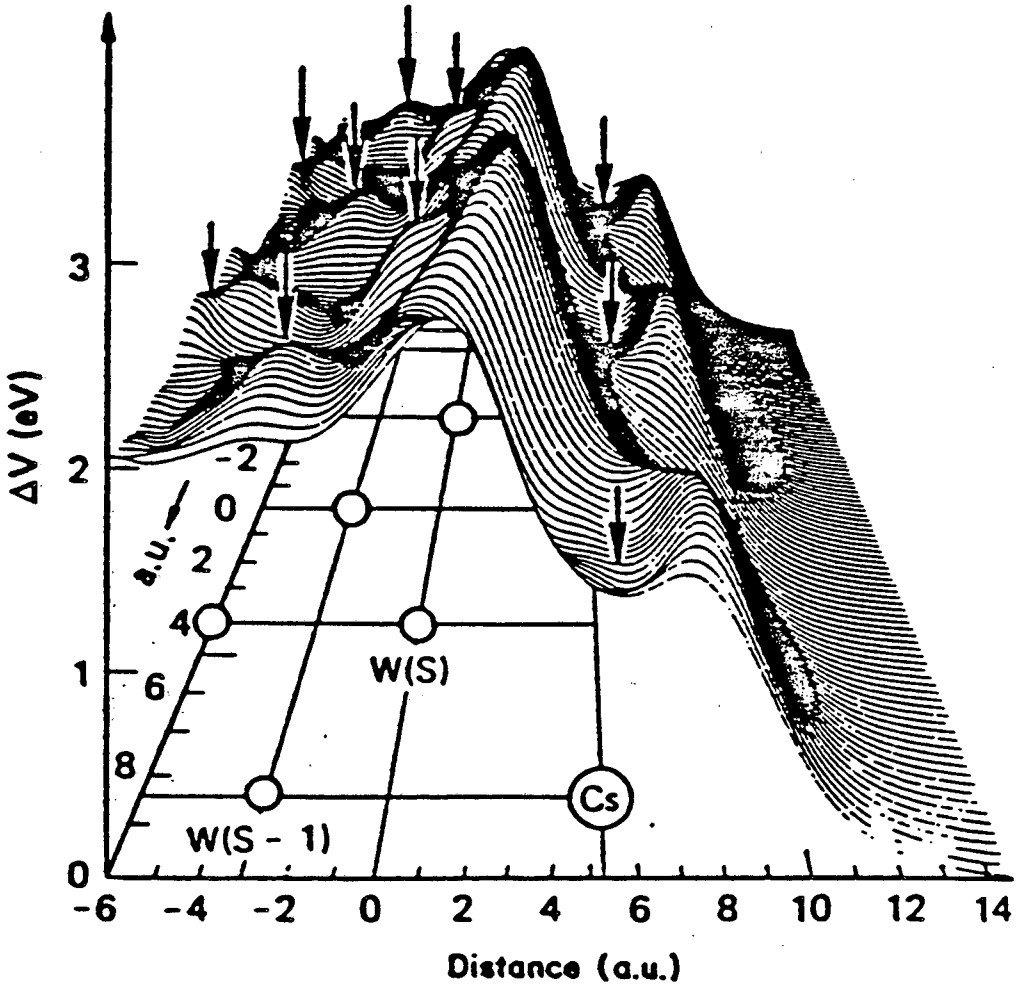

Figure 12. The change in Coulomb potential due to Cs adsorption on W(001) according to the FLAPW calculation of Wimmer et al.. The initial large change centered between the Cs and W layers is due to the polarization of the Cs valence charge and the opposing dip centered right at the Cs atoms can also be seen. The arrows indicate the location of the atoms. From ref. 82.

Figure 12. The initial large drop at the interface between the W atoms and the adsorbed Cs is due to the valence dipole while the second small rise centered on the Cs atoms is from their core dipole moment. An overall $\Delta\phi$ can also be computed by this method, and it is found that increasing the distance of the Cs from the surface atoms serves to reduce $\Delta\phi$. From this dependence they estimate a Cs-W distance of 3.1 Å to obtain agreement with the experimental determination of $\Delta\phi$ for Cs/W. A value for this distance has not been determined experimentally. Although in applying this theory, a calculation must be performed for each specific system to predict a $\Delta\phi$, the mechanistic information obtained from the results appears to be both unique and highly informative.

In recent work, Ning[84] and co-workers have combined the jellium model of Lang with the slab model of Wimmer. The motivation is that the slab model cannot treat a continuous change of coverage. This is overcome by using three layers of W as the slab and simulating the adsorption of Cs with a jellium coating of appropriate thickness. As before, the coverage may be altered by increasing the concentration of positive charge (n_{ad}) in the jellium layer. The resulting ϕ vs. θ curve is shown in Figure 13, as applied to Cs/W. It succeeds better than the simple jellium model at low coverage as expected since the approximation of a continuous sheet of adsorbate becomes poor at low coverages. This model also does better than the jellium model alone in predicting the coverage at which the minimum in ϕ occurs, however, it overestimates the magnitude of this minimum by $\approx$1 eV. This discrepancy was ascribed to neglect of the core electrons of Cs which according to Wimmer et al. made a positive contribution to $\Delta\phi$.

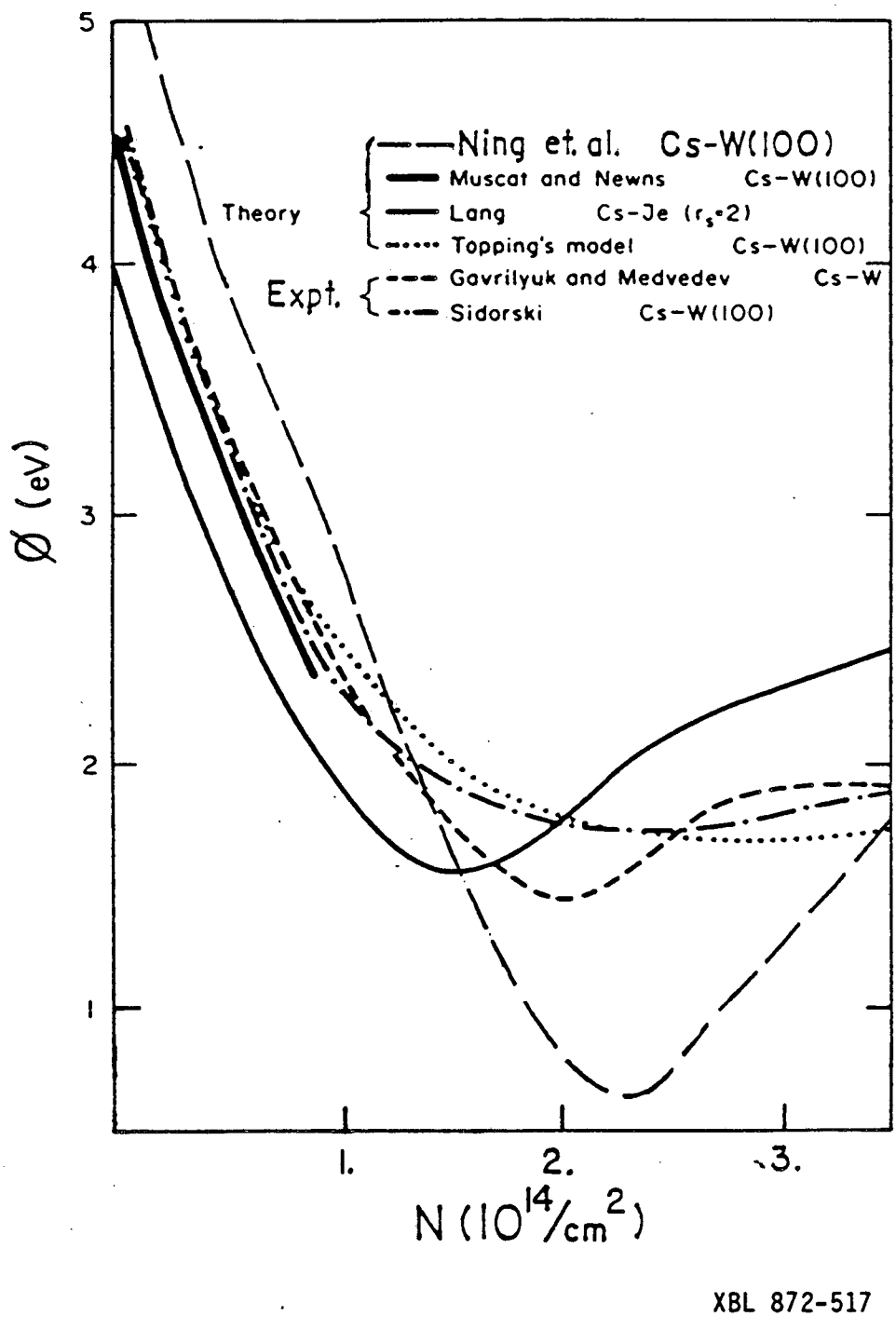

Figure 13. Comparison of four of the theories presented here as applied to $\Delta\phi$ shifts for Cs/W. Surprisingly, all theories reproduce the basic trend quite well. After ref. 59. The experimental references are V.M. Gavrilyuk and V.K. Medvedev, Fiz. Tverd. Tela, 8, 1811 (1969); Z. Sidorski, J. Pelly and R. Gomer, J. Chem. Phys., 50, 2382 (1969).

Finally, a truly novel method for $\Delta\phi$ shifts has been presented by Shustorovich and Baetzold in a series of papers.[85] To develop this theory, one unit cell of the substrate is replaced with a two-layer slab - one representing the bulk layers, and another for the surface. These slabs are in turn represented by LCAO-MO's generated from one set of valence orbitals for the substrate, the d and p orbitals. Chemisorption is represented with perturbation theory, which mixes the original orbitals of the two different slabs. The key to determining the work function shift is in the mixing of the surface p and d orbitals. If the symmetric combination is taken, the resulting MO has its largest lobe directed into the surface, which by the familiar argument results in a negative $\Delta\phi$. Conversely, the antisymmetric combination of the surface p and d orbitals results in an increase in $\Delta\phi$. This is shown diagrammatically in Figure 14. It is the weighting of the coefficients of these two mixed LCAO-MO's that will determine the surface's contribution to the $\Delta\phi$. The inclusion of this surface rehybridization term in $\Delta\phi$ is the essential element of this theory. The total $\Delta\phi$ is expressed as a sum of this surface polarization with a charge transfer part, such as has been invoked previously. Shustorovich and Baetzold contend that the charge transfer is usually towards the adsorbate since it is usually more electronegative, resulting in a work function increase. Thus it is the tradeoff between these two terms which allows some particularly troubling experimental data to be explained. An example is the observation of a change in the sign of $\Delta\phi$ for some atomic adsorbates on different crystallographic faces of the same material. In addition, this theory is corroborated by predictions it

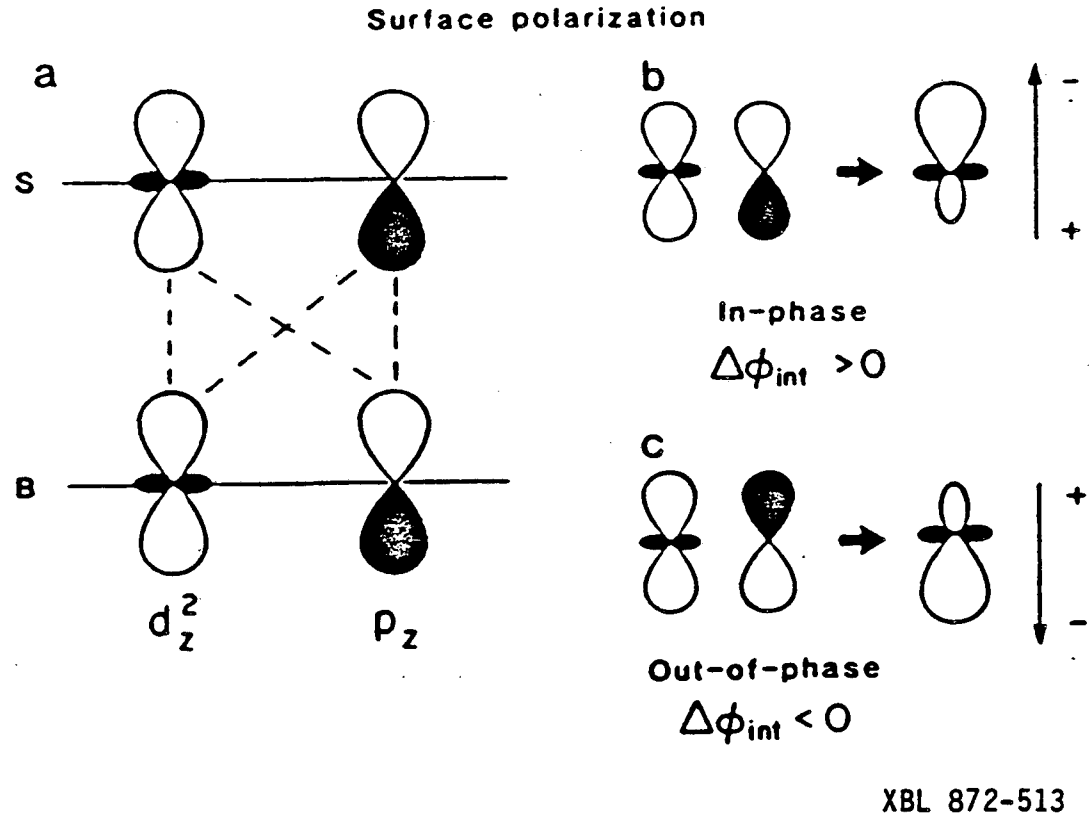

Figure 14. Shustorovich and Baetzold's description of $\Delta\phi$ effects as a mixing of the surface and bulk wavefunctions represented by the orbitals shown in a). These mix and form either the in-phase combination leading to a positive $\Delta\phi$ in b), or the reverse in c). The overall $\Delta\phi$ will be the sum of this term plus the contribution due to charge transfer between the adsorbate and surface. From ref. 85.

successfully makes for the bare surface work functions of different faces of the same material.

Figure 13 compares the results of several of the theories reviewed above for the coverage dependence of the work function for Cs/W. Results from two experimental determinations are also shown. This figure serves also to emphasize that the bulk of the theoretical work has been aimed at explaining adsorption of the alkalis, one of the few types of systems studied in detail experimentally. As is seen in the figure, all of the theories fit the experimental curve fairly well, from the recent sophisticated treatment of Ning et al. to the early phenomenological relation of Topping. Certain specific features are described better by some theories than others, but they all reproduce the general trend of the data quite well. However, the information obtained from each of these theories is very different. For the Topping equation, for example, the dipole moment and polarizability in the equation serve for the most part as fitting parameters, and comparison and interpretation of these values must be done with caution. In contrast, the theory of Lang is quite satisfying in it's prediction of $\Delta\phi$ adsorption changes, because no fitting parameters are used. Although they cannot be used to generate the type of plot displayed in Figure 13, the theories of Wimmer, and Shustorovich and Baetzold also deserve praise since they provide insight into the mechanism behind the work function lowering in terms of the rearrangement of the electron density due to adsorption.

B. Experimental Studies of Work Function Shifts

Work function changes have long been routinely used in the experimental characterization of adsorbate/surface systems. The first systematic study was done by Mignolet in 1950.[86] He found that a variety of adsorbates (Ar, Xe, He, N_2, and ethane) on Ni films caused a lowering of the work function. This work established the surprising result that even physisorbed molecules exhibit significant work function changes. Beginning in 1958, Gomer and co-workers extensively studied noble gas adsorption using the novel technique of field emission to determine the $\Delta\phi$ shifts. Noble gases are regarded as the model physisorption system for determining these effects. Table 2 is meant to show a representative sampling of the different types of systems that have been reported and the range of $\Delta\phi$ values typically observed. A comprehensive compilation of experimental work function changes, through 1976, is given in a review article by Holzl and Schulte.[5]

Whereas the coverage dependence of $\Delta\phi$ for alkali atoms is known to go through a minimum before a monolayer coverage, and several of the theories discussed above duplicated this trend, most of the systems in Table 2 do not display this type of behavior with respect to coverage. Instead a monotonic decrease of $\Delta\phi$ is usually observed levelling off at a monolayer. Some exceptions do exist, however. Examples can be found in Wang and Gomer's results for Xe/W(100)[66] and also in Palmberg's study of Xe/Pd(100)[67] both of which display a minimum in the θ-dependence of $\Delta\phi$.

Strong chemisorption can give rise to a unique $\Delta\phi$ coverage dependence for adsorption on single crystalline surfaces. The

Table 2: Experimental work on adsorbate-induced work function shifts.

System	Method	$\Delta\phi_{mono-clean}$ [a] (eV)	$\Delta\phi_{multi-mono}$ [b] (eV)	Ref.
Fe/Ag(111)	UPS[c]	0.90	-0.07	87
Xe/Ag film	UPS	-0.47	-0.13	88
Xe/W film	field emission[d]	-1.30	-0.20	102
Ar/W film	field emission	-0.80	0.60	102
Xe/W(110)	vibrating cap.[e]	-0.43	0.	66
Xe/W(100)	vibrating cap.	-1.05	0.	66
Xe/W(110)	field emission	-2.40	0.	89
Xe/W(100)	field emission	-1.35	0.	89
Xe/Pd(100)	vibrating cap.	-0.94		67
Xe/Ag film	photo-yield[f]	-0.75		90
Xe/Ag film	vibrating cap.	-0.45		91
Xe/Ag film	diode	-0.47		92
CO/Ag film	vibrating cap.	<-0.30		91
H_2/Ag film	diode	0.32		92
acetylene/Pt(111)	vibrating cap.	-1.42		93
ethylene/Pt(111)	vibrating cap.	-1.00		93
ethylene/Ag(110)	UPS	-0.16		94
ehtylene/Ag film	photo-yield	-0.36		95
benzene/Ag(110)	UPS	-0.60		94
benzene/Pt(111)	vibrating cap.	-1.52		96
toluene/Pt(111)	vibrating cap.	-1.63		96
aniline/Pt(111)	electron irrad.	-1.8		105
nitrobenzene/Pt(111)	electron irrad.	-1.5		105
pyridine/Pd(111)	UPS	-1.15		97
pyridine/Ag film	UPS	-1.92		98
pyridine/Ag film	electron irrad.	-1.85		106

[a] Work function of monolayer surface minus that of the clean surface.

[b] Work function after multilayer adsorption minus that of the monolayer. If not shown, multilayer adsorption not observed.

[c] Work function evaluated by the spread in electron energy obtained from Ultraviolet Photoelectron Spectroscopy.

[d] Work function evaluated through the dependence of the emission current with the applied field.

[e] Contact Potential measurement.

[f] Work function evaluated through the dependence of the photoemission yield on the energy of the exciting photon.

strength and structure of an adsorbate at a particular crystallographic site will of course affect its contribution to the surface dipole moment, which, according to the Helmholtz equation (eqn. (19)) is directly proportional to the work function. As the availability of specific sites will change with increasing coverage, so will ϕ. An example of this is CO/Pt(111)[99] where dramatic reversals in the sign of $\Delta\phi$ are observed and assigned to adsorption of the CO linearly at 3-fold sites at low coverages followed by population of 2-fold bridge sites at higher coverages. The work function changes occur because the latter bonding site has been shown to have a zero dipole moment. Self depolarization of the molecules was also hypothesized to contribute to the measured $\Delta\phi$ changes in these experiments.

Table 2 also shows several results of $\Delta\phi$ for the same system, yet determined by different techniques. Although each method certainly has its drawbacks and advantages the most direct measure of a work function shift is accomplished by the vibrating capacitor method which measures the actual contact potential between the surface under study and a reference surface. Alternatively, both the field emission and photoelectric yield techniques require an assumption regarding the dependence of the measured yield or current versus either an accelerating voltage or the wavelength of the exciting light, respectively. Although this assumption is theoretically well understood for clean surfaces, the validity of applying the same relations to an adsorbate covered surface has been questioned. In particular, for the photoelectric determination it has been shown[100] for O_2/Mg(100) that the dependence of the photoemission yield on the energy of the exciting photon in the

presence of adsorbates deviates from the clean surface relation. Better agreement between photoelectric and contact potential measurements was obtained for the adsorbed case if a slightly different empirical functional form relating the yield to the photon energy was assumed. A change in the quantum mechanical transmission coefficient through the interface was suggested as the underlying reason for the difference. In another comparison of photoelectric yield versus contact potential $\Delta\phi$ determinations,[101] it was suggested that differences may be related to inhomogeneities on the surface. The latter method gives rise to an area average work function across the surface, while the former tends to weight any lower work function patches more heavily. Thus low work function island growth was postulated in the coadsorption of alkalis and halogens to explain the discrepancy between the two work function measurements.

A quick review of the literature convinces one of the generality of the result that an adsorbed layer of molecules changes (and in most cases lowers) the work function. It is not quite so easy to ask how much of this effect is due to the first layer and how much may be attributed to multilayer adsorption. As noted above, Lang[79] theoretically predicted a small change in ϕ for mulitlayer formation for the specific case of alkali adsorption, and cites a few experimental examples for which small changes in ϕ were observed at the start of the second layer. However, he predicted that the work function after one monlayer would lie very close to the ϕ for the bulk adsorbate. Much of the experimental $\Delta\phi$ data in the literature is for chemisorbed systems for which no additional layers beyond the first exist.

The most complete discussion of multilayer $\Delta\phi$ effects for physisorbed systems is due to Gomer[102,103,104] in a set of early papers employing the novel method of field emission to study noble gases physisorbed on W surfaces. The emission changes observed for second and third layer formation were interpreted as further changes in ϕ (these values are shown in Table 2). However, Gomer interprets the emission changes with a model which includes the dielectric effect that multilayers will have on the field felt at the metal surface, and the competing effect of an increased probability of electron tunneling due to the presence of the adlayer. Field emission occurs via a tunneling mechanism through the potential barrier created by the very high fields used, and the adlayer is hypothesized to provide hopping sites for the emitted electrons, thereby increasing overall emission. This is shown in Table 2 where Xe multilayers are responsible for an apparent decrease in ϕ while the opposite effect was reported for Ar multilayers.

Later, Wang and Gomer[66] repeated these noble gas adsorption experiments, this time measuring $\Delta\phi$ with the more direct method of the vibrating capacitor which yields the contact potential. In these experiments no change in work function was observed for multilayers. Table 2 also summarizes the experimental work reporting $\Delta\phi$ changes past the first layer for physisorbed systems. A can be seen, even when these multilayer effects are observed they are quite small.

Confining $\Delta\phi$ shifts to the first monolayer is consistent with the ideas presented above in the theory section since changes were postulated to be either due to charge transfer with the substrate or interaction with the short-ranged surface fields for molecules with

no permanent dipole moments. It is conceivable that an adsorbate with a permanent dipole moment could exhibit further work function shifts if the adsorption were ordered, but in most cases multilayer adsorption is seen to be amorphous for large organic adsorbates. Gland and Somorjai[105] did observe weak ordering for a series of aromatic molecules on Pt surfaces, but the molecules were chemisorbed and therefore only monolayers were formed. There are few experimental $\Delta\phi$ measurements for physisorbed aromatic molecules, but one example shown in Table 2 is pyridine/Ag films where Eesley found that $\Delta\phi$ saturated at one monolayer (i.e. no multilayer $\Delta\phi$ effects).[106] Based on the considerations above, and the lack of any experimental evidence to the contrary, it appears reasonable to conclude that almost all of the work function change upon adsorption will be exhibited in the first monolayer.

IV. Experimental Procedure

The experiments were performed in a standard UHV vacuum chamber, typically operating in the low 10^{-10} torr region. The set-up is shown diagrammatically in Figure 15a. The Ag(111) surface (oriented by Laue diffraction), was mechanically polished in seven steps, the finest at 0.05 μm. It was then chemically polished in a chromate solution (100 ml saturated $K_2Cr_2O_7$, 2 ml saturated NaCl, 10 ml concentrated H_2SO_4, and 110 ml H_2O). Preceding each experiment, the crystal was Ar^+-ion sputtered for 10 minutes, and then annealed at 620 K for another 10 minutes. The sample was then cooled to $\approx$90 K by flowing liquid N_2. Molecules were dosed by raising the total chamber

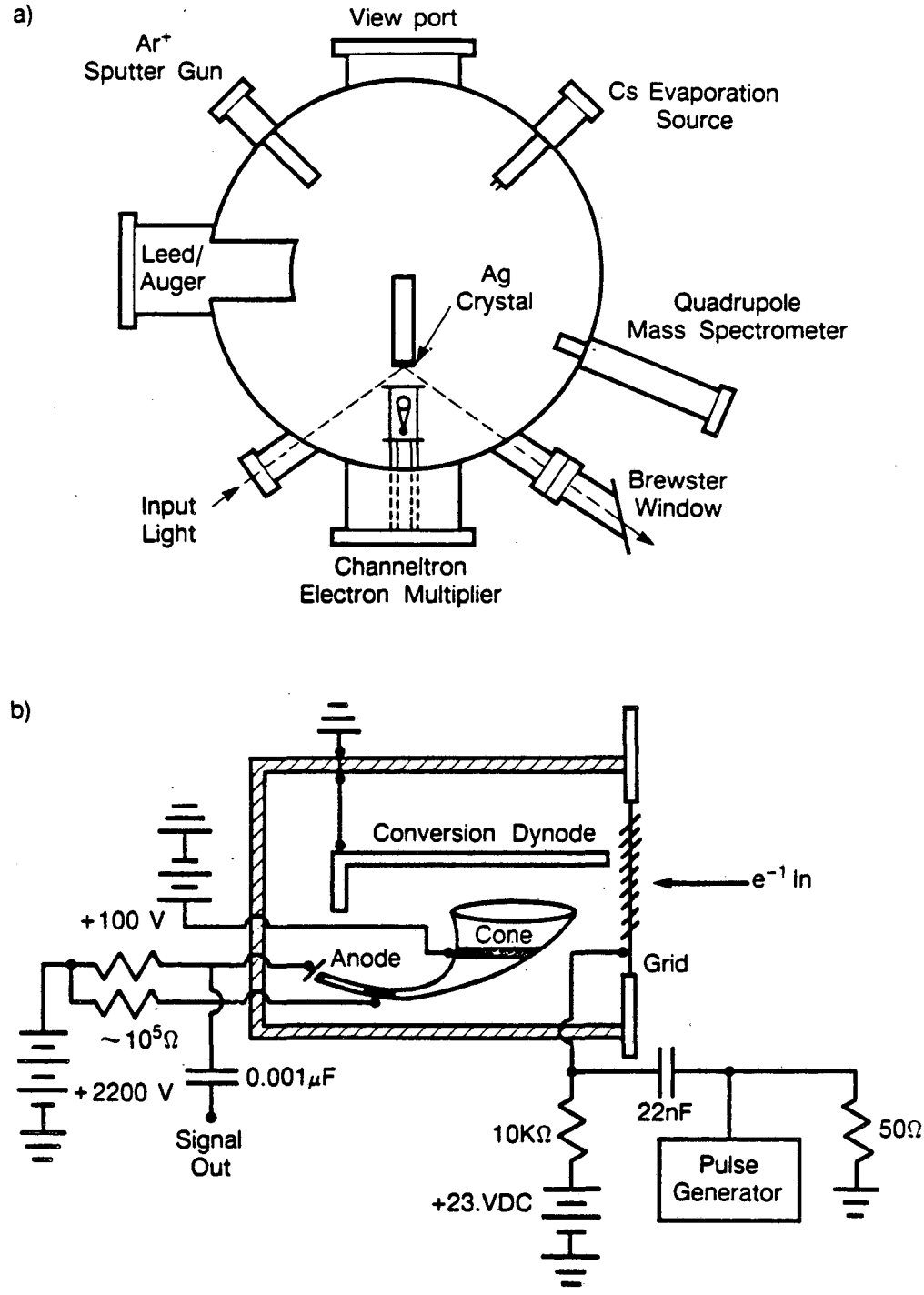

XBL 868-8915

Figure 15. a) Schematic of the UHV chamber used for the photoemission yield experiments. The Ag crystal could be rotated in the plane of the paper around the center of the chamber. b) Details of the Galileo 4870 off-axis channeltron detector. The conversion dynode and the shield surrounding the detector are stainless steel. See text for further description.

pressure for the required time (1 Langmuir (L) = $1.x10^{-6}$ torr-sec). No attempt was made to correct for the ion gauge reading for different molecules. Calibrations performed earlier using ellipsometry indicated that for benzene/Ag 5 L equalled one monolayer.[107] The films studied here ranged from 0-100 L, or approximately 0-100 Å. The sample could be resistively heated via a button heater in thermal contact with it. For the photoyield thermal desorption experiments described below, this proved unsatisfactory due to interference from thermionic emission from the heater. For those experiments, the sample was heated slowly (≈0.3°/s) by circulating warm N_2 through the cooling line.

Experiments were also performed on an optical flat of Infrasil quartz. Initial attempts indicated that the surface was contaminated because of the large photoyields observed. In situ annealing seemed to accelerate the problem, suggesting that the contamination may have been caused by diffusion to the surface of bulk impurities. A clean surface was finally obtained by etching the quartz for three minutes prior to installation in 20% HF/H_2O. This succeeded in reducing the quantum yield at 266 nm less than 10^{-2} of that observed from Ag. Charging of the quartz was noted for laser exposure times of many minutes. The charge dissipated after removing the laser over a period of 15 minutes (faster if the applied voltages were also removed). This problem was avoided by exposing the sample to the laser only for the time needed to make a measurement (on the order of 30 seconds).

The samples used were of the highest purity availible. Dissolved gases were removed before using by freeze-pump-thaw cycles,

and samples were dosed into the chamber through a leak valve from an inlet line pumped to 10^{-4} torr.

The excitation light was from either a pulsed Molectron YAG laser, or a 150 W Xenon arc lamp. Usually, the 4^{th} harmonic of the YAG (266 nm = 4.66 eV) was used. The light was successively apertured to result in a 1 mm diameter incident beam on the crystal at 65° from the normal. Since any stray light reflections within the chamber generated background electrons, the reflected light exited the chamber through a Brewster window.

When using the arc lamp, it was dispersed through one side of a double monochromator with slits to give a 5 nm bandpass. The monochromator was scanned via a stepper motor under computer control. The output from the monochromator was collimated using a quartz lens, and was also focussed onto the crystal with a 300 mm focal length quartz lens. Even though focussed, the arc-lamp had a similar sized beam at the crystal.

The laser light was primarily p-polarized, but little polarization effect was seen. The laser pulse energy was monitored just before entering the chamber with a Molectron J-3 energy meter, and further attenuated using calibrated metal-film neutral density filters. Incident intensities were usually kept below 10 W/cm^2, the point at which damage to the molecular film was observed. The cause of this damage is not completely understood. A pulsed heating calculation[108] indicates that the temperature rise induced by such incident intensities would be $< 10^{-3}$ K on Ag, even assuming of 0% reflectivity and all the light absorbed at the surface. Damage by the photoelectrons themselves is also a possibility although the

damage seems to correlated more with pulse energy than photoelectrons produced. Reports of electron irradiation damage in the literature indicate values of 0.5 decomposition events per 100 eV of energy absorbed,[109] for electrons of ≈10 eV. Greater damage was reported for thicker films, consistent with the results here. This damage yield number is for continuous electron irradiation and is much too small to account for the damage observed here. Higher damage yields however, might be consistent with the large peak irradiation intensities obtained with the 20 ns laser pulse (10^{-7} A/cm^2 peak intensity compared to the $5x10^{-5}$ A/cm^2 reported to destroy a monolayer with 10 seconds of continuous radiation[109]).

The details of the electron detection are shown in Figure 15b. The detector was a Galileo 4870 Channeltron. It was constructed such that it's entrance cone was not on a line of sight with the crystal. Earlier experiments using a channelplate detector resulted in undesirable background from detection of scattered photons by the plates themselves (the quantum yield of the channelplates for 266 nm photons was found to be $7x10^{-9}$ electrons/photon). The channelplate also exhibited a faster output pulse, and this signal proved hard to detect except via pulse counting techniques. The channeltron was located behind a stainless steel mesh grid which was situated approximately 2 cm directly in front of the sample. The grid was biased at +23 V with respect to the crystal, determined by finding the smallest voltage for which no appreciable change occurred in the photoyield signal. For this reason it is believed most of the photoemitted electrons were detected. The large background of charged species generated by the ion pump was sufficient to saturate

the channeltron. Installing a biased grid between the pump and the detector only partially rectified the problem. Partial closure of a gate valve on the ion pump finally eliminated this source of noise.

The time-resolved experiments employed a Biomation transient recorder with a 10 ns channel width. The collected photoyield signals showed a FWHM of 20 ns, presumably reflecting the width of the laser pulse. To avoid saturation of the detector when observing the tail of the photoyield pulse, a ≈100 ns, -30 V, electrical gating pulse supplied by an HP 212A pulse generator was applied to the grid simultaneous with the laser pulse. This resulted in a rejection ratio of the 'prompt' electrons of approximately 10^3. The coverage dependent data using the laser/Biomation were collected by successively dosing the crystal, and then turning the voltages and laser on to take data both without ('prompt' emission) and with ('delayed' emission) the electrical gating pulse. When the arc-lamp was used, the output of the channeltron was amplified x100 before being sent to a discriminator and pulse counted. For these experiments, the photoyield could be monitored while continuously dosing the crystal. This method resulted in better, more reproducible data, although the data from the two methods agreed quite well.

The bare Ag surface was characterized via photoemission in two ways. Figure 16 shows an intensity dependence of the photoemission excited with the laser at 266 nm. This linear plot (slope = 0.9) verifies that only single photon photoemission is being monitored. Saturation observed for the higher energy points limits the useful dynamic range to approximately one order of magnitude. The data

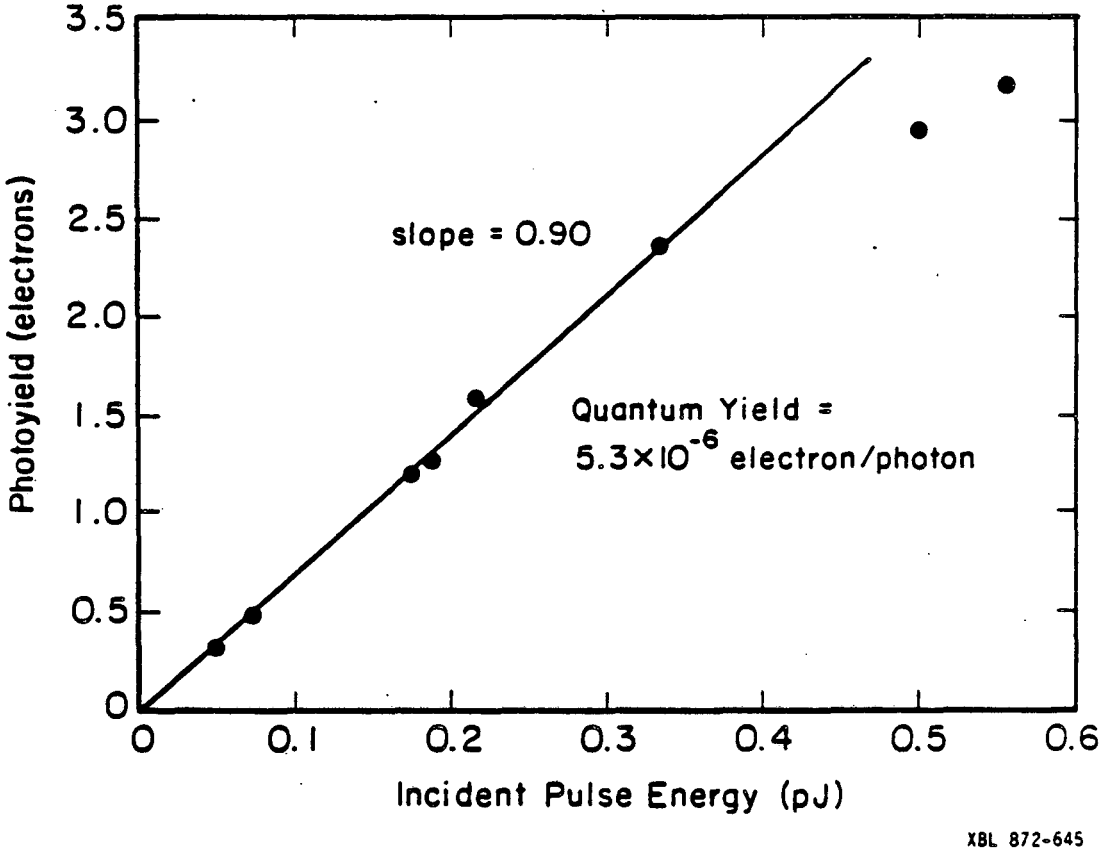

Figure 16. Laser intensity vs. detected photoyield signal for bare Ag(111), using 266 nm radiation. The linear relation verifies that only single photon emission is being probed.

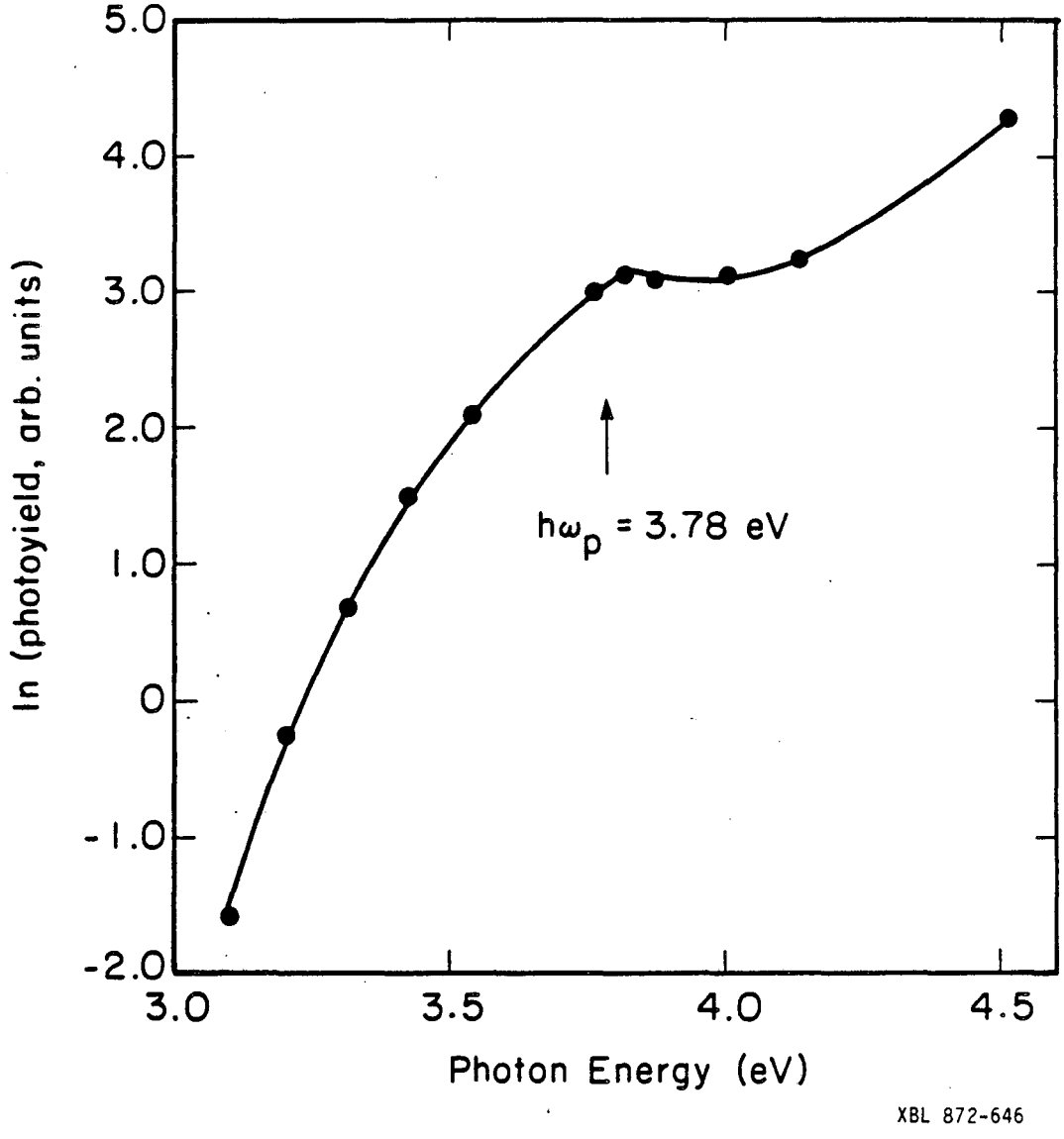

Figure 17. Arc-lamp excited spectrum showing the energy dependence of photoemission from clean Ag(111) below the workfunction (ϕ = 4.66 eV). The arrow indicates the position of the bulk plasmon for Ag. The temperature is 90 K.

shown in Figure 16 indicate a quantum yield (at 266 nm) of $5x10^{-6}$ electrons/photon, which is typical of the values measured here.

Figure 17 shows a plot of the bare Ag photoemission vs. incident photon energy collected with the arc-lamp. The data has been corrected for the variable output of the Xe lamp. Since the reported work function for Ag(111) is 4.66 eV,[110] all of the data in Figure 17 is below ϕ. The feature at 3.8 eV is due to the minimum in reflectivity which occurs at 3.78 eV, the bulk plasmon energy of Ag.

V. Results and Discussion

A. Molecular Coverage Dependence of the Photoemission Yield

The behavior of the total photoemission yield with respect to film thickness is displayed in Figure 18, for anisaldehyde on Ag(111). A sharp rise in the yield is seen over the first few Langmuirs of coverage, and after that a slower, monotonic decrease. This trend held true for all the various molecules tested. It is believed that the initial rise is attributable to a work function change of the metal surface, and that the decrease in the yield following is due to attenuation of the photoelectrons by the film. The discussion of the dependence of the yield with film thickness will be divided along these two lines.

1. Work Function Effects

Changes in the work function of a metal surface upon molecular adsorption are well documented (e.g. see Table 2). As discussed in part II, based on both theoretical and experimental considerations, it is reasonable to conclude that this work function shift occurs for

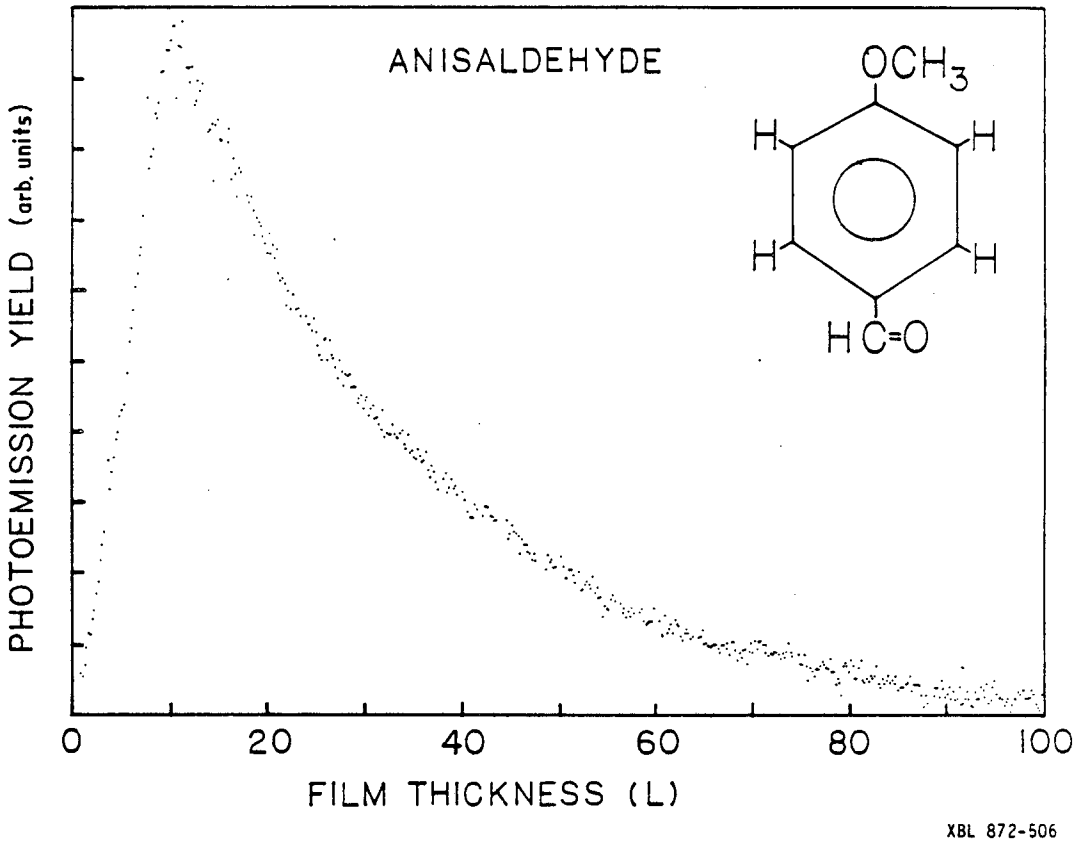

Figure 18. The dependence of the photoyield on increasing film thickness (coverage). The initial rise is due to the $\Delta\phi$ for anisaldehyde/Ag, while the decrease is caused by attenuation of the photoelectrons by the film.

the initial monolayer adsorbed. To quantitate the hypothesis that the rise in Figure 18 can be explained as a $\Delta\phi$ shift, an expression relating the photoyield to film thickness (coverage) will be needed.

The Topping equation (eqn. 24) is a simple, phenomenological, expression relating the work function shift, $\Delta\phi$, to the surface coverage, dipole moment, and polarizability of an adsorbate. In order to make use of this equation here, the dependence of the photoemission yield Y, on ϕ is needed. For the case of the exciting radiation $h\nu >> \phi$, $Y = A(\phi - h\nu)^2$, where A is a constant.[111] This is appropriate because the excitation wavelength is 266 nm (4.66 eV) which is already above the unperturbed work function of bare Ag(111) (ϕ = 4.46 eV[110]) and the work function decreases further yet upon adsorption. Combining this relation for Y with eqn. 24 for $\Delta\phi$, Y as a function of N, adsorbate surface density, is obtained:

$$(32) \qquad Y(N) = A\left[(\phi_0 - h\nu) + \frac{2\pi e p_{eff} N}{1 + 9\alpha N^{3/2}} \right]^2$$

where α and p_{eff} are the polarizability and effective dipole moment of the surface adsorbed molecule. The case for mobile adsorption (adsorbates arrange themselves on a regular lattice at all coverages), is implied in eqn. 32, although both the mobile and immobile cases were considered, and found to not give distinguishable experimental fits. Finally, if eqn. 32 is divided by Y(N=0), the constant A can be eliminated, and substituting $N=\Theta N_1$ (Θ=1 being one monolayer), results in the following :

$$(33) \qquad Y(\theta) = \frac{Y(0)}{(\phi_0 - h\nu)^2}\left[(\phi_0 - h\nu) - \frac{2\pi e p_{eff} N_1^{-1/2}\theta}{N_1^{-3/2} + 9\alpha\theta^{3/2}}\right]^2$$

This equation can now be fit to experimental data, assuming reasonable values for the polarizability and surface density. α = 13 $\AA^3$ for anisaldehyde was estimated by comparing to known gas phase values for similar molecules.[112] N_1 was determined by comparision to estimates made of the monolayer coverage for benzene/Ag.[113] This value of 3.0×10^{14} /cm^2 probably represents an upper limit owing to the larger molecular volume of anisaldehyde, so N_1 for anisaldehyde/Ag was chosen as 2×10^{14} /cm^2. In Figure 18 the photoyield peak occurs at 10 L of anisaldehyde, and this point was chosen as one monolayer (θ=1). This value is reasonably close to ellipsometric calibrations performed previously in this laboratory for benzene/Ag indicating one monolayer was about 5 L.[107] After selecting these values, eqn. (33) was fit to the experimental data of Figure 18 by varying p_{eff}. The fitted data is shown in Figure 19, obtained with a p_{eff} of 1.0 D, which is significantly smaller than the gas phase dipole moment of anisaldehyde of 3.26 D.[114] In the Topping model, p_{eff} represents the total perpendicular surface dipole. Ignoring contributions via charge transfer to the surface, consistent with a physisorbed system, the effective dipole is constructed from the alignment of the permanent moment of the molecule plus any induced moment produced via polarization by surface fields, which as shown in Figure 8 b) will contribute to a decrease in ϕ. Thus, the Topping model implies that the permanent dipole of the adsorbed anisaldehyde is not aligned with it's positive end

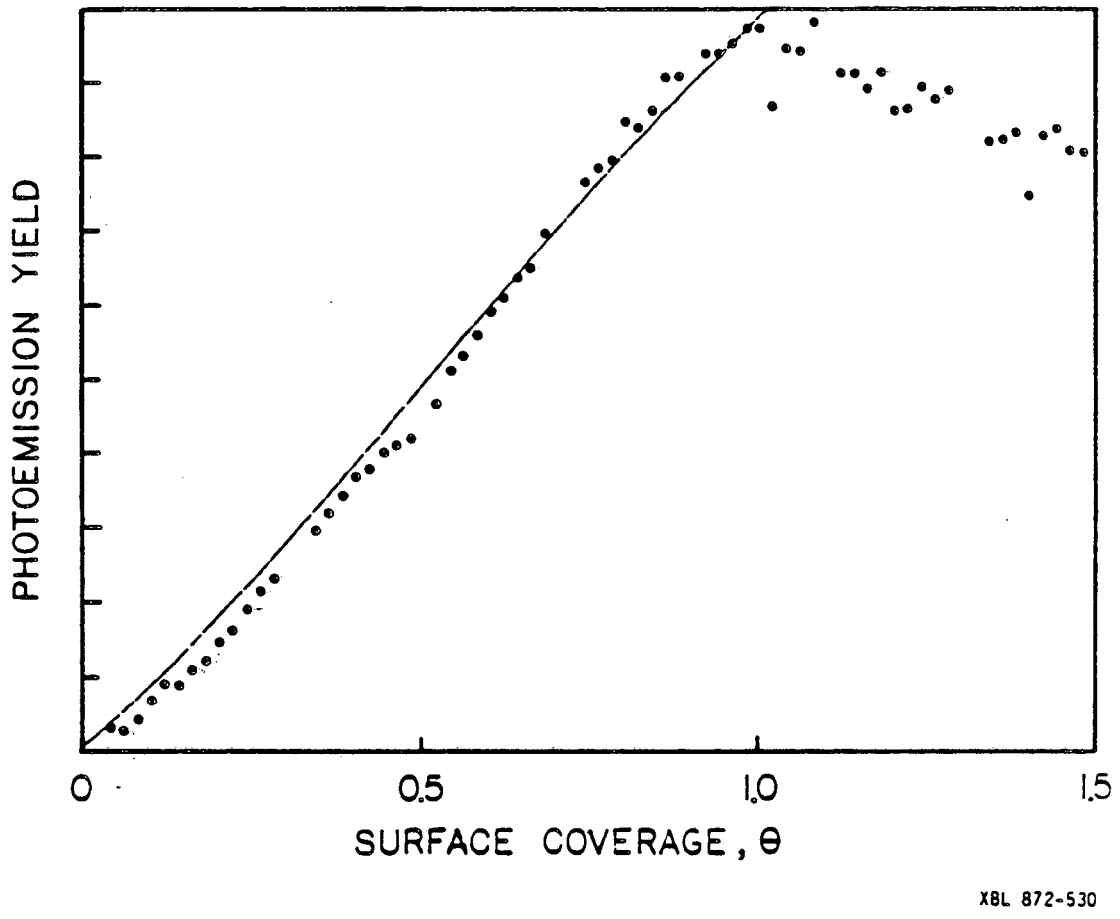

Figure 19. The fit of the Topping equation (solid line) to the photoemission yield data for anisaldehyde/Ag. Parameters used are $N_1 = 2.0 \times 10^{14}$ /cm^2, $\alpha = 13$ Å^3, $p_{eff} = 1.0$ D.

directed outward. Either a flat adsorption geometry, or one with some small component of the permanent dipole perpendicular to the surface would result in an effective dipole consistent with the Topping model.

When these parameters are substituted back into the Topping equation the $\Delta\phi$ for one monolayer is found to be -0.28 eV. This appears to be rather small when compared to $\Delta\phi$ for other aromatic molecules such as found in Table 2. As discussed in part II, the Topping equation has been successfully employed to fit results as diverse as the strong chemisorption of alkalis on transition metal surface[55,56] to the physisorbed system of a rare gas on Pd[67]. There has not been a careful coverage dependent study of $\Delta\phi$ for a physisorbed organic adsorbate, and it is possible the Topping equation fails to accurately describe the $\Delta\phi$ created in these large, weakly adsorbed systems. Another problem in using eqn. (33), is the proportionality assumed between the photoyield and ϕ: $Y \propto (h\nu - \phi)^2$. This relation, known as the Fowler law certainly holds well for clean surfaces, but deviations have been observed for adsorbate coated systems. In particular, Lange et al.[100] found empirically that better agreement between photoelectric and contact potential measurements for O_2/Mg were obtained when a variable exponent was used in the yield expression. They tentatively suggested this might be related to a change in the electron transmission coefficient at the surface.

To summarize, a fit of the coverage dependence of the photoyield for anisaldehyde/Ag results in a p_{eff} of 1.0 D, and a value for $\Delta\phi$ of -0.28 eV, which appear to be too small when compared to similar

molecules. A direct measure of the $\Delta\phi$ for this system, e.g. by contact potential, would allow the assumptions involved in this photoelectric yield determination of ϕ to be tested.

2. Electron Attenuation by Multilayers

The monotonic decrease following the peak in the photoyield at one monolayer is believed to be caused from electron attenuation by the succeeding layers. In part I, the two-stream theory due to Bader et al.[19] was used to treat electron transmission through condensed organic films, resulting in eqn. (2) for the transmitted current. With the further assumption that only unscattered electrons are detected, eqn. (2) predicts an exponential decrease for the transmitted photoyield with film thickness, with a characteristic falloff or mean free path (MFP) given by the 1/e distance of the yield. Many of the studies done in this area (see part I) have assumed such an exponential attenuation. That the photoyield data for anisaldehyde/Ag is also well described by such a relation is exhibited in Figure 20, a plot of film thickness vs. ln(yield). The MFP for this data is 30 L, although a relatively large deviation of values in the range of ≈7-30 L has been observed. Using the calibration mentioned above this MFP corresponds to a few monolayers. Comparision to literature is afforded by Table 1 (part I). Although the more careful work shown in this table suggests that MFP's generally tend to be on the order of only one monolayer, the MFP is energy dependent, a point illustrated well by Figure 3 for the MFP of Xe films on Pt.

The energy of the photoelectrons emitted in this experiment can be estimated from the difference between the energy of the exciting

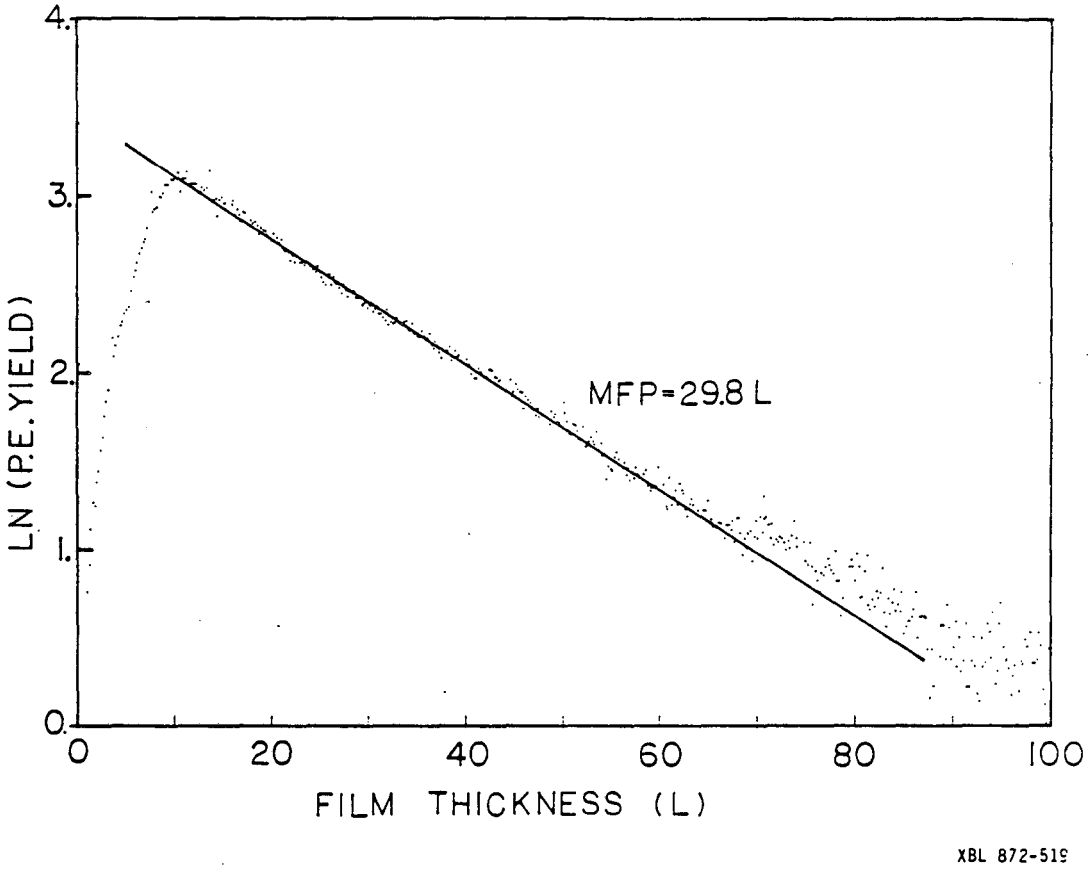

Figure 20. The same data as Figure 18 for anisaldehyde/Ag plotted as ln(photoyield) vs. film thickness. The slope of the falling portion of the curve can be interpreted as the mean free path (MFP) of the electron in the film.

radiation and ϕ. Photons at 266 nm (4.66 eV) are only 0.2 eV above ϕ for bare Ag. The $\Delta\phi$ upon anisaldehyde adsorption may as small as -0.28 eV as suggested by the analysis here. Even if a more typical value of -1.5 eV is assumed, the electrons are emitted at relatively low energy (< 2 eV). The actual energy spread of such photoemitted electrons can be obtained from some early work on energy resolved Ag photoemission,[115] where it was shown that when low energy photons were used (a few eV above ϕ) the electron energy distribution contained significant contributions from electrons at all energies between zero and ($h\nu$ - ϕ) due to production of secondary electrons by scattering in the metal. Therefore, the photoelectrons produced in this experiment will be at very low energies energies and a MFP of several molecular layers is quite reasonable.

Coverage dependent photoyield results for pyridine and cyclohexane are shown in Figure 21. The scaling factors allow these curves to be compared to anisaldehyde, indicating that cyclohexane causes a smaller decrease in ϕ while pyridine a much larger one. The functional form of the curve for cyclohexane looks much like that for anisaldehyde: it peaks at 12 L and is attenuated with a MFP of 28.4 L. The rising portion of this curve can also be fit with eqn. 33 to the Topping model. Assuming a polarizability of 10 $Å^3$, and a monolayer coverage of $3x10^{14}$ $/cm^2$, a dipole moment of 0.32 D is obtained corresponding to a $\Delta\phi$ of -0.12 eV at a full monolayer of coverage.

The yield vs. film thickness curve for pyridine (Figure 21) appears quite different than either anisaldehyde or cyclohexane, rising to it's maximum in only 3.8 L, and then decaying in an

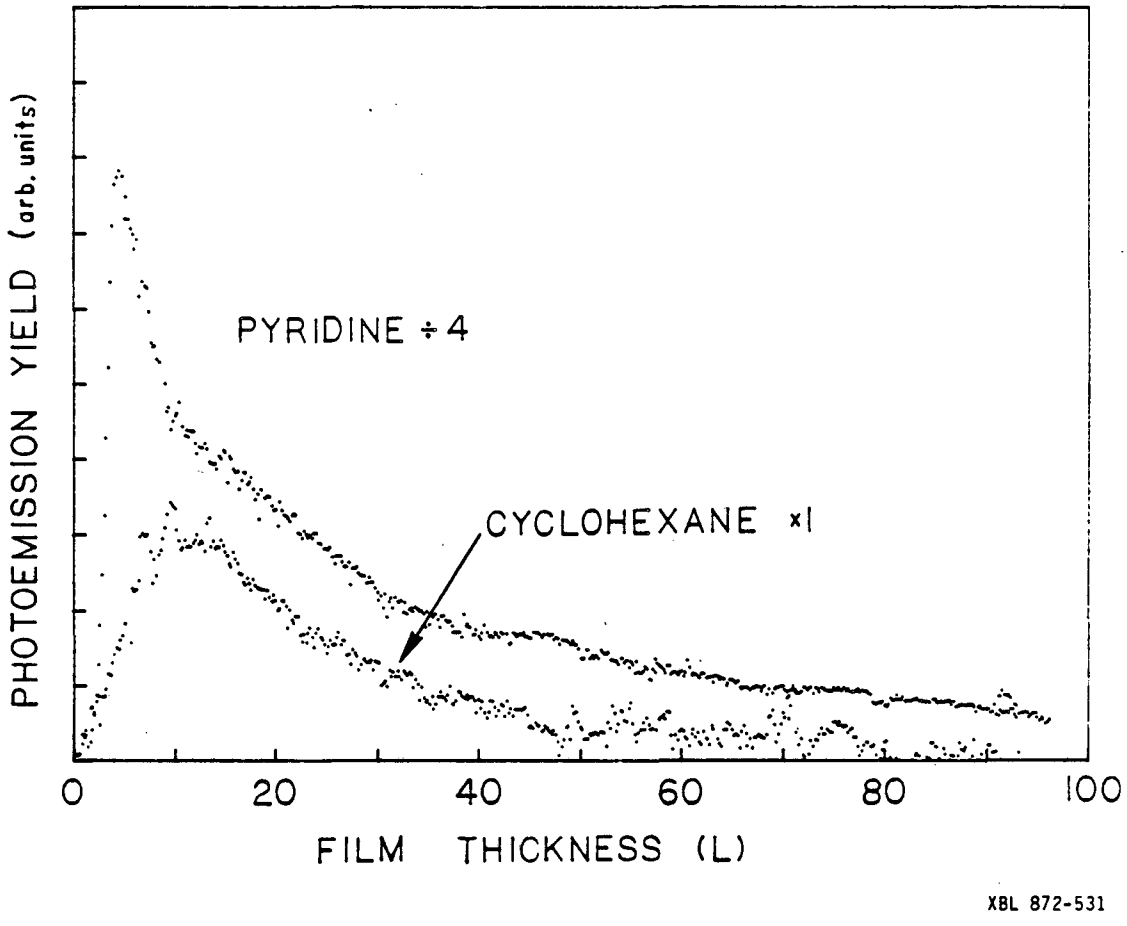

Figure 21. Photoemission yield data for pyridine and cyclohexane on Ag. The scaling factors are relative to Figure 18 for anisaldehyde.

obviously non-exponential fashion. In fact, it's can be broken into three distinct segments, each of which is approximately exponential. Between 3.8 and 8 L of coverage it falls with a 1/slope value of 9.5 L, between 8 and 30 L it becomes shallower at 28.7 L, and beyond that even more shallow with a value of 50.8 L.

More insight into this behavior can be obtained by monitoring the photoyield during thermal desorption of a thick (≈90 L) film. As Figures 19 and 21 show, photoyield measurements are extremely sensitive to the initial monolayer adsorbed, a fact which this technique exploits. An advantage over normal mass selected detection of the desorbates is that there is no interference with desorption from other parts of the cooled crystal manipulator - only changes on the crystal surface itself are detected.

Figure 22 shows such curves for each of the three molecules considered here. Cyclohexane appears to be readily interpretable: the initial rise at 150 K corresponds to desorption of multilayers, thereby causing the photoyield to rise to it's maximum value (the smallest value of ϕ occurs at one adsorbed monolayer). The next decrease in signal at 188 K is due to the desorption of that monolayer, indicating, as is often the case, that the first monolayer is more tightly adsorbed. The thermal desorption curve for anisaldehyde also shows similar multi- and monolayer desorption features as observed for cyclohexane, but occurring closer together at 205 K and 213 K, indicating a smaller difference in adsorption energy between the first monolayer and successive layers. The fact that the curve does not return to 'zero', may be interpreted as evidence for incomplete desorption or the prescence of decomposition

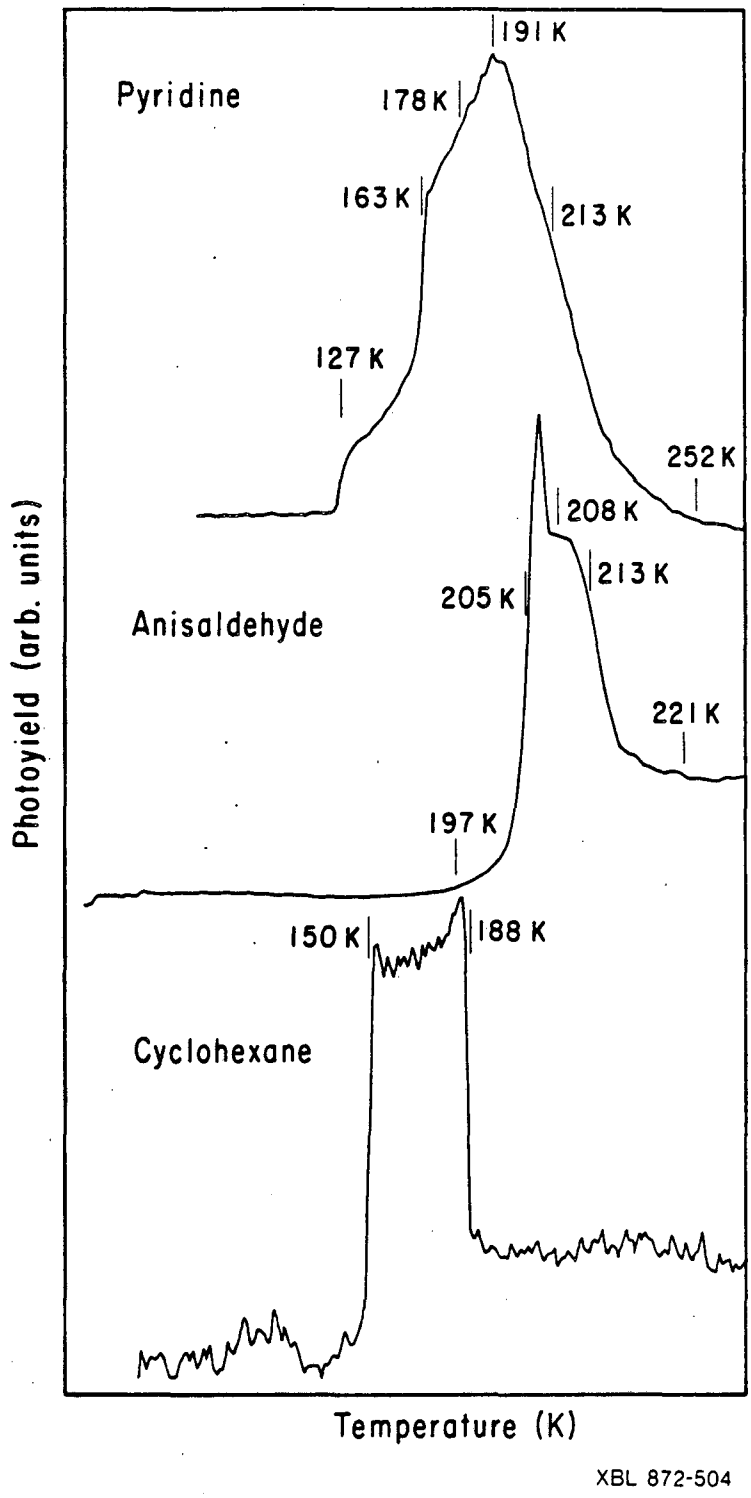

Figure 22. Photoyield thermal desorption spectra for each of the three molecules studied. The temperature axis is slightly different for each run. The heating rate was approximately 0.3°/s.

products on the surface. This may also account for the sharp peak observed right after the physisorbed layer desorbs.

Finally, the complicated spectrum obtained for the thermal desorption of pyridine will be considered. Pyridine on Ag(111) is known to undergo a compressional phase transition from a π-bonded species lying flat on the surface to a configuration bonded through it's nitrogen lone pair electrons with it's ring tilted at 55° to the surface near 0.5 monolayer.[116] The transition occurs at approximately one-half of a monolayer. The reported desorption temperature for the π-bonded species is 210 K, which compares well to the highest temperature desorption feature observed for pyridine in Figure 22 (213 K). Assigning the edge at 163 K to multilayer desorption, suggests that between 163 K and 191 K the N-bonded molecules are transforming to the lower coverage π-bonded phase.

The existence of a phase transition is consistent with the thickness vs. yield plot (Figure 21) as well. The sharp increase between 0 and 3.8 L is now understood to be due to the sub-monolayer formation of the π-bonded molecule. The break in the curve at 8 L thus signals the completion of a full monolayer of tilted N-bonded pyridine. This 8 L value is also more consistent with the cyclohexane and anisaldehyde monolayer completion thicknesses (12 and 10 L respectively). The extra edge in the thermal desorption curve at 127 K is not understood, but may correspond to a change in the bulk film structure. A related feature may be the kink in the thickness dependent curve (Figure 21) at 30 L. The MFP after 8 L of coverage, the point of the first multilayer formation, is 28.7 L, very close to the MFP's observed for the other molecules. After the

kink at 30 L film thickness, the MFP is 50.8 L.

The problem with this interpretation of the yield vs. coverage results for pyridine is that the flat π-bonded species should then have the larger effect on the work function. This is contrary to what might initially be expected, since the tilted form will have a larger permanent dipole normal to the surface compared to the flat form, which has no formal permanent dipole along the surface normal. Likewise the dipole contribution due to surface polarization appears to also favor a more negative $\Delta\phi$ for the tilted molecule. The polarizability of pyridine is approximately twice as large along the ring plane as perpendicular to it.[117] Thus, the tilted species should have a polarization dipole about 2.3 times as large as the π-bonded form. An argument can be made for a larger work function shift for the π-bonded pyridine by postulating charge-transfer to the surface. Demuth et al.[116] report that this form is weakly chemisorbed, being bound by 2 kcal more than the tilted molecule. Direct evidence for charge-transfer has been seen in EELS studies for both configurations of pyridine.[118] The π-bonded form displayed a broader peak, again suggesting that it is more tightly bound to the surface.

Whether the charge-transfer alone could outweigh, or change the other two $\Delta\phi$ contributions is difficult to estimate. Basing quantitative arguments on gas phase parameters is rather dubious for adsorbed species, especially when charge-transfer is present. The measurements presented here combined with an independent means of $\Delta\phi$ determination could better evaluate the uncertainities surrounding the above model.

B. Time Dependence of Photoyield

The time dependent data for the anisaldehyde/Ag system was collected in a similar fashion as the 'prompt' emission experiments described above, the only difference being the addition of an electrical gating pulse to the collection grid simultaneous with the 266 nm YAG laser pulse. Instead of a 20 ns FWHM photoemission yield signal, reflecting the temporal shape of the laser pulse, the behavior shown in Figure 23 is observed. Curve a is for a sputtered, and annealed Ag(111) surface at 77 K, where the double arrow indicates the position of the laser pulse in time. The gating reduces the photoyield intensity coincident with the laser by approximately 10^3. The large deflections seen on either side of the laser pulse are noise generated by the rising and falling edges of the gating pulse. The decay signal of curve b in Figure 23 is seen after dosing 85 L of anisaldehyde on the surface. Although this 'delayed' emission signal is quite non-exponential it decays on the order of a few hundred nanoseconds.

This time dependent feature can also be followed as a function of film thickness. Figure 24 displays these results for both the 'prompt' and 'delayed' signals for anisaldehyde. The 'prompt' emission data excited with pulsed 266 nm light shows the same exponential attenuation with film thickness as was reported above using arc lamp excitation (see Figure 18). The 'delayed' emission appears to increase with film thickness with approximately the same slope (1/12.7 L) as the fall of the 'prompt' (1/16.4 L), suggesting that the 'prompt' and 'delayed' emissions might be related. In some of the data, a saturation in the increase of both of these signals is

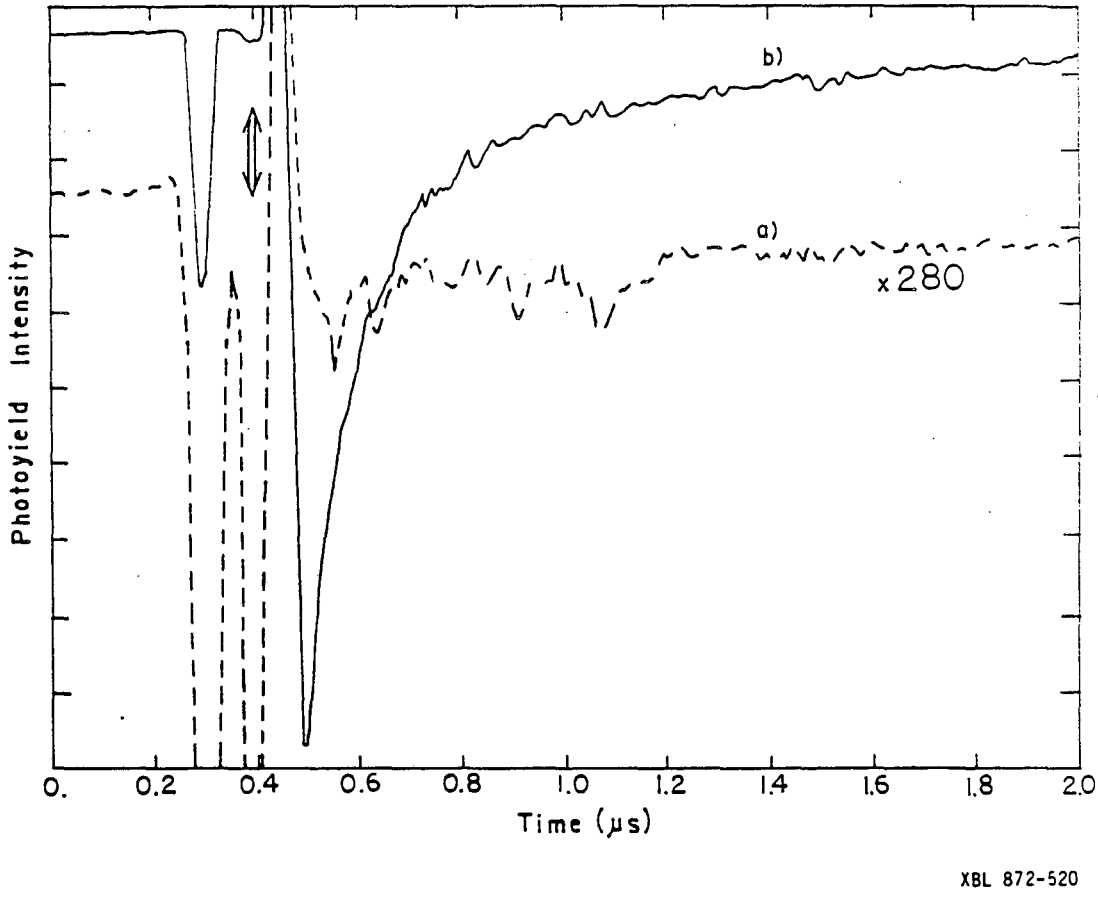

Figure 23. The time dependence observed for the 'delayed' signal. The double arrow shows the position of the laser pulse, surrounded by noise spikes from the gating pulse. a) Clean Ag at 90 K. b) After dosing 85 L of anisaldehyde.

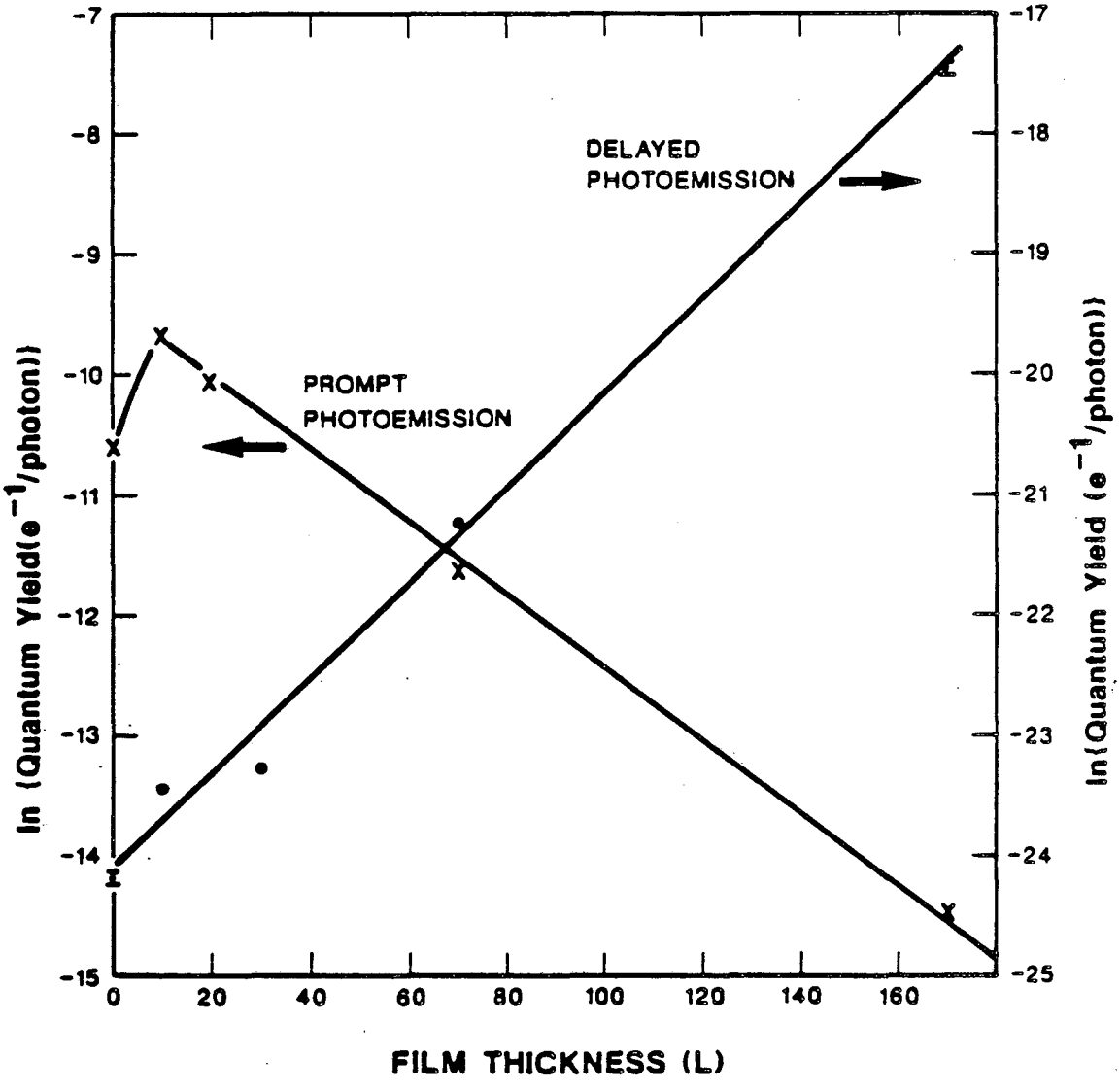

XBL 872-521

Figure 24. Comparision of the dependence of both the 'prompt' and 'delayed' signals on film thickness for anisaldehyde/Ag. The fall of the 'prompt' and rise of the 'delayed' have similar slopes. This data was collected using pulsed radiation at 266 nm. The 'prompt' curve can be compared with Figure 18, the same data obtained with arc-lamp excitation. Two points on the 'delayed' plot show estimated error bars.

seen for film thicknesses above ≈100 L.

The characteristic time decay shown in Figure 23 is usually observed only after deposition of at least ≈30 L of anisladehyde. Due to the limited range of thicknesses which were systematically investigated (0-100 L), it is difficult to determine if this curve changes shape with film thickness. For the existing data, however, it appears that the time-dependent features do not change appreciably with coverage.

Although these thickness dependent signals were normalized linearly to the exciting laser intensity, a rather anomalous, yet reproducible dependence is seen for the 'delayed' signal with respect to exciting laser intensity. Usually, a linear dependence is found (for example at 15L, and 85L), however, for data taken at film thicknesses of 35L the magnitude of the 'delayed' signal goes approximately with the square of the laser intensity. This is confusing since it is clear from the bare surface data already presented (Figure 16) that only linear photoemission is observed at these incident powers. A possible explanation for this observation will be discussed later in the context of a model.

Similar results to anisaldehyde for the 'delayed' signal have been obtained for benzaldehyde, pyrazine, and pyridine films. Both the quantum yield, and the approximate time dependence of the decay are duplicated. Contrasting behavior is displayed by napthalene, shown in Figure 25. The normal fall-off of the 'prompt' emission with film thickness without an accompanying increase in the 'delayed' emission proves that the presence of the 'delayed' emission signal is not simply due to an increase in the photoemission yield (i.e. work

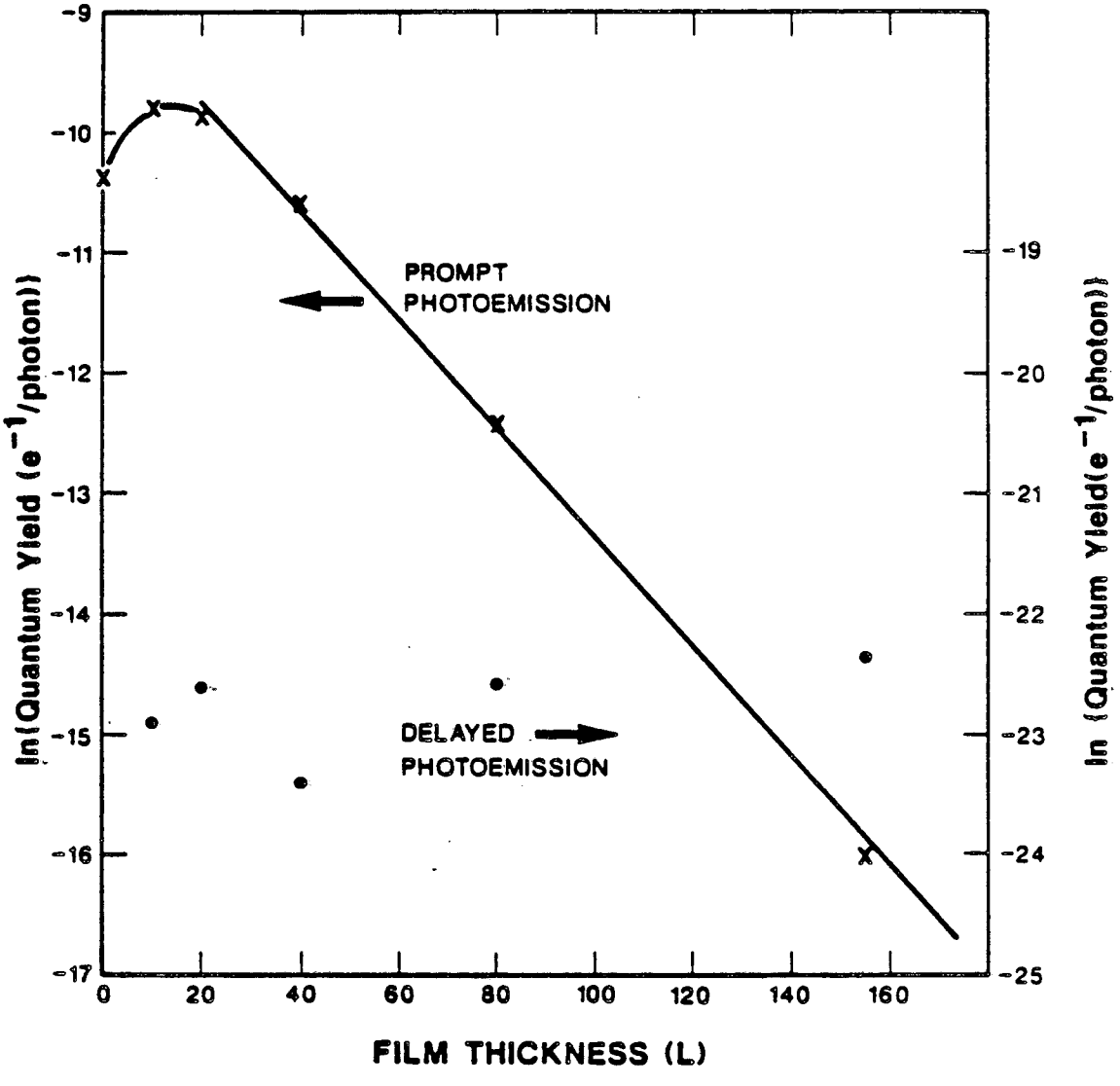

XBL 872-522

Figure 25. 'Prompt' and 'delayed' photoyield signals shown for napthalene/Ag. No increase in the 'delayed' signal was observed.

function lowering) upon adsorption. Another argument against this explanation is that the magnitude of the detected photoemission signal is approximately constant at each film thickness. Because of the limited dynamic range of the detector, the incident power was adjusted for each yield measurement. Similar to napthalene, cyclohexane films also showed little 'delayed' emission component.

The insensitivity of the 'delayed' emission to the identity of the molecule argues against the possibility of molecular photoemission or photoconductivity, especially with the broad range of photophysical parameters represented by the molecules studied here. As an example, anisaldehyde has a phosphorescence quantum yield of 32%,[119] whereas pyridine has extremely small quantum yields for both fluorescence and phosphorescence.[120] A more stringent test for a molecular process is the failure to observe this signal for molecular films deposited on cooled quartz substrates. In this instance, 'prompt' emission is reduced by at least a factor of 100 compared to Ag, shows no change with increasing film thickness, and also exhibits no 'delayed' component. A decrease in signal due to charging of the insulator was observed after several minutes of irradiation, and thus could be avoided if data were taken quickly. It is likely that this low level of signal represents a background determined by the sensitivity of the channeltron detector to stray 266 nm photons.

Space charge effects, defined here as a spreading of the photoemitted beam of electrons spatially, and thus also temporally, is rejected on the basis that any such effect would also be seen for the bare metal surface.

Although the system of the Ag surface in conjunction with the grid 2 cm away has an estimated capacitance of 0.5 pF, the relative increase in this figure upon insertion of a film into the capacitor of dielectric constant ϵ, and thickness th, can be shown to be (th)/(plate spacing), for large ϵ.[121] For the 100 Å films studied here the relative increase in the capacitance is 10^{-6}, which isn't consistent with the large increases seen in the electron decay signal after film deposition.

As a first step towards understanding the time dependence of the photoemission, classical trajectories of the photoemitted electron will be considered. A charge q placed a distance d from a grounded, perfectly reflecting conductor will be attracted to the metal surface via it's own induced surface charges. This well known problem[122] may be conveniently solved by the method of images where the conductor surface charge is replaced with a discrete 'imaginary' charge of -q, located the same distance d behind the conductor-vacuum interface. This is illustrated in Figure 26 a). The attractive potential felt by charge q is now given by Coulomb's law as $-q^2/4\pi\epsilon(2d)$. To model the experimental situation, this image potential is added to the constant potential due to the voltage applied to the collection grid. The total potential becomes:

$$V_T = \frac{-q^2}{4\pi\epsilon_0}\left[\frac{1}{2d}\right] + V_{ext} \qquad (32)$$

where ϵ_0 is the permittivity of vacuum. Molecular dosing of the surface can be represented as the addition of a dielectric slab on

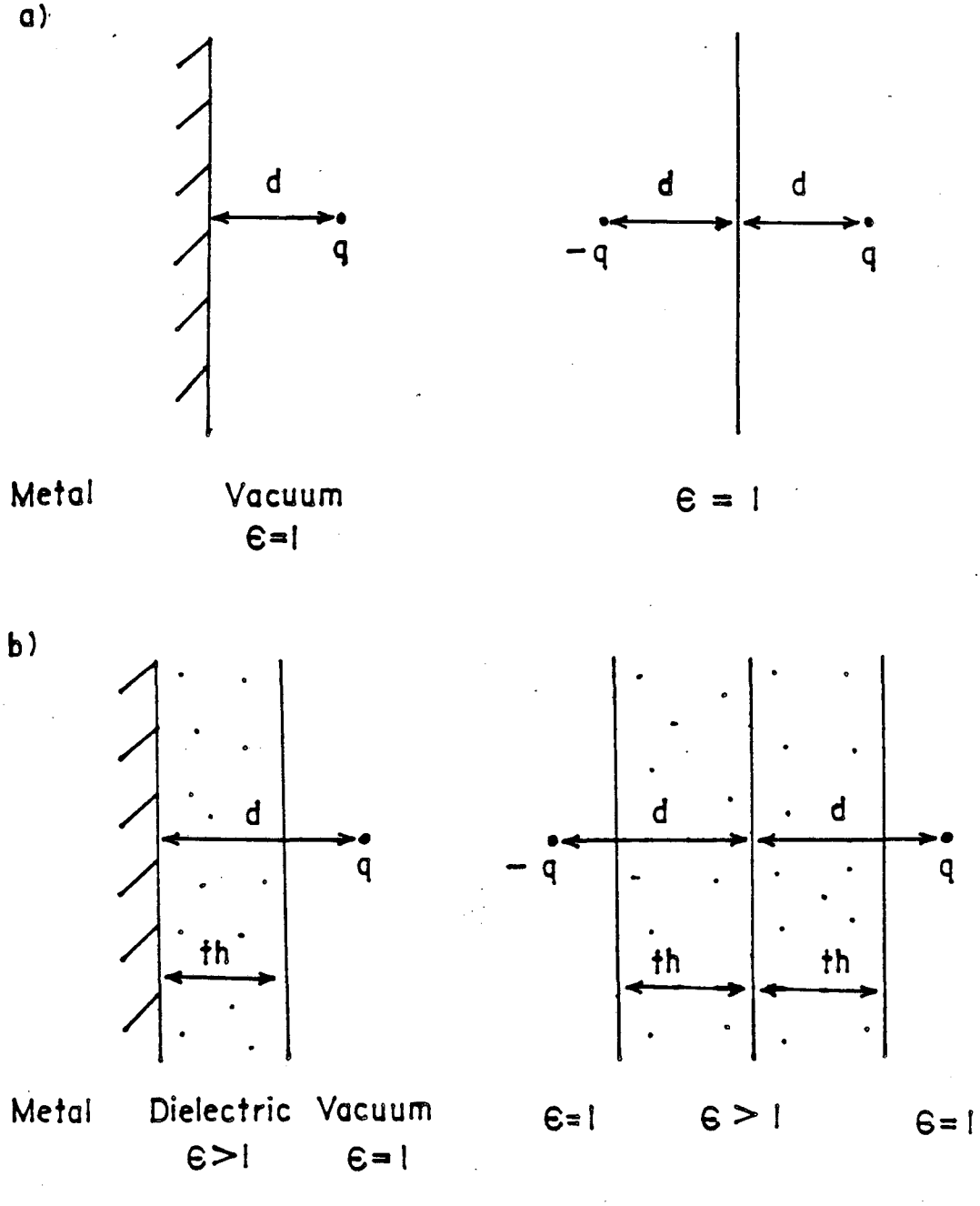

XBL 872-526

Figure 26. a) A charge q is located a distance d from a perfectly conducting metallic surface. To the right is the image solution of the problem formed by placing an equal but opposite charge, -q, the same distance d behind the surface. b) The charge is now a distance d away from a dielectric-coated surface. Also shown is the image solution which consists of reflecting the opposite of the charge, and the dielectric slab across the metal/dielectric interface.

top of the conductor. This is shown in Figure 26 b), along with the analogous image problem used to solve[123] for the potential. The potential is assumed to be the sum of the bare surface potential (eqn. (32)), and an additional term, ΔV, which represents the effect of the molecular dielectric layer. The 1/d potential can be expanded in a Taylor series and written as a integral. Trial solutions are assumed for ΔV such that they vanish for $d = 0$ and $d = \infty$.

$$(33) \qquad V_T = \frac{q^2}{4\pi\epsilon_0}\left[\int_0^\infty e^{-k(2d)}dk + \Delta V\right]$$

$$\Delta V = 2\int_0^\infty dk \begin{cases} A(k)\sinh(k\cdot d) & 0<z<t \\ B(k)e^{-k\cdot d} & t<z<\infty \end{cases}$$

where k is a dummy variable of integration. The coefficients A(k), B(k) are determined by the boundary conditions for D_n and E_t at the dielectric-vacuum interface. The full solution for the potential is:

$$(34) \qquad V_T = V_{ext} - \frac{q^2}{4\pi\epsilon_0}\left[\frac{1}{2d} - \Delta V\right]$$

$$\Delta V = 2(\epsilon - 1)\int_0^\infty e^{-k(2d-th)}\frac{\sinh(k\cdot th)}{\epsilon + \tanh(k\cdot th)}dk \qquad d>th$$

$$\Delta V = 2(\epsilon - 1)\int_0^\infty e^{-k\cdot d}\frac{\sinh(k\cdot d)}{\epsilon + \tanh(k\cdot th)}dk \qquad d<th$$

with th the thickness of the adsorbed layer of dielectric constant ϵ. The ΔV term disappears as it should for $\epsilon = 1.0$, leaving the usual expression for the image potential. In the limit $\epsilon \to \infty$ the dielectric layer becomes a conductor and therefore here also the potential should simplify to the bare surface result. In fact, for $\epsilon \to \infty$,

$V_T \rightarrow 1/2(d\text{-th})$, as expected. The solution for d > th can be evaluated since the integral converges as $k \rightarrow \infty$. The solution for d < th cannot be evaluated, however, since the integrand approaches a constant value, forcing the integral to diverge. As will be seen in the following discussion, the effect of this part of the potential can be estimated.

A plot of the total potential for d > th is shown in Figure 27 for various values of ϵ, and V_{ext}. The values used for V_{ext} correspond to the approximate field strengths used experimentally to either collect (V_{ext} = 20 V), or reject (V_{ext} = -20 V), the photoelectrons. The image effect is responsible for the constant rise in the potential over the first micron from the surface, while the steady fall in potential after this point is due to the applied grid voltage, V_{ext}. The curve obtained for ϵ = 20 would be indistinguishable on this plot from the potential for $\epsilon = \infty$, whose image potential, as discussed above, approaches a 1/2(d-th) dependence on distance.

Trajectories for electrons emitted from either the bare or dielectric-coated surface may now be calculated by integrating the energy balance equation:

$$\Delta t = \int_{d_1}^{d_2} \frac{1}{\sqrt{(2/m)(E - V_T(d))}}\, d(d) \tag{35}$$

where time (Δt) is given in terms of total energy (E) and the potential energy ($V_T(d)$). This equation was numerically integrated with the potential given by eqn. (34) using a 24^{th} order quadature

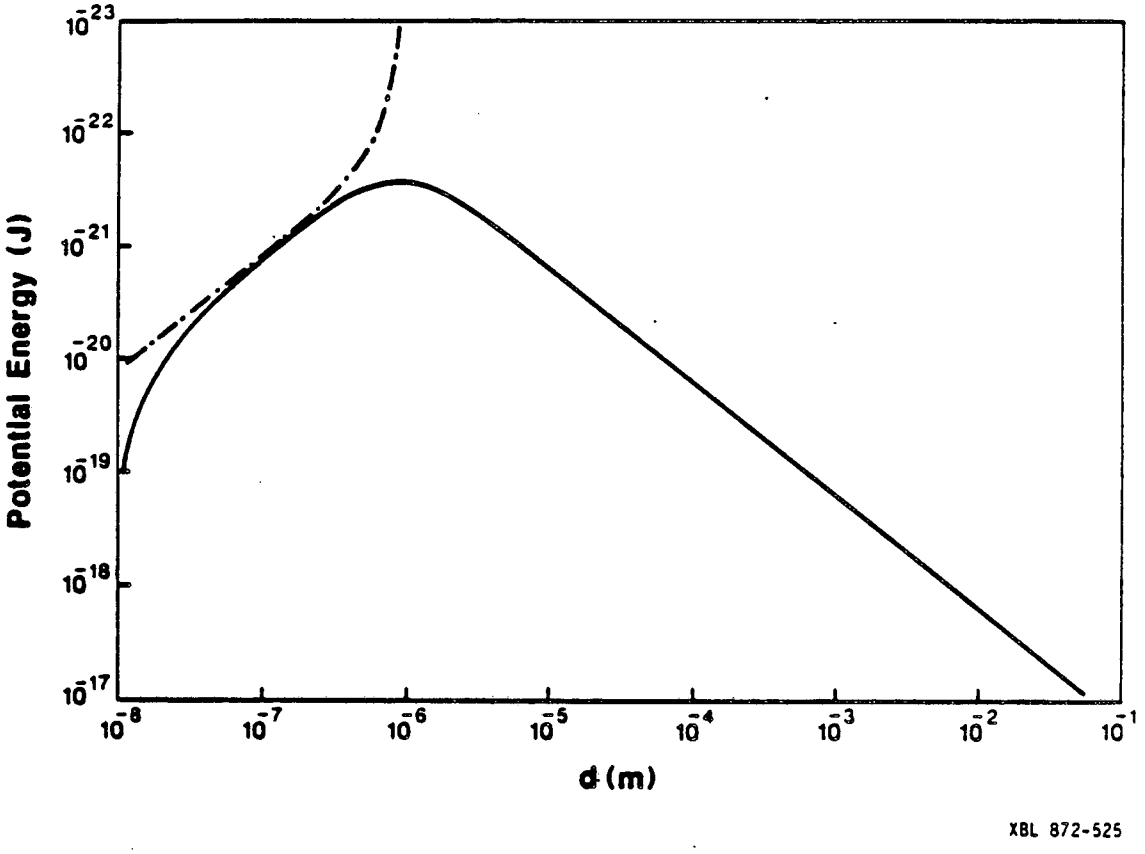

Figure 27. Potential energy vs. distance from a surface coated with 100 Å of dielectric. Curves are plotted starting at the dielectric-vacuum interface. V_{ext} = -20 V, ϵ = 1, -•-•-•-•. V_{ext} = +20 V, ϵ = 20, ————. The third curve is for V_{ext} = +20 V, ϵ = 1, and lies over the two lines already shown. It is ——— for $d > 10^{-7}$ and -•-•-•-• for $d < 10^{-7}$.

algorithm[124]. The Fortran program is listed in the Appendix. Below 10 Å the simple electrostatic solution for the image potential breaks down, so all trajectories are begun 10 Å from the surface.[46] An initial velocity, and a value for V_{ext} (±20 V) must also be specified.

Trajectories for a bare metal surface are shown in Figure 28. Photoelectrons are emitted with a spread of energies ranging from zero (just escaping the surface) to approximately the photon energy above the work function. To simulate this range, trajectories are plotted in Figure 28 for initial velocities just above the surface escape velocity to 0.5 eV above this velocity (the approximate energy a 266 nm photon lies above the Ag(111) work function). For the trajectory in which the initial velocity is less than 1 part in 10^6 above the escape velocity, the electron reaches the detector 2 cm away in 16.7 ns. The 0.5 eV electrons reach the detector in 6.67 ns, so the spread in collection times due to the time-of-flight effect of the electrons is about 10 ns. This effect will therefore not manifest itself in this experiment since the detection time resolution is 10 ns. A trajectory is also plotted in Figure 28 for an initial velocity just below the escape velocity. This electron turns around after about 0.1 ns when it is ≈1 μm from the surface.

In Figure 29, electron trajectories for a 100 Å thick layer of anisaldehyde on the Ag surface are shown. An ϵ=20 was used for the dielectric constant of the adsorbed film (ϵ=22.3 for liquid anisaldehyde[114]), and the trajectories were begun 10 Å from the film surface (110 Å from the metal surface). The results are not too different from the bare surface case. Those electrons just over the

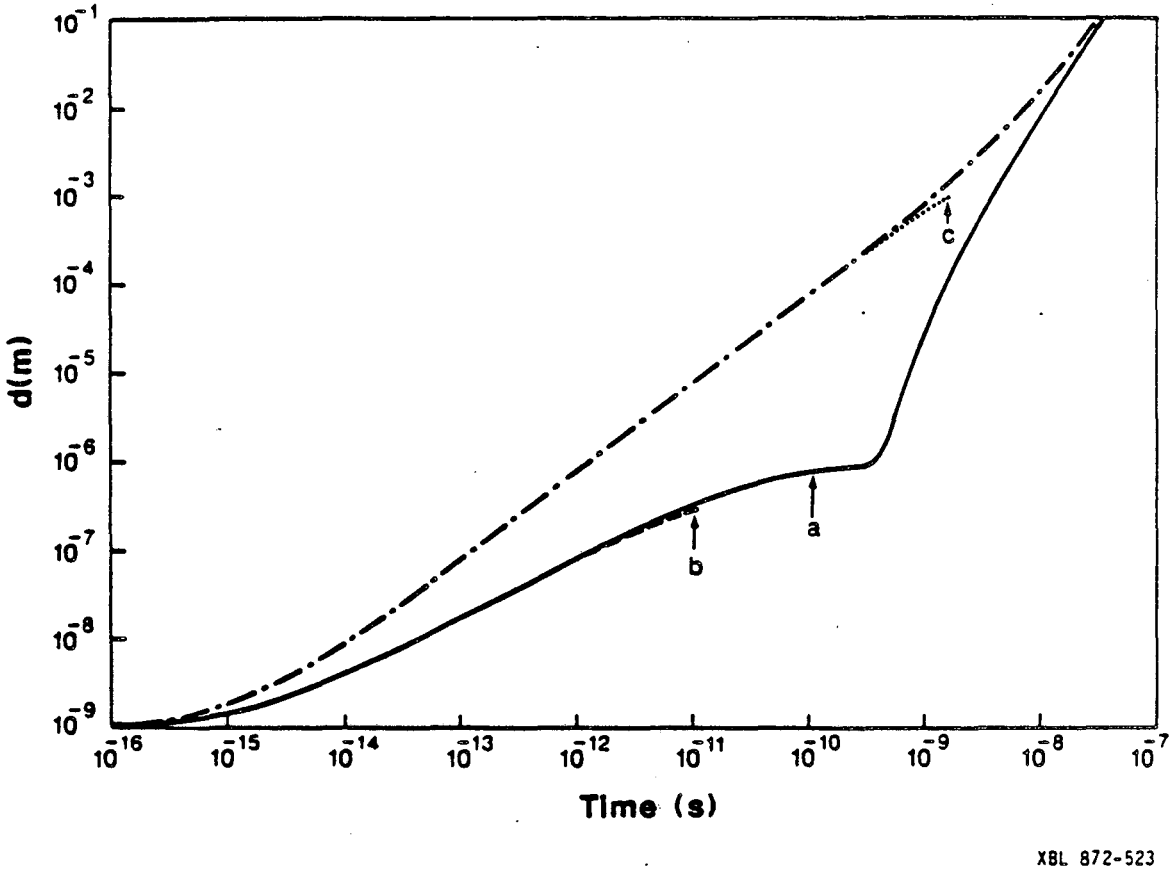

Figure 28. Trajectories for an electron escaping a bare metal surface. All runs were started with the electron 10 Å from the surface. With the initial velocity (v_0) just above the escape velocity (v_0 = 5.026348x10^5 m/s), V_{ext} = 20 V, the trajectory is ———. If the initial velocity is just below v_{esc} (v_0 = 5.026347 x10^5 m/s), the electron turns around at point a). If, in addition, a retarding field, V_{ext} = -20 V is used, the electron turns around at b). With 0.5 eV excess kinetic energy (v_0 = 9.219x10^5 m/s), V_{ext} = 20 V, the trajectory is —•—•—•—•. If V_{ext} = -20 V for this higher energy electron, the turnaround point is at c).

escape velocity arrive at the detector in 14.31 ns, a little slower than for the bare surface because of the difference in the magnitude of their respective escape velocities. The most energetic photoemitted electrons were assumed to have an energy of 2.5 eV, corresponding to a -2.0 eV shift in the work function due to the adsorbed layer. This value represents an approximate upper limit comparing to the shifts listed in Table 2 for similar molecules. Figure 29 shows that these high energy electrons need 8.15 ns to reach the detector. This time is ≈2 ns faster than the comparable bare surface value, and the resulting spread in electron collection times is only ≈6 ns. Although the transit time through the molecular layer was not included in this calculation as mentioned above, it is easy to see that the transit times are insignificant. Since the electron must have at least the calculated escape velocity of 4.81×10^5 m/s when it reaches a point 10 Å outside of the molecular film, and because it must be accelerating through the film to overcome the image potential of the metal itself, it must travel with at least this escape velocity through the film. So the maximum contribution to the overall collection time is simply (film thickness)/(escape velocity) or 23 fs. Therefore even for the case of a high dielectric constant molecular film with a large $\Delta\phi$, the time dependence of the photoemission yield signal is not predicted to change measurably with respect to molecular dosing.

As just demonstrated the magnitude of the escape velocity changes upon adsorption. The only place a comparison can be made between bare and dielectric coated surfaces is at 110 Å from the surface. Before adsorption, 1.50×10^5 m/s is required to escape,

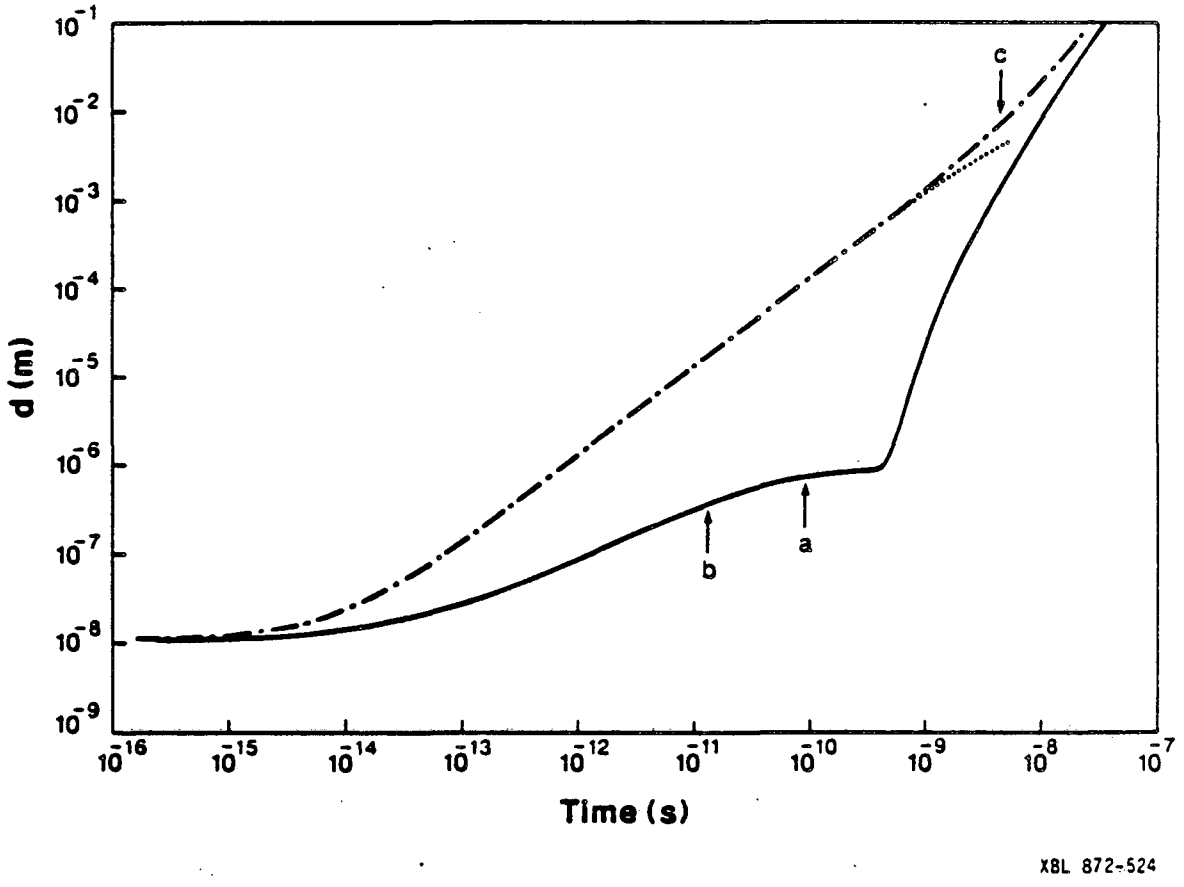

Figure 29. Similar trajectories as in figure 28, but for an electron escaping a surface coated with 100 Å of dielectric (ϵ = 20). All runs were started with the electron 10 Å from the dielectric-vacuum interface. With the initial velocity (v_0) just above the escape velocity (v_0 = 4.810913x10^5 m/s), V_{ext} = 20 V, the trajectory is ———. If the initial velocity is just below v_{esc} (v_0 = 4.810912 x10^5 m/s), the electron turns around at point a). If, in addition, a retarding field, V_{ext} = -20 V is used the electron turns around at b). With 2.5 eV excess kinetic energy (v_0 = 1.41878x10^6 m/s), V_{ext} = 20 V, the trajectory is —•—•—•—•. If V_{ext} = -20 V for this higher energy electron, the turnaround point is at c).

compared to 4.81×10^5 m/s after dosing. This implies that different populations of electrons are being detected in the two cases, i.e. after dosing the threshold for detection has seemingly moved up in energy by the difference in kinetic energy represented by these two escape velocities, or ≈0.6 eV. Experimentally, of course, this would mean a decrease in the photoyield even if there were no change at all in the work function accompanying adsorption. To verify this claim, the escape velocities should be compared at the surface, not the film-vacuum interface. This would require a solution to the image potential which can be evaluated within the film.

Since transit times are calculated to be on the order of the time resolution of this experiment, and shown not to change dramatically after dosing, this is not the cause of the long tails observed in the 'delayed' signals. An alternative approach to explaining the 'delayed' signals is to postulate the existence of traps in the molecular film capable of capturing the photoemitted electrons, and further that the time dependence is simply a property of the trap itself. Electron traps in condensed films have been documented in part I of this chapter, and lifetimes very much longer than the few hundred nanoseconds observed here have certainly been observed.[39,45] The problem with such a hypothesis is that once released from the trap the electron must have enough kinetic energy (a velocity on the order of 10^5 m/s) to overcome the image potential and be detected - otherwise the trapped electrons will simply fall back into the surface. An electron which is trapped for hundreds of nanoseconds will certainly lose it's kinetic energy to the matrix. Complete energy transfer might be expected to take at most 10^3 matrix

vibrations to occur, but assuming a typical phonon frequency of 10^{12} s^{-1}, this suggests that an excited electron could survive at most only 1 ns while trapped in a condensed medium.

An improvement on the trapping model which overcomes this problem is the screened image potential. Consider the situation illustrated in Figure 30 where an electron is situated a distance d_x from the conductor surface and is also in the vicinity of another electron located d_1 from the surface, and a distance d_y parallel to the surface from the first electron. In addition to image forces for each of the two electrons, there will also exist an extra coulombic repulsion between the two electrons which has a component perpendicular to the surface, therefore acting to 'screen' the electron from the attractive force of it's own image. Referring to Figure 30, the total forces parallel (F_y), and perpendicular (F_x) to the surface can be written as:

$$F_x = \frac{q^2}{4\pi\epsilon_0}\left[\frac{-1}{4d_x^2} + \frac{d_x-d_1}{\left[d_y^2 + (d_x-d_1)^2\right]^{3/2}} - \frac{d_x+d_1}{\left[d_y^2 + (d_x+d_1)^2\right]^{3/2}}\right] + F_{ext}$$

(36)

$$F_y = \frac{q^2}{4\pi\epsilon_0}\left[\frac{d_y}{\left[d_y^2 + (d_x-d_1)^2\right]^{3/2}} - \frac{d_y}{\left[d_y^2 + (d_x+d_1)^2\right]^{3/2}}\right]$$

F_{ext} is due to the constant applied potential by the grid. These equations were used to calculate electron trajectories for a variety of values of d_x, d_y, and d_1. The equations of motion corresponding to these forces were integrated using a fourth order Runge-Kutta algorithm[125]. The Fortran program used is shown in the Appendix. Zero initial kinetic energy was given to the electron at (d_x, d_y) to

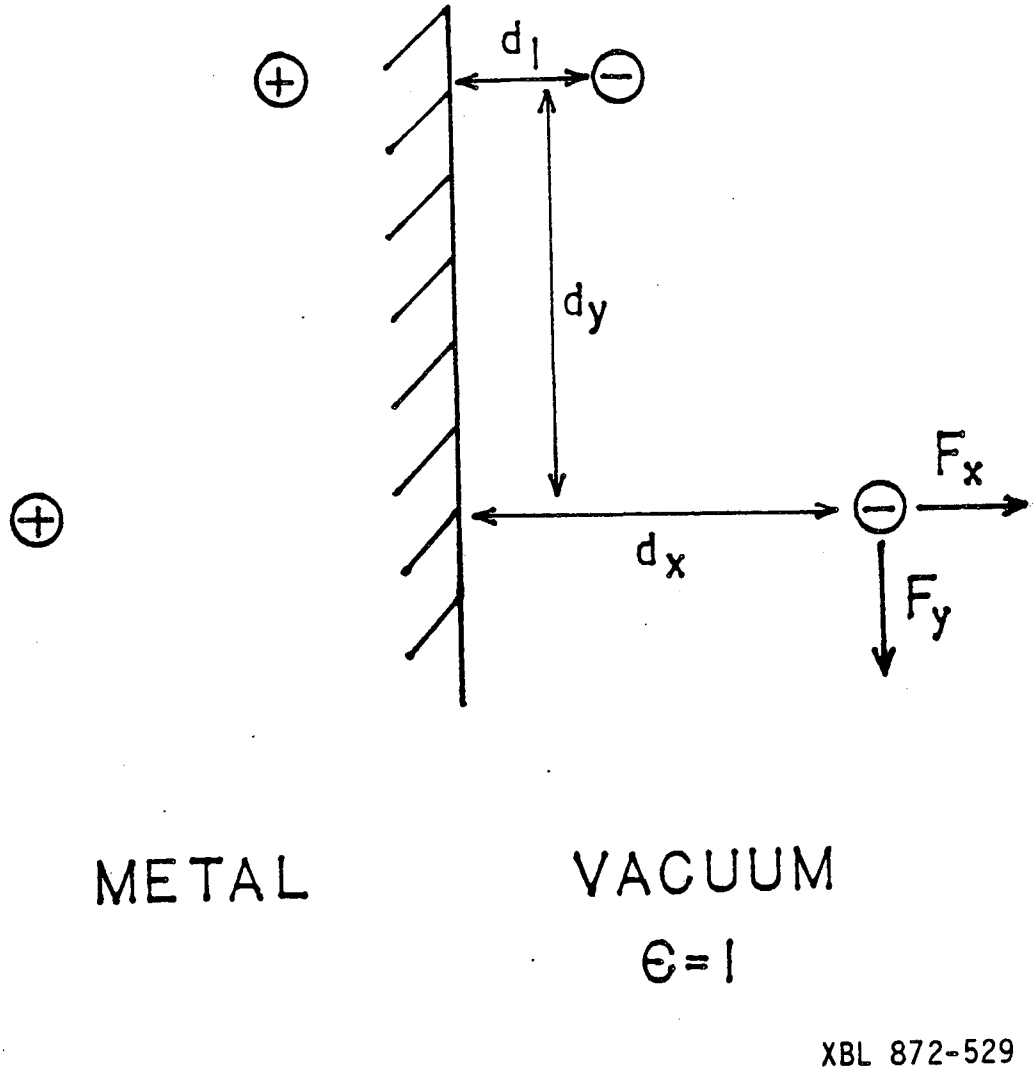

Figure 30. The screened image potential model. An electron a distance d_x from the surface interacts not only with it's own image, but also another electron located a distance d_1 from the surface, and it's image. There is also a constant force (F^1_{ext}) in the x direction from the constant grid voltage.

simulate an electron just after being released by a trap. The electron at $(d_1,0)$ was assumed to be trapped, and was therefore not allowed to move during the calculation. For each value of d_x and d_1, a critical value of d_y was found such that the corresponding trajectory escaped the surface to the detector. By varying these parameters the curves shown in Figure 31 were generated which delineate the region from which escaping electrons will eventually reach the detector. These curves were calculated for every 10 Å perpendicular to the surface. Since this problem is symmetric with respect to rotation about the x axis, sweeping these curves around this axis will produce a volume containing trajectories which successfully reach the detector. This volume was integrated numerically and when divided by the total film volume available to the photoemitted electrons (the beam spot size times the film thickness) represents the probability $P(d_1)$ of a trapped electron being subsequently detected as part of the 'delayed' signal.

Quantitative comparison of the screening model to experiment may now be done. The underlying assumption is that the 'delayed' electrons are the part of the original population of photoemitted electrons which have undergone trapping at special sites, i.e. there are two requirements for an electron to be observed as part of the 'delayed' signal: first, it must be trapped, and secondly it must be trapped in the vicinity of another trapped electron. If the film is divided into i layers, and exponential attenuation of the 'prompt' signal is assumed, then the number of electrons deposited in layer i is just the integral of the decaying exponential:

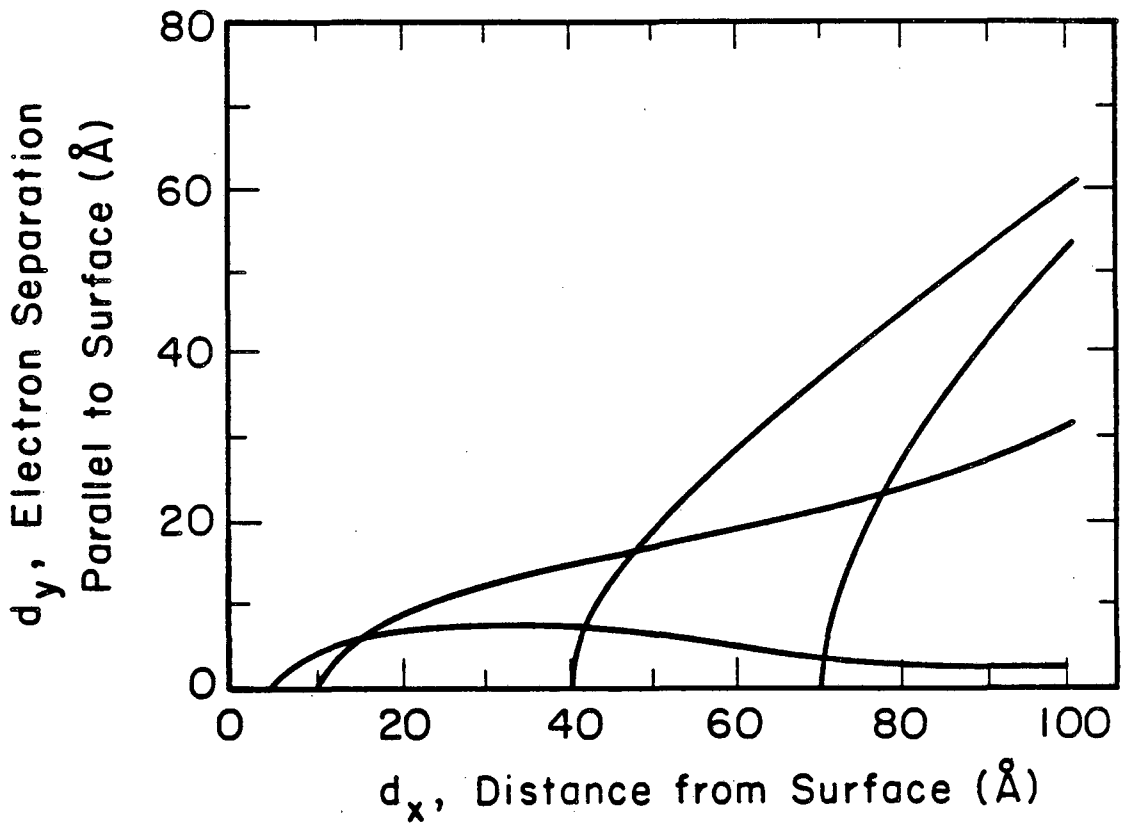

XBL 872-648

Figure 31. Critical values for d_y, the parallel separation of two electrons along a surface, plotted vs. the distance of the first electron from the surface, d_x, as defined by Figure 30 for the screened image potential model. The second electron sits at the x-intercept of each curve. All (d_x,d_y) points which fall below each curve represent starting points for electron trajectories which will sucessfully reach the detector. The electrons were given zero initial kinetic energy.

$$N_i = N_e \int_{x_i}^{x_{i+1}} e^{-x/MFP}\, dx \tag{37}$$

where N_e is the number of electrons emitted from the surface. Each of these electrons in the i^{th} layer has associated with it a probability $P(d_l=i)$ (as defined above) for successful trapping of another electron. The total probability that the electrons in layer i will screen a trapped electron such that it will contribute to the 'delayed' signal is $N_i P(i)$. The number of electrons in the 'delayed' signal due to the i^{th} layer (N_{ti}) is this total probability times the number of electrons in layers further from the surface than the i^{th} layer:

$$N_{ti} = P(i) \sum_{j \gtrless i} N_j \tag{38}$$

$$P(i) = \frac{N_i V_i}{\pi r_b^2 th}$$

where V_i is the volume determined from Figure 31, and r_b is the laser beam radius. After substituting in above, the following form is obtained for the number of 'delayed' electrons in layer i:

$$N_{ti} = \frac{V_i}{\pi r_b^2 th} N_e^2 I_i \sum_{j \gtrless i} I_j \tag{39}$$

$$I_k = \left[e^{-x_k/MFP} - e^{-x_{k+1}/MFP} \right]$$

The total 'delayed' signal predicted by this model is the sum of the individual contributions of each layer, N_{ti}. The number of electrons emitted from the surface, N_e, will simply be given by the photoemission quantum yield times the number of incident photons. Therefore, this model predicts that the magnitude of the 'delayed' signal varies with the square of the exciting light intensity. This behavior is observed experimentally, for layer thicknesses around 35 L. The prediction by this model for the dependence of the 'delayed' signal with film thickness is plotted in Figure 32. At thicknesses greater than ≈30 Å the 'delayed' signal approaches a square dependence with film thickness. Although experimentally an exponential increase with film thickness was observed, this model does predict a monotonically increasing 'delayed' yield with coverage.

A more significant problem is that the quantum yield predicted for the 'delayed' signal by this model is four orders of magnitude smaller than what is observed experimentally. However, the above calculation started the electrons just released from the trap with zero kinetic energy. A more realistic initial condition is to give these electrons the thermal energy of the matrix, which even at 90 K results in substantial electron velocities of $> 10^4$ m/s. If the trajectories are re-run allowing for $1/2k_BT$ of energy in each direction, quite different results are obtained. Now, an electron separated by as much as the beam radius (≈1 mm) from another trapped electron is able to escape the image potential of the surface. This picture predicts, then, that every electron which is trapped will contribute to the 'delayed' signal. This quantum yield of 'delayed'

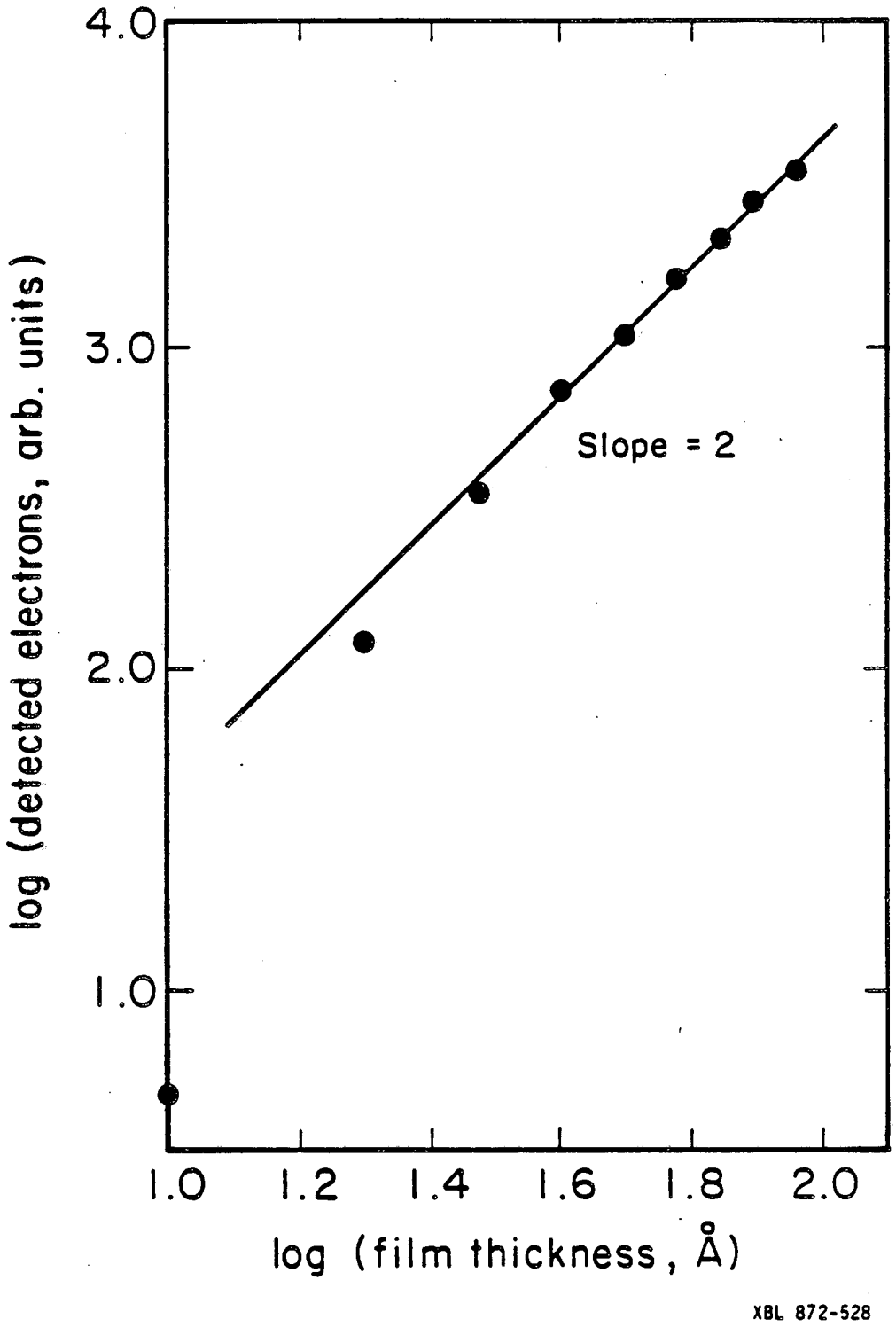

Figure 32. Predicted thickness dependence of the 'delayed' photoyield by the screened image potential model.

electrons to attenuated electrons is larger than the observed experimental value of 10^{-6}-10^{-4}, but there are refinements which could be added to the basic screening model above which would lower this yield. For example, instead of simply assuming that the electrons are in a vacuum, the effect of the dielectric constant of the film should cause a lowering of the calculated yield due to shielding of the trapped electrons from each other. The correct form of the image potential inside the film may also be important for correctly predicting the 'delayed' signal in this screening model.

Although greatly over-simplified, the screening model is useful. First of all, it predicts a square dependence of the 'delayed' signal with exciting intensity. Since such a dependence is only observed experimentally for a restricted thickness regime, more than one model may be required to explain the entire thickness range of the 'delayed' signal data. Furthermore, assuming that the observed signal decay times are simply a reflection of the trap lifetime, the screening model easily accounts for the quantum yields measured for the 'delayed' signal.

Another method of treating the delayed photoemission phenomenon is to consider the electron motion as a series of consecutive random hops between adjacent layers of the film. Trapping or attenuation can be introduced as a reduction in the probability of an electron continuing in an unimpeded path toward the detector. Since for a trajectory as in Figure 28 the electron velocity changes by only 1% over the first 100 Å, the electrons will be assumed to be travelling at a constant 5×10^{5} m/s (the escape velocity from the surface), and the image force will not be included explicitly in this model.

Two populations of electrons will be followed corresponding to those of the 'prompt' and 'delayed' signals. The 'prompt' population is generated at the surface and then hops layer by layer through the 20 layers chosen to represent the 100 Å thick film. The electrons successfully escaping from the last of the 20 layers reach the detector, and are recorded. The 'prompt' electrons hop from layer to layer (but only away from the surface) with a probability of 0.7 which corresponds to the experimentally measured MFP of 15 L. It is assumed that the remaining 'prompt' electrons (0.3 per layer) become the 'delayed' population, which propagates separately and isotropically with a 1/3 probability of moving either up or back a layer, or remaining in the same layer. This can be expressed mathematically as:

$$N_d = P_p N_p \tag{39}$$

$$N_d = P_d N_d + P_{p\to d} N_p$$

where N_p, N_d are the populations of the 'prompt' and 'delayed' signals respectively, and P_p, P_d are the matrices describing their hopping probability between layers. Likewise, $P_{p\to d}$ is the matrix for transfer from 'prompt' to 'delayed' populations. These probability matrices are:

$$P_p = \begin{bmatrix} P_{11} & P_{12} & \\ P_{21} & P_{22} & \ddots \end{bmatrix} = \begin{bmatrix} 0 & 0 & 0 & 0 & \\ 1.0 & 0 & 0 & 0 & \\ 0 & 0.7 & 0 & 0 & \\ 0 & 0 & 0.7 & 0 & \ddots \end{bmatrix} \tag{40a}$$

$$(40)b \qquad P_d = \begin{pmatrix} 1.0 & 1/3 & 0 & 0 & \\ 0 & 1/3 & 1/3 & 0 & \\ 0 & 1/3 & 1/3 & 1/3 & \\ 0 & 0 & 1/3 & 1/3. & \\ & & & & . \end{pmatrix} \qquad P_{p\to d} = \begin{pmatrix} 0 & 0 & 0 & \\ 0 & 1/3 & 0 & \\ 0 & 0 & 1/3. & \\ & & & . \end{pmatrix}$$

where the element P_{ij} describes transfer from the j^{th} layer to the i^{th} layer. During the time that the laser pulse is 'on' the 'prompt' population of layer 1 (the surface) was incremented by one before each cycle. This is halted to simulate the laser turning 'off', and additionally the $P_p(12)$ and $P_p(11)$ elements were switched so that after the laser is 'off' no electrons can escape from the surface.

These equations were followed numerically using the Fortran program listed in the Appendix. The total number of electrons (N_p+N_d) reaching the detector after the laser is turned 'off' should represent the experimentally observed 'delayed' signal. This signal, normalized to the total number of electrons emitted while the laser was on, is plotted versus the number of steps in Figure 33. This typical result was obtained with the laser on for 1000 steps before this plot was started. The exponential decay in signal from $\approx 10^{-2}$ to 10^{-10} occurs over 2000 steps. The total quantum yield of an actual experimental decay as in Figure 23 is $\approx 10^{-4}$ electrons/photoemitted electron. Assuming that only scattering of the photoemitted electrons is occurring, the time step length for this model may be estimated knowing the layer thickness and the electron velocity (5 Å, and 10^5 m/s respectively), resulting in 1 step equal to 10^{-15} s. The 1/e value of the signal in Figure 33 is 133 steps, so the decay time predicted by this random-walk model is 0.13 ps, failing to explain

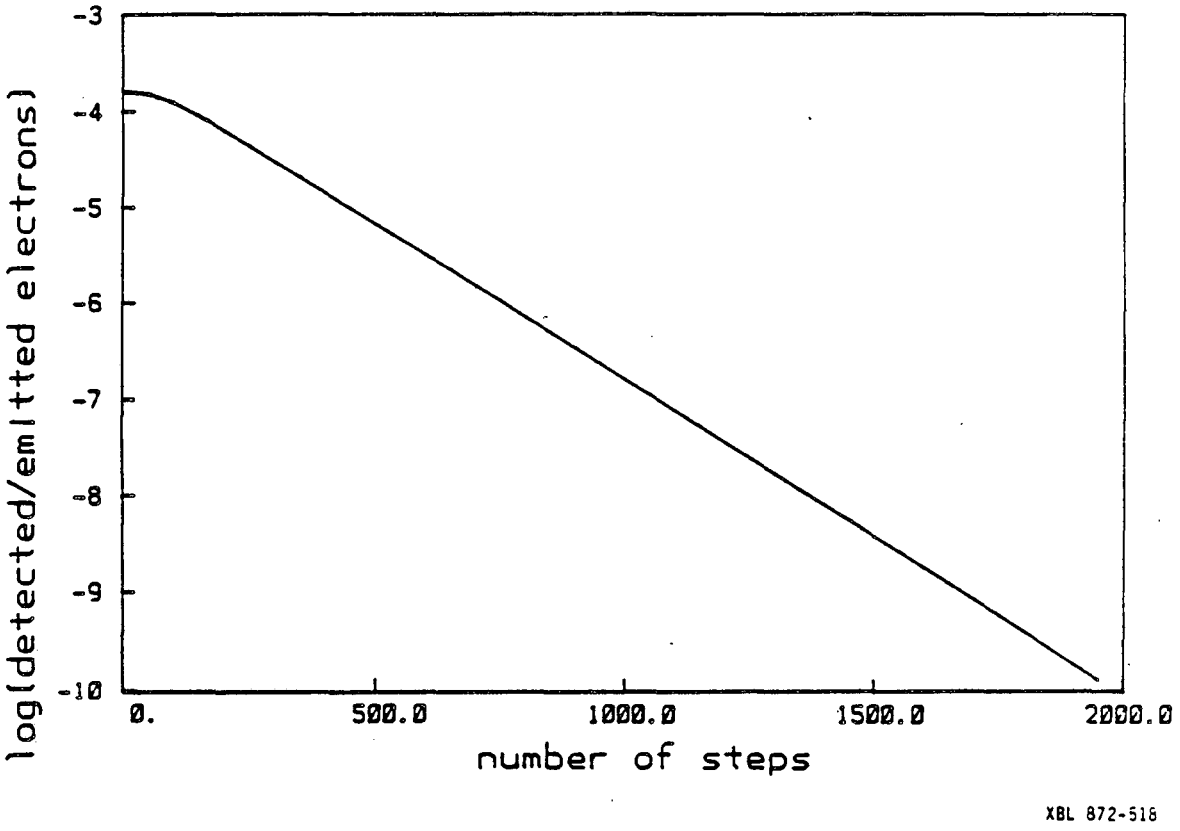

Figure 33. The predicted time dependence of the photoyield according to the random-walk model. The quantum yield of this simulated signal is 10^{-2} electrons/(emitted electron). The 1/e decay time of this curve is 0.1 ps if the nominal surface escape velocity of an electron is used. However, if a real diffusion constant is used to relate the step size to a time, then a decay time of 2 ns is obtained.

the value of ≈200 ns seen in experiments.

Diffusion will be quite sensitive to the properties of the film - an effect which was ignored in the model above. Had the diffusion model above been approached from the diffusion equation, the effect of the film would have been accounted for by proper choice of a diffusion coefficient, D. The step size of Figure 33 can be converted to a real time through D. The mobility, μ, of solid hexane, which should provide an order of magnitude estimate, is $\approx 10^{-2}$ cm^2/Vs at T = 150 K.[37] The Einstein relation ($D = \mu k_B T/e$) is used to obtain a diffusion constant of 7.8×10^{-5} cm^2/s. The solution to the diffusion equation is a Gaussian whose width can be used to characterize the distance diffused: $\sigma^2 = 2Dt$. Therefore using this expression with the 1/e value from Figure 33 of 133 steps, or 665 Å (5Å/step x 133 steps), t is found to be 2 ns. This is dramatically different from the 0.13 ps value obtained simply by using the escape velocity above.

This diffusion-controlled 'delayed' signal lifetime of 2 ns is approaching the kind of times observed in the experiment. The next refinement in this diffusion treatment is to realize that this problem is actually diffusion on a potential surface. The electrons are diffusing on the sum of the image potential and the applied grid potential. This is the one-dimensional analog of the problem solved by Onsager in 1938,[126] for the escape of an electron from the Coulomb well of an ion. Although Onsager treated only the steady-state solution, much attention has been given since then to the time-dependent behavior both theoretically,[127] and experimentally.[128] The Onsager problem differs from the one suggested here both because of

the dimensionality, and the boundary conditions - others have traditionally assumed a continuous dielectric as the electron moves away from the coulomb well. Here, however, absorbing boundary conditions are required on both sides; the inner one representing capture by the surface, and the outer one the film edge where diffusive motion ends. This problem has been solved for the steady-state by Charle and Wittig,[129] but as of yet no time-dependent solution exists. Very qualitatively, one expects diffusion on the image potential (the applied potential in this instance is negligible near the surface - see Figure 27) to decrease the detected yield and increase the time constant of the 'delayed' signal. The yield for the random-walk model of Figure 33 is 2×10^{-2} electrons/(emitted electron), larger than that observed experimentally. As mentioned before, the decay time of the curve is 2 ns, so the addition of longer decay-time components is also in the correct direction to agree with experiment. In lieu of a full treatment of the time-dependent solution, one can conclude at least that the trend predicted on the basis of diffusion out of the image potential of the surface is in agreement with experiment.

Two models have been examined to explain the time dependence of the 'delayed' signal - trapping and diffusion. For each model further absorption of light by the electron in the film might be expected. A trapped electron is known to absorb light in a broad band centered in the near IR; Figure 4 (part I) is an example of this. This second absorption was seen experimentally by Balakin and Yakovlev for electrons trapped in liquid hexane.[41] By applying an IR laser pulse at delay times after the initial ionization pulse, they

observed increases in the photocurrent corresponding to the timing of the second pulse. They were able to resolve this effect for delay times from 10 μs to 1 ms. Very similar behavior has been seen for electrons diffusing on their image potential near a metallic surface. These electrons can also absorb light in a bound to free transition as demonstrated by Scott in a recent report where he was able to time-resolve the electron's motion down the image potential by a pump-probe experiment.[130] He found much faster time-scales (74-330 ps depending on the excitation energy of the light) compared to the lifetimes of the bulk, trapped electrons reported by Balakin and Yakovlev. Interestingly, both of these experiments were performed on liquid hexane.

Evidence for subsequent absorption by the electrons in the film was looked for in this experiment. Typically pulses at the wavelengths accessible with the YAG laser (1.06 μm, 532 nm, and 355 nm), were overlapped temporally on the surface; however, delay times as long as 75 ns were also tried. No increase in the total photoyield was detected in any of these pump-probe attempts.

VI. Conclusion

The effect of adsorbates on the photoemission yield from Ag(111) has been studied for several different aromatic molecules and cyclohexane. Within the first monolayer of coverage all molecules lowered the work function of the surface. The $\Delta\phi$ shift was characterized by fitting to the Topping equation. Pyridine caused the largest effect, followed by anisladehyde with a $\Delta\phi$ = -.28 eV, and

then cyclohexane with $\Delta\phi$ = -.12 eV. The values appear to be smaller than those reported in the past employing more direct measures of the work function.

Multilayer adsorption causes an exponential decrease in the photoyield with respect to film thickness. The MFP determined from this data was on the order of several molecular layers for all three molecules. This relatively large value is consistent with the very low energy distribution of the photoelectrons (< 2 eV). The coverage dependence of the photoyield for pyridine is suggestive of the structural phase transition between flat and tilted forms of surface-bonded pyridine which has been reported previously. Results obtained by monitoring the photoyield during thermal desorption corroborate this phase transition.

Time-resolved measurements of the photoyield reveal a non-exponential tail extending for several hundreds of nanoseconds after the excitation pulse. The time-dependence is identical for the molecules which exhibited this behavior (napthalene and cyclohexane did not), and increases exponentially with film thickness. Two models are suggested to explain this phenomenon, one involving trapping by the film, and another diffusion of the electron on it's image potential in the film. Both models assume that the 'delayed' electrons are generated by attenuation of the 'prompt' population by the film. These two models appear to predict, at least qualitatively, the long time scales involved and the observed yield, but further experimental work is required to critically evaluate these models.

Chapter 2.

Monolayer Fluorescence of Tetracene on Si(111)

I. Introduction

Absorption and fluorescence of molecules adsorbed directly to semiconductor and metal surfaces are of interest because of the of the novel photophysical interactions present at such an interface. Work has also been motivated by applications such as the sensitization of semiconductor electrodes via molecular adsorption,[131] and photochemistry at or near surfaces used in 'laser-writing' metal films for circuit fabrication, and laser-induced chemical vapor deposition (CVD) semiconductor growth.[132]

The prohibitively small signals expected from fluorescence of molecular adsorbates stem from two causes. The first is the inherently small number of photons absorbed. Even for a molecule with an $\epsilon = 10^4$ /cm•M, only a few tenths of a percent of the incoming photons are absorbed. Compensating by increasing the incident power is limited at some point by desorption or damage to the adlayer due to substrate heating effects. The second reason for small fluorescence yields is the efficient non-radiative energy transfer to the substrate which exists for most conductive materials in the visible region of the spectrum. This pathway increases dramatically near the surface (as d^3), and can damp the effective fluorescence quantum yield by as much as 10^6. Non-radiative transfer has been experimentally characterized in this lab in the past for both metal[133], and semiconductor[134] surfaces, and has been found to obey a simple classical theory[135] in most cases.

Because of this difficulty in probing excited states of adsorbates, few studies have been done. Avouris and co-workers have

successfully used electron energy loss spectroscopy (EELS) to study the excited states of a variety of aromatic molecules as well as CO and Xe on Ag, Cu and Ni substrates.[136] Experiments have also been performed in this lab by Robota et al.[137] employing scanning ellipsometry to obtain absorption spectra for molecules on Ni(111). In a recent report, Dietsche et al.[138] have obtained absorption spectra of tetracene on Ag films using a novel technique to detect the phonons generated in a Ag film due to the relaxation of adsorbed, optically excited tetracene molecules. The phonons could be sensitively detected by superconducting tunnel junctions in contact with the substrate on which the Ag film was deposited. They record a vibrationally resolved absorption spectrum for the $S_0 \rightarrow S_1$ transition of tetracene even for coverages as low as 0.3 monolayers. Their Ag films were not kept under vacuum after preparation, so it is not clear that these results are actually for tetracene directly adsorbed to Ag. Dietsche et al. speculate that a layer of water may exist on the film.

The work reported here represents the first account of detected fluorescence for a molecular monolayer adsorbed on a non-insulating surface. The system studied is tetracene/Si(111), and the fluorescence was laser excited and detected using conventional photon counting techniques. According to the theory for energy-transfer mentioned above, the first monolayer will have a competing non-radiative energy transfer rate into the Si surface approximately 2000 times it's radiative emission rate.[139] Changes in the fluorescence spectrum of the adsorbed tetracene as a function of coverage were also observed and are related to monomer aggregation. Finally, new

features, believed to be vibrational structure, were observed in the fluorescence spectra for tetracene when adsorbed on Xe spacer layers above the Si surface.

II. Experimental Procedure

The experiments were performed in a standard UHV chamber operating at pressures in the low 10^{-10} torr regime. A schematic drawing of the chamber is shown in Figure 34. A liquid helium cold tip allowed the crystal to be cooled to 30 K, by flowing liquid He. Liquid N_2 could also be employed as a coolant, but unavoidable vibrations caused by the expanding liquid/gas degraded the signal. For this reason all data reported here was obtained using liquid helium cooling.

The fluorescence was excited continuously with several different lines of a Coherent Innova-100 Ar^+-ion laser. Tetracene in solution absorbs into it's S_1 state between 375 and 490 nm with an ϵ of 10^4 /cm•M at the maximum of the various vibrational peaks observed.[140] For thick amorphous films, this is seen to shift and broaden to about 400-540 nm.[141] Similar spectra were obtained here using either the 488.0 nm or 476.5 nm line of the laser. Estimated typical intensities of 100 W/cm^2 were obtained by loosely focussing the laser onto the crystal. At incident intensities approximately five times this value, some evidence of damage to the molecular layer was observed. The input radiation was passed through a dielectric bandpass filter to eliminate plasma line emission and was then p-polarized.

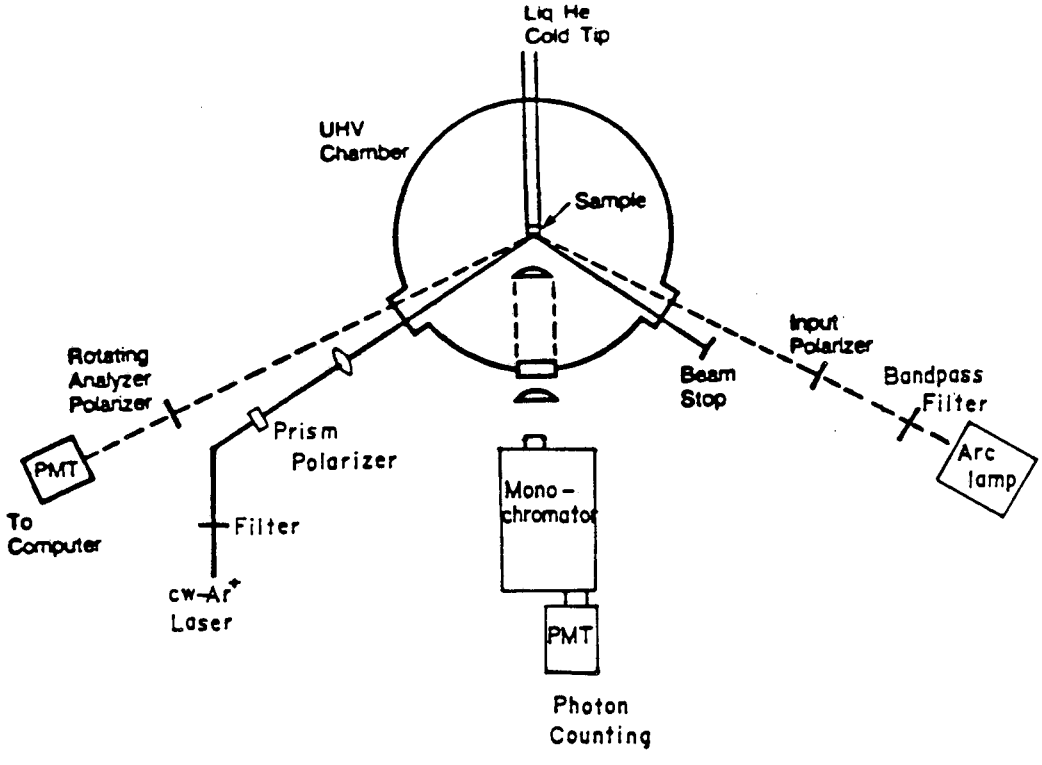

Figure 34. Schematic of the experimental set-up used for fluorescence detection of tetracene/Si(111).

The fluorescence was collected with a f/1 quartz lens and focussed into a Spex doublemate monochromator with a resolution of 0.5 nm. The output of the EMI 6256 phototube was amplified x10 by a Kiethley wideband amplifier, fed through an EG and G TD101/N discriminator, and was then counted and stored by computer.

Polished Si(111) wafers were 500 μm thick, and 10 ohm-cm resistivity. Before installing in the chamber, they were etched according to a procedure determined ellipsometrically by Aspnes and Studna[142] to result in sharp interfaces. The process consisted of successive etches in bromine/methanol, HF/methanol, and $NH_4OH/H_2O_2/H_2O$ dilute solutions. Before each experiment the Si was also Ar^+-ion sputtered for one hour, followed by a 10 minute anneal at 850°C.

The tetracene was purchased from Aldrich and a GC/MS analysis revealed ≈99% purity. It was introduced into the chamber through a leak valve connected to an inlet line pumped to 10^{-7} torr and heated to 195°C with heating tapes. This was necessary to overcome the small vapor pressure of tetracene. Since the dosing into the chamber is essentially a distillation, the tetracene improved in purity the longer a single sample was used. Indeed, initial doses with a new sample were never used in an experiment until only those peaks attributed to tetracene could be observed in the chamber quadrupole mass analyzer.

Coverage was monitored by a rotating analyzer ellipsometer, which has been discussed previously.[143] The 365 nm emission line of a 100 W Hg arc-lamp was isolated with a dielectric bandpass filter, polarized, reflected off the crystal, and finally passed through the

rotating polarizer to a phototube. Coverages could be calibrated by comparing a broad range of experimentally determined tetracene/Si optical constants with those generated by a computer simulation based on an successive arbitrary choices for the optical constants of the overlayer. Once the correct overlayer optical constants are thus found, the ellipsometer output during dosing can be directly related to the molecular film thickness. Although this system has provided precision to 0.1 monolayer in the past, slow but steady drifts in the ellipsometer constants during these experiments limited the accuracy to ≈20%. The drift was in the direction of increasing coverage, and thus may have reflected actual dosing due to residual amounts of tetracene generated through the heating of the leak valve of the chamber. For this reason all drifts were interpreted as 'real' coverage increases and therefore it is felt that the tetracene coverages quoted below represent upper bounds to the actual amount present on the crystal surface.

III. Results and Discussion

Figure 35 summarizes the experimental results for the fluorescence of tetracene/Si(111) excited at 488 nm for coverages of 0. to 4.9 monolayers. 6.65 Å was used as the monolayer thickness determined by approximating the tetracene as a cube and using the reported density of crystalline tetracene of 1.29 g/cm^3.[144] Assuming that, at least for the initial monolayer, tetracene lies flat on the surface[145], this value of 6.65 Å overestimates the monolayer thickness since the value for the interplanar spacing of crystalline

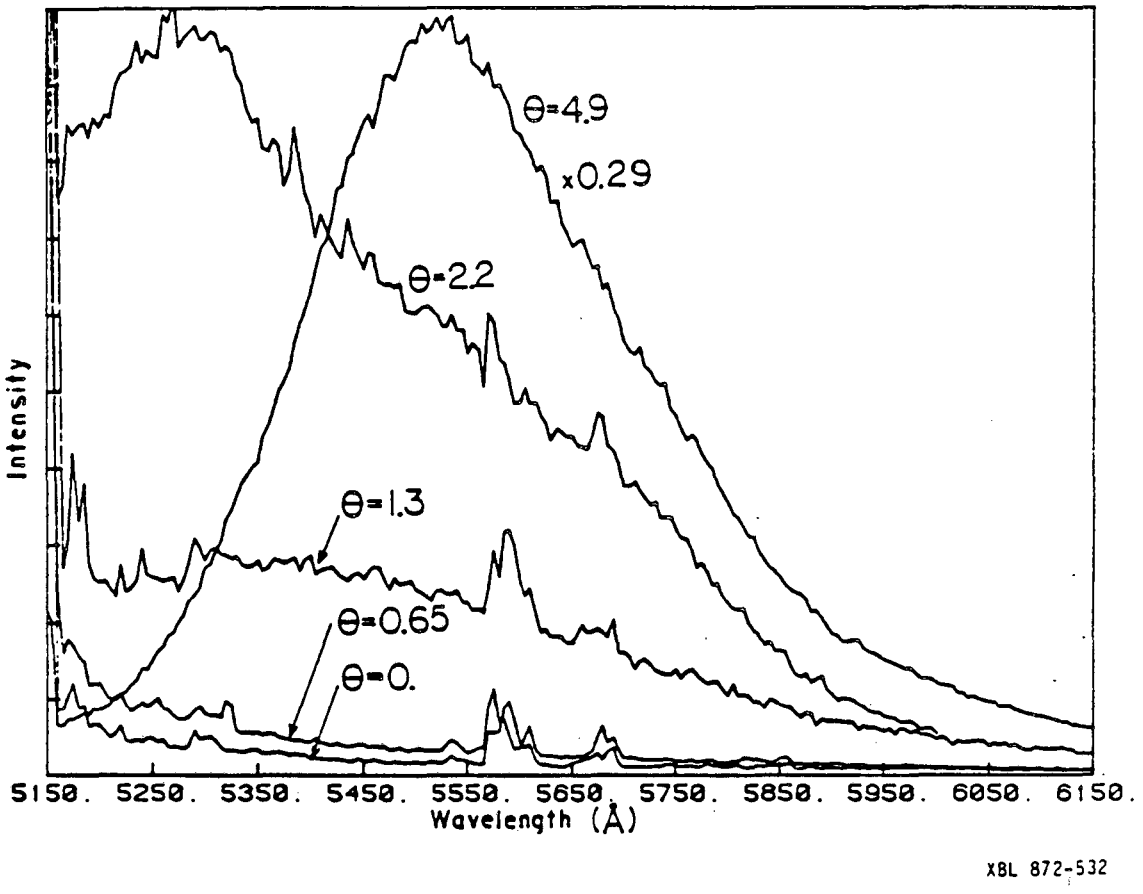

Figure 35. Fluorescence of tetracene adsorbed on Si(111) at 30 K and excited at 488 nm. See text for discussion. The sharp reproducible features are spectrometer grating ghosts.

tetracene is known to be 3.83 Å.[146] The tetracene films studied here will probably be amorphous, however, as was shown by Eiermann et al.[145] via electron diffraction studies of tetracene deposited onto cooled carbon films. They concluded that some degree of short-range crystalline order was present and increased with increasing temperature, but that overall the tetracene was amorphous. Amorphous layers will not pack as tightly as the crystalline form, and thus the value of 6.65 Å taken for the tetracene layer thickness should represent a reasonable estimate.

The fluorescence spectra in Figure 35 are quite sensitive to coverage. For the lower coverage curves it is difficult to ascertain the maximum, but at $\theta = 2.2$ the peak occurs at 528.0 nm with a shoulder that appears to grow in to become the 551.5 nm peak at $\theta = 4.9$. Aggregation of tetracene and the effect on it's optical properties was first studied in 1967 by Katul and Zahlan.[147] They assigned the fluorescence observed at low concentration to a monomer and the peaks which grew in at higher concentration to a dimer. The features due to the latter were observed to the red of the monomer and resembled the crystal spectrum. In later work, Fournie et al.[148] reassigned this dimer feature to a larger aggregate they called a microcrystal, and also reported observation of a new peak, intermediate in energy, which they assigned to the dimer emission. They point out, however, that the so-called dimer feature has not been shown to be due to just two tetracene molecules. This question of assigning optical features to various sized aggregates, which are seen quite commonly for many aromatic molecules, is discussed by Martinaud.[149]

Returning to the Figure 35, the 551.5 nm peak seen for $\theta = 4.9$ shifts to approximately 560 nm at $\theta = 10$, which is in fair agreement with the microcrystal peak at 565 nm reported by Fournie et al..[148] The peak at 528.0 nm in the $\theta = 2.2$ spectrum is seen to red-shift with coverage until it disappears into the 551.5 nm peak. It is probably due to the dimer peak that Fournie et al. see at 539 nm, and may be shifted from their value somewhat by the interaction with the Si surface. Evidence of this has been seen in other experiments performed in this lab where it was found that the high energy peak for tetracene occurred between 538-546 nm on sapphire, and 516-526 nm on single-crystalline NaCl.

Preliminary data has been obtained for fluorescence of tetracene spaced away from the Si(111) surface by the deposition of a film of Xe atoms preceding the tetracene dose. Spectrum a) shown in Figure 36 was taken immediately after dosing $\theta = 0.25$ of tetracene on top of 25 Å of xenon. Spectrum b) was collected following a), and judging from the differences, tetracene was still being deposited. This time-lag in dosing after closing the leak valve has not been observed in the past for more volatile substances, and is presumably due to the difficulty in pumping such a low vapor pressure molecule. The other notable feature is the structure exhibited by this spectrum-unique for all the various surfaces on which tetracene fluorescence was studied in this lab (Si, sapphire and NaCl). The peaks in Figure 36 b) are fairly regular with a periodicity of $\approx$435 cm^{-1}. After the deposition of another dose of approximately 1 monolayer, spectrum c) was obtained, which shows a red-shifted peak as was seen previously, and a blurring of the regular features seen in b).

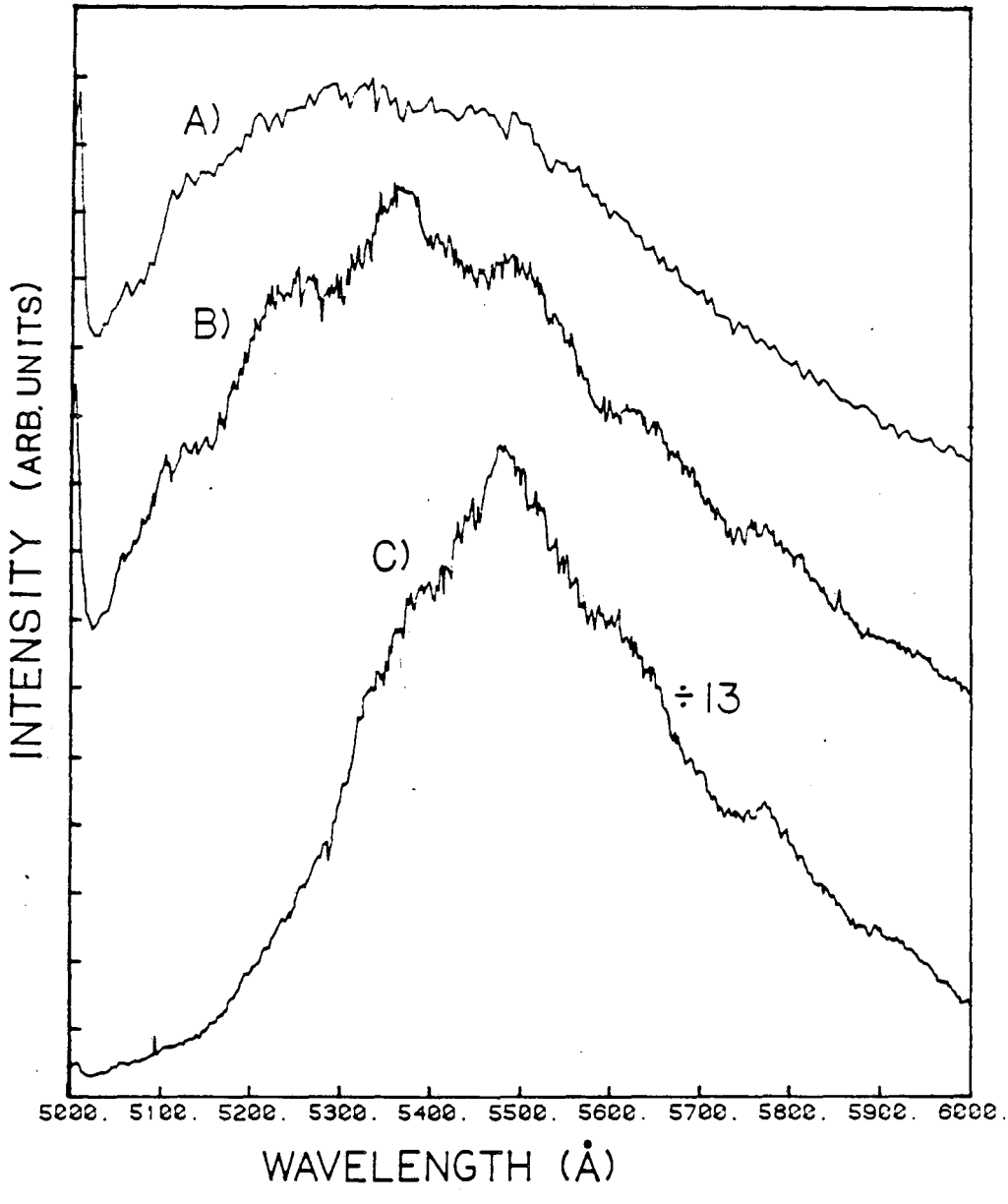

Figure 36. The fluorescence of tetracene spaced 25 Å from a Si(111) surface with Xe, excited at 476.5 nm. A): θ = 0.25 of tetracene, collected after dosing. B): Taken after scan A). C): After deposition of another monolayer. Note that the baselines are offset.

Assignment of these features is not obvious. Phonons in cryogenic rare gas matrices are reported to lie well below 100 cm^{-1}.[150] Sidman has assigned the fluorescence spectrum for tetracene substituted into a crystal of anthracene.[151] He finds a fundamental vibration at 321 cm^{-1} and another weaker one at 619 cm^{-1}. The data Amirav et al.[152] have collected for tetracene fluorescence in a seeded molecular beam agrees well with the work of Sidman, although in addition they find a weak fundamental vibration at 489 cm^{-1}. Both of these studies are for the isolated tetracene molecule, however, and the aggregated species could have perturbed vibrations. Evidence for this comes from fluorescence studies of tetracene films such as the work of Sakurai et al.[153] where structure was seen at 615 cm^{-1} in the crystal spectrum, and at 840 cm^{-1} for films deposited at -120°C. Katul and Zahlan[147] observe a second peak at 1270 cm^{-1} in the crystal fluorescence, in agreement with the 1300 cm^{-1} separation seen by Fournie et al..[148] In addition, however, Katul and Zahlan also see a 370 cm^{-1} peak in the spectrum they assigned to the dimer.

If the 435 cm^{-1} features observed here is indeed due to a vibration of a tetracene species, it is interesting to note that this structure was seen only for adsorption on Xe spacer layers. Assuming these features are associated only with the tetracene implies that they are obscured by inhomogeneous broadening for both sub-monolayer and multilayer coverages of adsorbed tetracene on Si, as well as the insulator surfaces of sapphire and NaCl.

IV. Conclusion

Fluorescence from a directly adsorbed molecular monolayer of tetracene on Si(111) has been detected. The competition with non-radiative energy transfer to the surface, and the inherently small signals expected from such monolayer amounts have traditionally made such measurements difficult. Changes in the fluorescence spectrum over the first 10 monolayers were seen and attributed to the creation of new fluorescent species due to aggregation of the tetracene monomers, as has been observed in other systems. Finally, preliminary evidence has been seen for vibrational structure in the tetracene fluorescence when adsorbed on a layer of Xe above the Si surface. This suggests that the fluorescence spectra for the directly adsorbed layers of tetracene investigated here are predominantly inhomogeneously broadened.

Chapter 3.

Photochemistry on Rough Metal Surfaces

I. Introduction

Increasing attention is currently being focussed on the possibility of observing photocatalyzed reactions on metal and semiconductor surfaces. While it has long been known that certain chemical reactions will proceed on irradiated semiconductor surfaces where the semiconductor is excited with bandgap radiation and transfers energy to the adsorbates, very little evidence exists for true photoinduced reactions on metal surfaces[154,155]. Recently, however, the possibility of dramatic increases in rates of photoinduced reactions of adsorbates on metal surfaces has been hypothesized[156] due to the large enhancement of many processes (Raman scattering, IR absorption, fluorescence, and second harmonic generation) on certain structured metal surfaces. We reported the first observation of an enhanced photoreaction rate for the fragmentation of a number of molecules on roughened silver substrates using near UV radiation[157]. Other reports of enhanced decomposition rates have subsequently appeared for the decomposition of rhodamine-6G on silver island films[158] and the photodissociation of dimethyl cadmium on cadmium island films[159].

For weakly adsorbed species on metal surfaces (species for which discrete molecular electronic states, perturbed only slightly from gas phase values, still exist following adsorption) there are basically four mechanisms for the dispersal of energy following resonant absorption by the molecule: (1) radiative decay of the excitation (fluorescence or phosphorescence), (2) nonradiative decay of the excitation due to a transfer of energy to a continuum of

states or to a particular resonance of the metal substrate, (3) desorption of the molecule by transfer of energy to molecule-surface vibrational modes, and (4) chemical reaction of the adsorbed species. We are relatively certain that nonresonant surface excitation (surface heating) does not play a significant role in the photoreactions we have observed for several reasons: a calculation of surface heating rates based on effective optical constants determined for our rough surfaces by ellipsometry show a negligible temperature rise (less than 1°C), and photodecomposition is observed experimentally for molecules separated from the surface by a spacer layer. In addition, the trend in calculated surface heating rates with wavelength in Table 3 does not match that observed for photochemistry in Table 4.

In order to determine if photoinduced reactions of adsorbates can be generally observed, one must be able to predict whether or not energy dissipation through one of the other three pathways above will preclude reaction of the excited surface species. It is well known that energy transfer to a metal via the near field of an excited dipole becomes very rapid as an excited molecule is brought close to a metal surface. In many cases this eliminates the emission of observable fluorescence or phosphorescence, since the lifetime of the molecular excited state becomes extremely short in close proximity to the surface. Because of this damping the initial photoreaction step must occur very rapidly to compete with de-excitation of the excited state by energy transfer to the surface. For some molecules, rapid intersystem crossing rates (perhaps enhanced by interaction of the adsorbates with the surface) may allow population of triplet states

Table 3. Relative Raman enhancements and surface heating rates as a function of wavelength.

	Raman Enhancement	Surface Heating Rate
350.7 nm	0.014	4.5
363.8 nm	0.055	2.9
406.7 nm	0.13	1.6
457.9 nm	0.43	1.0
514.5 nm	1.00	1.0
647.1 nm	0.11	1.0

Table 4. Relative Photodecomposition Rates at 350.7 and 406.7 nm for 20-mW incident laser power.

	rate	
	406.7 nm	350.7 nm
benzene	1.0	3.6
pyridine	35	14
pyrazine	490	10
aniline	97	<1.0
benzaldehyde	140	2050
acetophenone	<0.2	

with intrinsically longer lifetimes than the initial photoexcited state, from which reactions may occur. If the initial excitation step is a two photon process, excitation of states not coupled to the ground state by strong dipole transition moments may occur. In this case de-excitation could proceed much more slowly, allowing time for chemical reaction.

Provided that the molecular excited state survives long enough on the surface for reaction to occur, an enhancement of reaction rate for surface[156] adsorbed species relative to free molecules may be expected. A theoretical treatment of silver spheroids on a conducting half-plane[160] indicates that enhanced local fields are experienced by molecules near a rough silver surface at frequencies near plasmon resonances of the spheroids. Experimental confirmation of the existence of these enhanced fields has been provided by a variety of experiments including surface enhanced Raman scattering and the observation of efficient second harmonic generation[161] on rough silver surfaces. Enhancement of local surface fields should yield enhanced absorption by molecules at the surface and hence an increase in photoreaction rate.

In the following sections we will first discuss the observed surface photochemical behavior of a number of aromatic molecules with 406.7 nm excitation, together with relevant gas phase absorption and fragmentation data. The dependence of the surface photofragmentation rate on excitation wavelength, surface temperature, and distance from the surface will then be presented for pyridine decomposition on silver. Finally, we will discuss the implications of our data for fragmentation pathways and for the possibility of observing

photochemical reactions when the excited state is rapidly damped.

II. Experimental Procedure

Photodecomposition of a large number of different molecules on rough silver substrates in UHV was investigated using the visible and near UV output of argon and krypton ion lasers. Decomposition was observed by monitoring the Raman spectrum of the molecule under irradiation in the graphitic carbon C-C stretch region of the spectrum near 1580 cm-1, using the same laser light for Raman scattering that is used to cause fragmentation of the molecule. Laser intensities used were in the range of 20-1000 W cm-2, obtained by focussing the output of the ion lasers to a 50x130 μm ellipse on the silver surface with a 350 mm focal length lens.

Spectroscopy and photochemistry were done using p-polarized light incident at 70° from surface normal. Scattered light was collected normal to the silver crystal surface using an f/1.0 fused silica collimator inside the vacuum chamber (Figure 37). The collimated light was brought out of the chamber through a quartz viewport and focussed onto the slits of a Spex 1400 double monochromator with an f-matching lens. The spectrometer was scanned using a stepping motor under the control of an LSI-11 microprocessor, and signal was detected using a photomultiplier with photon counting electronics. For UV spectra an EMI 6256S phototube was used, cooled to -50°C with dry ice and operated at -1300 V. Spectra in the visible region were collected using an RCA 31034A-02 photomultiplier cooled to -20C in a thermoelectric cooler and operated at -1500 V.

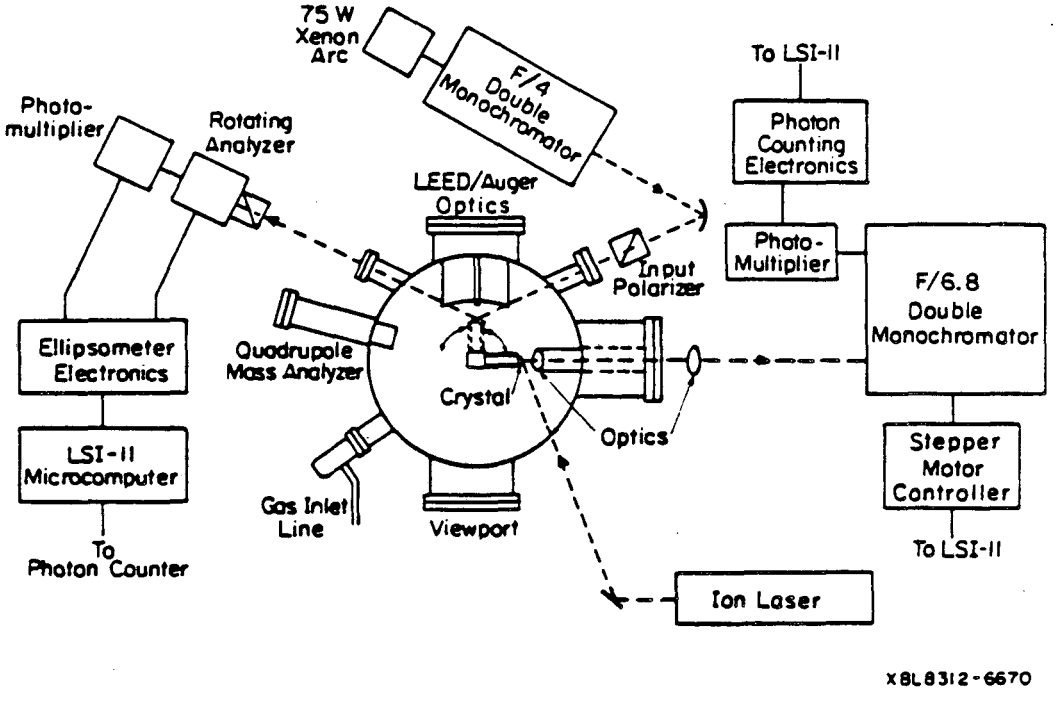

Figure 37. Schematic view of the vacuum chamber used for photodecomposition experiments.

The signal was routed to the microprocessor via a 32-bit binary counter (LSI Computer Systems LS7060) and stored on a magnetic disk.

The experiments were performed in a UHV work chamber equipped with LEED and Auger optics for surface characterization, and a quadrupole mass spectrometer for residual gas analysis and thermal desorption studies. Base pressure in the chamber was $8x10^{-11}$ Torr after bakeout at 200°C, and was in the range of $2\text{-}5x10^{-10}$ Torr during the course of the experiments. The silver crystal was mounted inside the chamber on a manipulator equipped with liquid nitrogen cooling coils to cool the crystal to 90 K for condensation of molecules on the surface. A resistive heater was mounted immediately behind the crystal and could be used in conjunction with the nitrogen cooling to maintain the crystal at any temperature between 90K and 1200K. The silver surfaces were cleaned prior to adsorption of molecules by sputtering at 500-2000 V with an argon ion sputtering gun (operated at $5x10^{-5}$ Torr Ar with 5 μA cm^{-2} ion current incident on the crystal in a defocussed beam).

Molecules were condensed on the crystal surface at 90 K by raising the pressure in the chamber to $5x10^{-9}\text{-}1x10^{-6}$ torr (uncorrected for ion gauge sensitivity) for the desired exposure time. No line of sight exposure system was used. Calibration of surface molecule coverages was done by ellipsometry using a rotating analyzer ellipsometer.[162] This method allows non-destructive determination of overlayer thicknesses from submonolayer coverages to thick multilayer coverages. Its disadvantage, though, is that changes in ellipsometric parameters are interpreted in terms of a simplified model consisting of a flat isotropic substrate and an

overlayer separated by a sharp boundary. These conditions are obviously inappropriate for the roughened surfaces used in this study, so coverage calibrations were done on smooth, well-ordered crystal surfaces obtained by sputter/anneal cycles on electropolished single crystals. Results of the calibration indicate approximately monolayer coverage for a 5L (1L = 10^{-6} Torr sec) exposure of pyridine.

The surfaces used in this study were silver single crystals oriented to the 110 surface plane, roughened by sputtering or electrochemical cycling and then sputtering. Crystals were cut by spark erosion from a high purity rod (Aremco products, 99.999+ %) and oriented by Laue diffraction to within ±0.5° of the desired surface plane. The crystal surfaces were all initially prepared by mechanical polishing using a progression of grit sizes, finishing with a 0.05 μm Al_2O_3 slurry on a vibratory polisher. This procedure resulted in a mirror finish with submicron scratches visible by light or electron microscopy. The mechanical polishing procedure, however, leaves a surface damage region which produces ellipsoidal roughness features upon sputtering at 2000 V due to surface imperfections. It was sometimes difficult to reproduce these surfaces, though, so during the latter part of this work the crystals were subjected to several cycles of electrochemical roughening in 0.1M KCl (0.5 mA cm-2, 2 min) after mechanical polishing. Sputtering on these roughened crystals in UHV then produced roughness on the same size scale as the mechanically polished but unroughened crystals. The surface nonuniformity produced by electrochemical roughening apparently provides some of the surface defects necessary for the

formation of the sputtering-induced roughness features.

The surfaces were characterized in the work chamber by a variety of methods. A good indication of whether the crystals would enhance both Raman scattering and surface photodecomposition was the observed level of continuum background scattering in the Raman spectra. The degree of roughening was also characterized by observing surface plasmon emission during electron bombardment of the surface. Typically, a 50 μA beam of 750 V electrons incident normal to the surface was used to excite plasmon radiation. The light was collected at 65° from normal through an ellipsometer port with a 350 mm quartz lens external to the chamber. The light was then focussed into a Spex Doublemate spectrometer with 0.5 mm slits and detected with a 6256S photomultiplier. The relative degree of surface roughness is reflected in the height of the surface plasmon emission peak near 350 nm compared to the transition radiation peak at 325 nm (as shown in Figure 38). Kretschman et al.[163] have calculated emission parameters for normally incident electrons on rough surfaces and find that the surface plasmon emission peak intensity is proportional to $\langle s_h^2 \rangle k_h^2$ and the splitting between the two peaks is proportional to $(\langle s_h^2 \rangle k_h^2)^{1/2}$ where k_h is the dominant high wavevector component of surface roughness and $\langle s_h^2 \rangle$ is the mean square roughness height of these features.

Additional characterization of the crystal in situ was done using scanning ellipsometry. Data obtained on rough surface optical properties by ellipsometry is, however, of limited utility since it is well known that surface roughness can substantially affect apparent surface properties determined ellipsometrically[164]. In

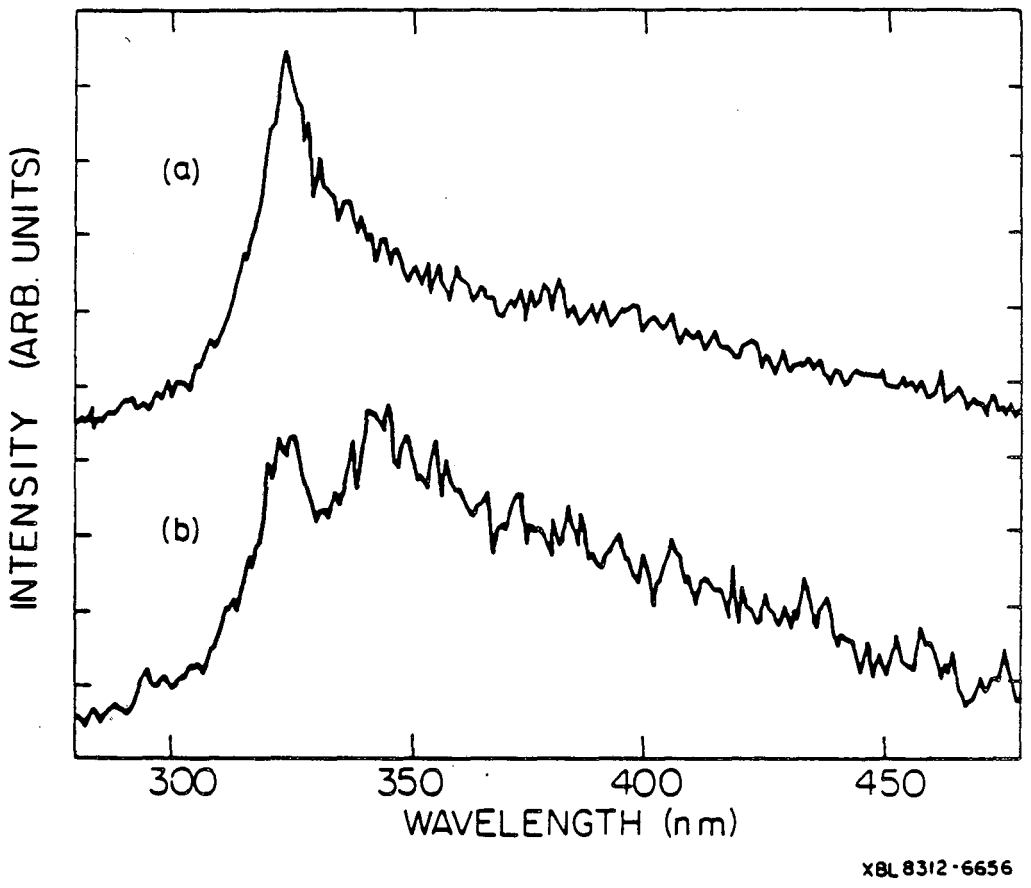

Figure 38. Light emission spectra from electron bombarded silver surfaces using a 50 uA beam of 750 V electrons. (a) Ag(110) annealed at 500°C. (b) Ag(110) sputtered 1 hour at 2000 V with Ar^+. The lower spectrum shows emission at energies below the surface plasmon energy due to roughness.

order to determine surface properties accurately the surface would have to be described using an inhomogeneous film model for surface roughness and have its properties calculated accordingly. Nevertheless, we can calculate effective surface optical constants for our rough surfaces from ellipsometric parameters. They show a maximum in the imaginary part of the refractive index at approximately 550 nm, consistent with the wavelength dependence of Raman enhancement for the roughened surfaces as shown in Table 3.

After the crystals were removed from the vacuum chamber following experiments they were examined by scanning electron microscopy to determine surface morphology. Shown in Figure 39 is a photomicrograph of a typical Ag(110) surface after sputtering taken on an ISI DS-130 scanning electron microscope. Most apparent are the large conical features on a micron size scale resulting from sputtering, but also observable are features of a much smaller size (300-400 Å). It is roughness features on this smaller scale that should have plasmon resonances in the 400-600 nm wavelength region[160,165].

III. Results

A. Surface Enhanced Raman Spectroscopy Using Visible Radiation

Raman spectroscopy using 514.5 nm excitation was done to determine Raman enhancement factors for the surfaces under study and to characterize the distance dependence of the enhancement. The enhancement factors were calculated for our surfaces using the observed Raman signal from the 1005 cm^{-1} ring breathing mode of

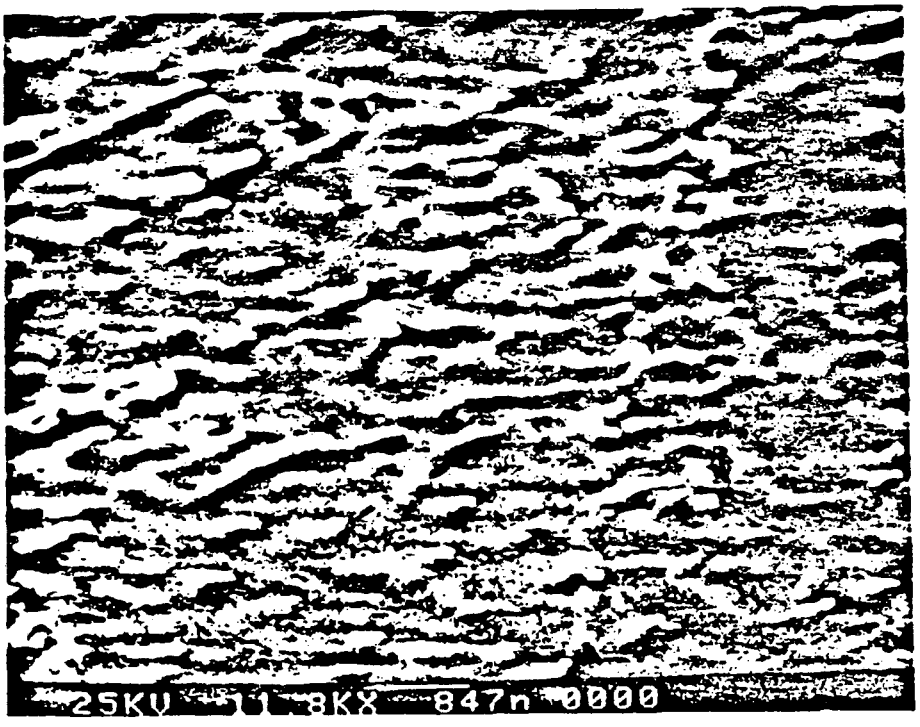

Figure 39. Electron micrographs of Ag(110) mechanically polished to 0.05 μm and sputtered at 2000 V in UHV. Top: micron sized roughness features at 11800X magnification. Bottom: 300 Å roughness features at 46800X magnification.

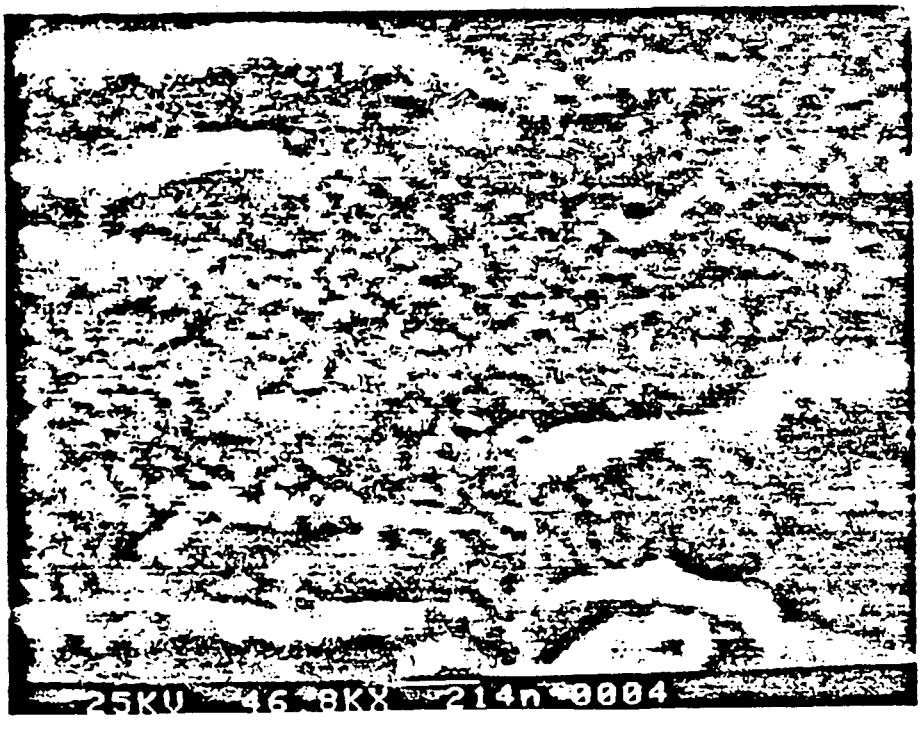

pyridine. The throughput of the optical system was calibrated by flooding the work chamber with an atmosphere of nitrogen and observing the intensity of the nitrogen band at 2331 cm^{-1}. The enhancement for the first layer of pyridine (5 L exposure) was calculated to be 1000 ± 20% for a typical surface.

Present in all of the Raman spectra taken on roughened silver surfaces is a strong peak near 1600 cm^{-1}, with weaker peaks near 700 cm^{-1}, 1350 cm^{-1}, and 3000 cm^{-1}. These peaks are due to residual amorphous carbon[166,167] and remain evident in Raman spectra with visible excitation even after extensive sputtering of surfaces that show no evidence of carbon by Auger spectroscopy. Auger, however, is only sensitive to approximately 0.2 monolayer of carbon due to interference with the silver 266 V peak. A rough estimate of the amount of residual carbon on the surface can be obtained by using the normal Raman cross-section for graphitic carbon of 4.4×10^{-28} cm^2 str^{-1} $atom^{-1}$ [168] and assuming the same enhancement factor for atoms at the surface as observed for pyridine. The residual surface carbon coverage for a typical surface was calculated to be 1.3×10^{13} atoms cm^{-2}. Taking a monolayer coverage of carbon as 8×10^{14} atoms cm^{-2},[169] this corresponds to 0.03 monolayer.

The high Raman cross-section of graphitic carbon also permits easy comparison of the relative Raman enhancements at wavelengths for which scattering from other adsorbed molecules is beyond the sensitivity of our detection equipment. Tabulated in Table 3 are the relative enhancement factors calculated from residual carbon peak heights at the Ar and Kr laser frequencies used in these experiments. The data indicate a peak in enhancement in the green region of the

spectrum corresponding to a plasmon resonance in surface roughness features.

The distance dependence of Raman enhancement for these surfaces was investigated by observing the Raman signal for the ring breathing modes of pyridine as a function of pyridine coverage (Figure 40). Results are similar to those observed for other roughened silver surfaces:[170] at submonolayer coverages, the symmetric ring breathing mode at 1005 cm^{-1} is selectively enhanced with respect to the asymmetric ring mode at 1035 cm^{-1}. At half monolayer coverage, the 992 cm^{-1} mode begins to show up as pyridine is no longer π-bonded to the surface (or as a particular surface site is saturated). There is a sharp saturation in the growth of all three peaks at approximately monolayer coverage. The first monolayer appears to be enhanced by a factor of approximately 1000 and the next several monolayers by a factor of 60 to 80.

B. Photodecomposition

1. Decomposition using 406.7 nm excitation

All of the molecules investigated for photodecomposition on rough silver (with the exception of benzaldehyde) showed a maximum decomposition rate at 406.7 nm compared to the other ion laser lines used in the study (Ar 363.8 nm, 457.9 nm, and 514.5 nm; Kr 350.7 nm). One of the few things that all of the molecules exhibiting photodecomposition at this wavelength have in common is the lack of any electronic states at or below this energy. Recent studies of the electronic states of aromatic molecules adsorbed on silver[171] indicate that the low lying electronic states of benzene, pyridine, and pyrazine are perturbed by only a few tenths of an eV from gas

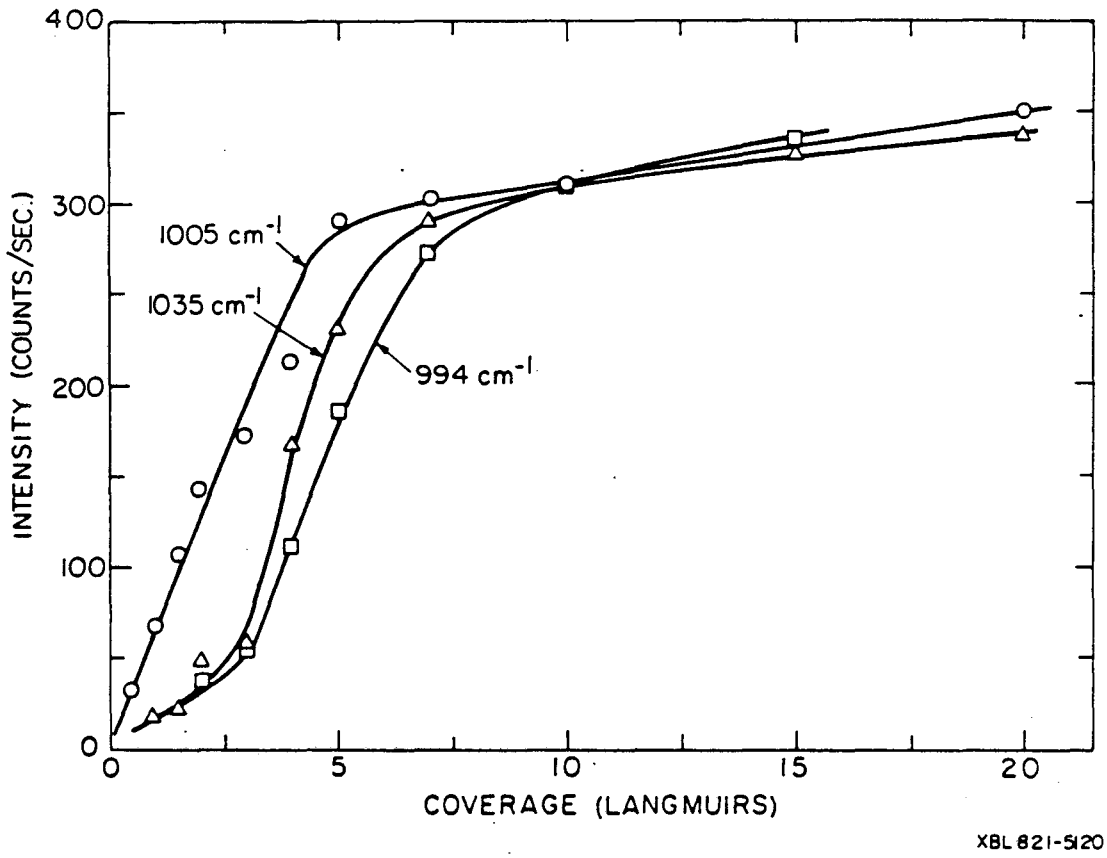

Figure 40. Coverage dependence of surface enhanced Raman signal for pyridine adsorbed on roughened Ag(110) at 90 K for several ring-breathing modes.

phase values by interaction with the metal surface. It is thus highly unlikely that the low lying electronic states of any of the aromatic molecules studied are shifted sufficiently by interaction with the surface to be in resonance with the laser excitation energy.

The only possibilities energetically allowed for absorption by the molecule are the simultaneous absorption of two or more photons, or frequency up-conversion at the metal surface followed by molecular absorption. To differentiate between these two absorption processes we compare two photon absorption (using a typical cross section of 10^{-50} cm^4 sec $molecule^{-1}$ $photon^{-1}$) to that of surface second harmonic generation (SHG) followed by an allowed one photon absorption (cross section 10^{-15} cm^2 $molecule^{-1}$). Using the highest values for surface SHG reported for silver surfaces (for 1.06 μm incident on electrochemically roughened surfaces[172]) we find that excitation via two photon absorption is several orders of magnitude larger than that of SHG followed by a one photon absorption. Studies of SHG on rough silver at shorter wavelengths (683 nm) where Raman enhancement is 10^6 show a drop in SHG intensity by a factor of 100 from that observed at 1.06 μm.[173] Although data is lacking for the wavelengths and exact surface structures employed in our experiments, the available evidence implies that two photon absorption is by far a more efficient process than SHG followed by absorption. A similar conclusion was reached in two photon fluorescence experiments on silver island films[174] where SHG was found to be too small to account for the observed fluorescence signal.

A two-photon initial absorption step in our photofragmentation experiments is supported by studies of the initial decomposition rate

as a function of incident laser power for pyridine and benzaldehyde. As shown in Figure 41 the photodecomposition rate for pyridine with 406.7 nm excitation varies approximately as the square of the incident light intensity for laser power between 5 and 50 mW. Some saturation of initial decomposition rate is observed for higher incident power. This is apparently due to depletion of molecules on the surface, since although appreciable surface carbon increase is still observed several minutes after irradiation is begun, it occurs at a much lower rate than that observed initially. Possible mechanisms for energy redistribution and fragmentation following multiphoton absorption will be discussed in the next sections.

Pyridine and Pyrazine The electronic states of the azabenzenes have been quite thoroughly studied.[175] The presence of lone pair electrons on the nitrogen heteroatoms of these molecules give rise to strong $n\pi^*$ transitions not observed in benzene. Shown in Figures 42 and 43 are the energy levels of known electronic excitations labeled with excited state symmetries for gas phase molecules. Electron energy loss studies of these molecules adsorbed on Ag(111)[171] show energy levels of the adsorbed phase molecules 0.1-0.2 eV higher than values observed in the gas phase.

The three most prominent transitions observed in both gas phase and condensed phase one-photon absorption spectra of pyrazine ($^1B_{3u}$, $^1B_{2u}$, and $^1B_{1u}$) are not allowed for two photon transitions due to their odd parity. For molecules adsorbed on a surface, though, these symmetry rules may be broken by interaction with the surface. In any case these states can have vibronically allowed two photon transitions, and the B_{3u} state has been studied by two photon

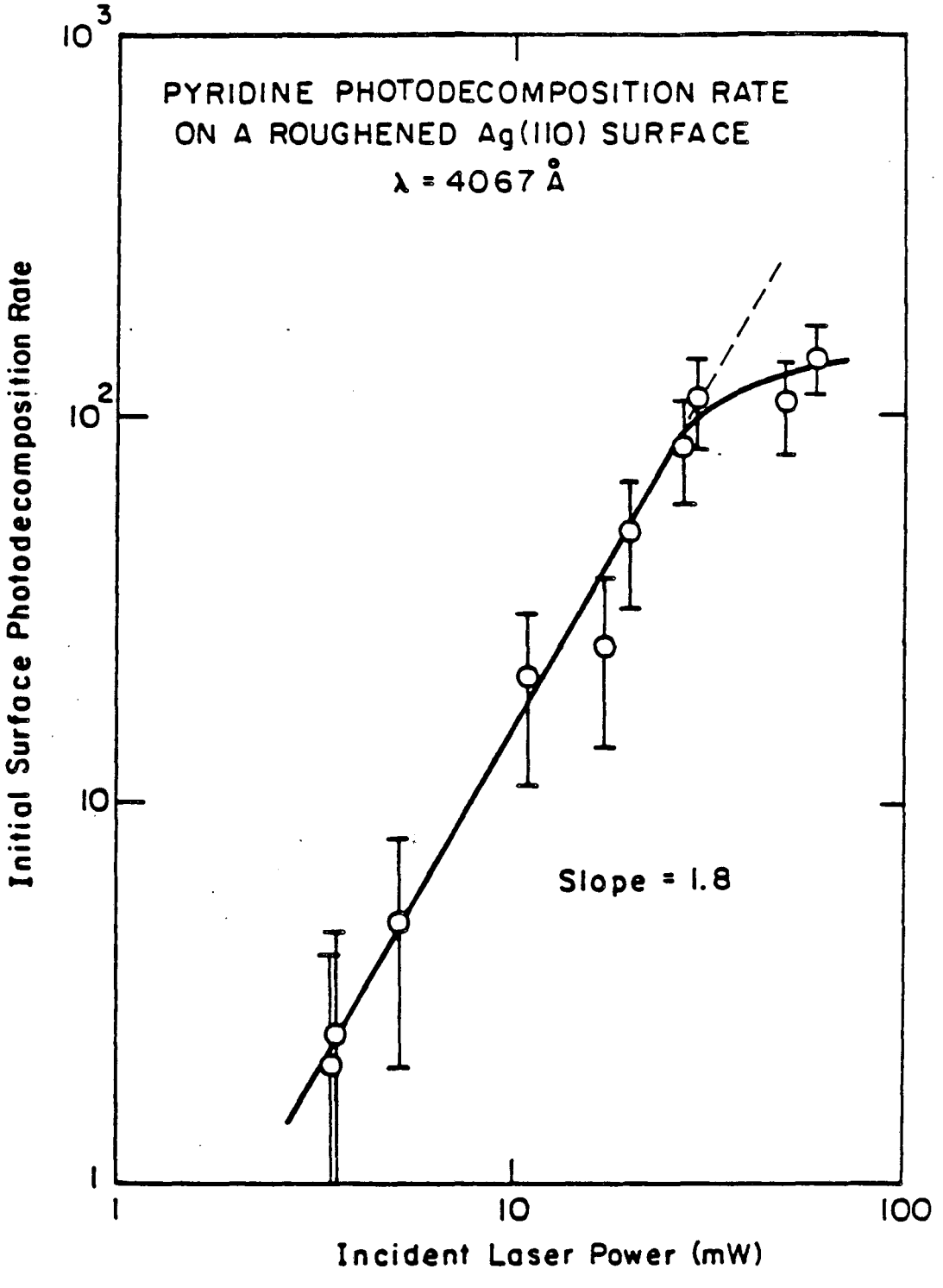

XBL 831-5090

Figure 41. Photodecomposition rate as a function of incident laser power for 10 L pyridine adsorbed on roughened Ag(110). Decomposition rate is measured as a change in the Raman signal per unit time (counts/s^2), corrected for the difference in Raman intensity at different incident laser intensities.

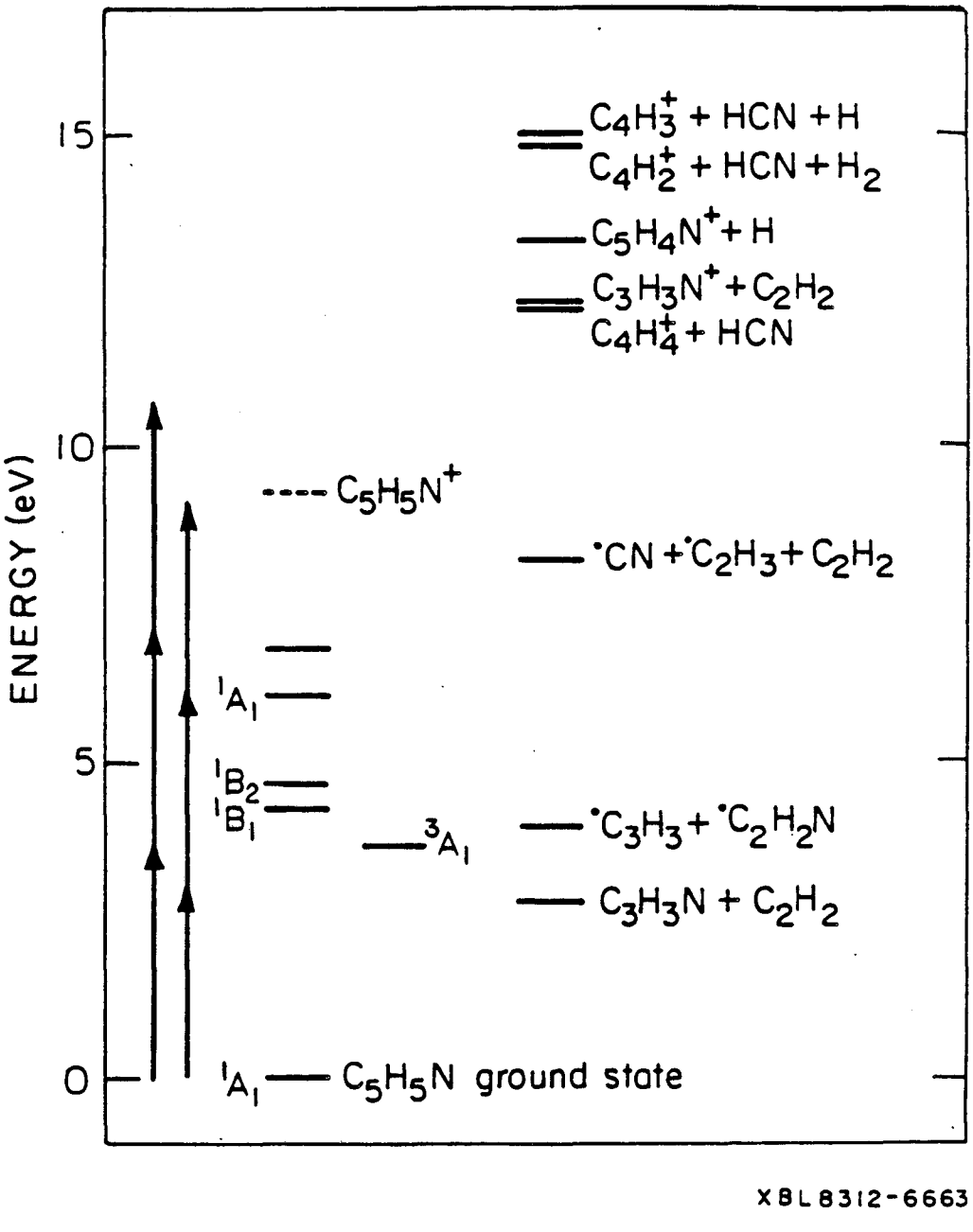

Figure 42. Energy levels of pyridine and appearance potentials of possible fragmentation products. The arrows along the left side correspond to the energies of photons at 350.7 nm and at 406.7 nm.

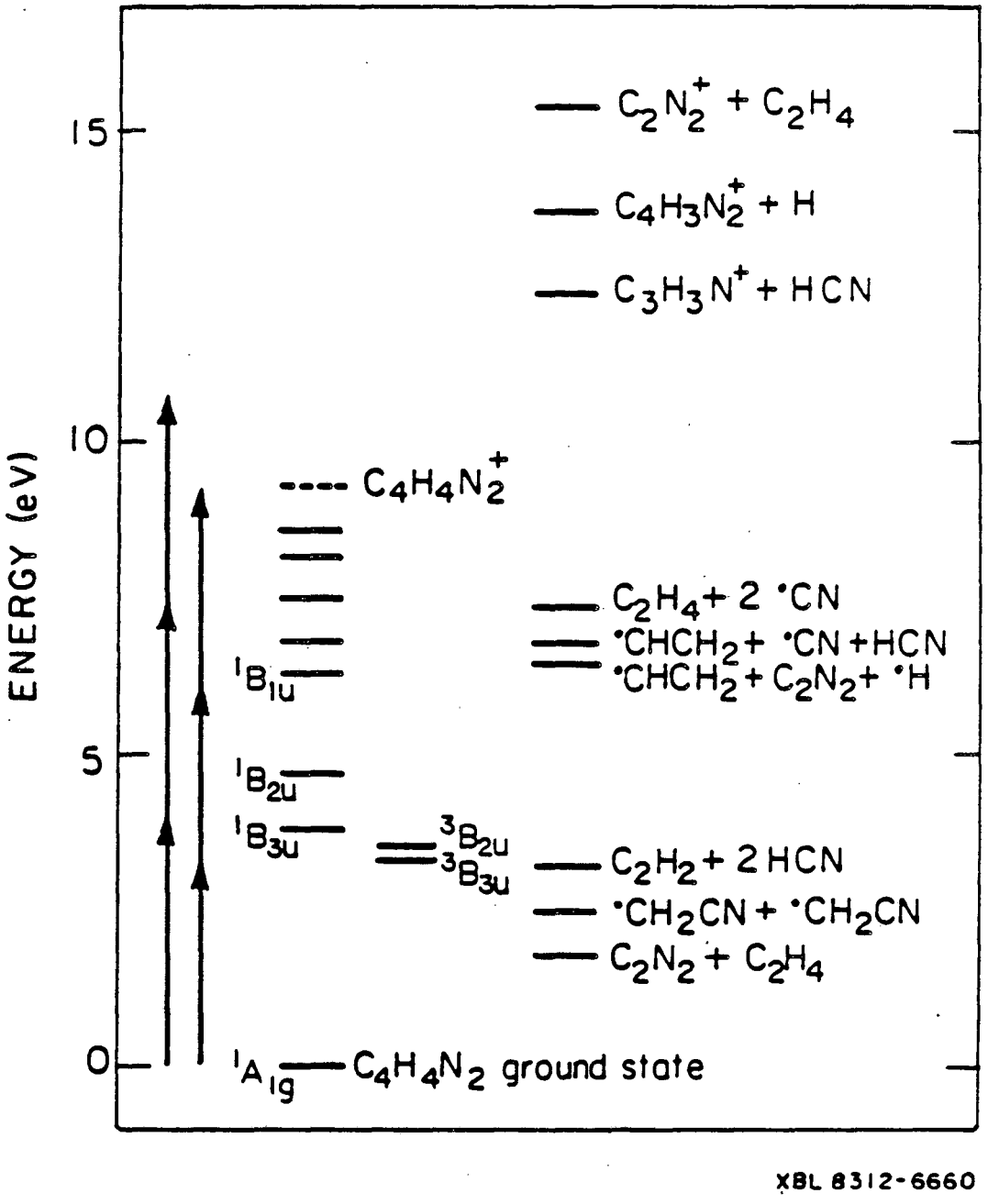

Figure 43. Energy levels of pyrazine and appearance potentials of possible fragmentation products.

absorption with fluorescence and phosphorescence detection.[176,177] Studies of gas phase pyrazine in the energy region for two photon absorption at 406.7 nm (6.10 eV) produced no evidence for vibronically allowed absorption to the $^1B_{1u}$ state, though, but instead showed a two photon allowed n→3s (A_1 transition to a Rydberg state.[178,179] This transition may not be observed in condensed phases, however, since Rydberg states are generally weakened substantially as well as broadened compared to the gas phase.[180]

A study by Esherick et al.[176] of two photon absorption in pyrazine crystals indicates that the observed two photon transition intensities to the $^1B_{2u}$ ($\pi\pi^*$) state were much larger than their calculations of vibronic interactions indicated that they should be. Their hypothesis was that the majority of intensity in this region was due to the presence of a B_{2g} state at an energy slightly higher than that of the B_{2u} state. Recent calculations of pyrazine energy levels by SCF-CI[181] and valence bond[182] methods also place the $^1B_{2g}$ ($n\pi^*$) transition in this energy region rather than near the B_{3u} state as has been assumed by many others. Thus we can tentatively assign the initial absorption step in our pyrazine photodecomposition experiments to a two photon allowed transition to the $^1B_{2g}$ state.

Pyridine (C_{2v} symmetry) is a molecule of low symmetry compared to pyrazine (D_{2h}). Consequently, the electric dipole selection rules are much less restrictive for pyridine transitions and all of the symmetry species can give rise to an allowed two photon transition from the ground state. The initial absorption step in our studies of pyridine is most likely two photon absorption into the $^1A_1$ ($\pi\pi^*$) state at 6.2 eV.

Pyridine and pyrazine both readily photodecompose on rough silver surfaces with 406.7 nm irradiation (Table 3). There have been few other studies of the photodecomposition of these molecules - most attempts to photolyze pyridine and pyrazine have shown that they do not photodecompose under normal spectroscopic conditions.[183] Mathias and Heiklen,[184] however, have done a careful study of the gas phase photolysis of pyridine using intense light at 213.9 nm and 228.8 nm. They report that pyridine photodecomposes at a rate dependent on the total energy content of the excited state (whether thermal or photolytic) by molecular elimination into one molecule of acetylene and one molecule of acrylonitrile. At room temperature in their experiments the acrylonitrile leads predominantly to a polymer, while at high temperature (260°C) the acrylonitrile is photolyzed to form C_2H_2 and HCN and/or C_2N_2 and H_2.

The initial step in the surface photodecomposition of pyridine may be direct fragmentation to neutral molecule fragments as has been observed for the gas phase, or may involve other surface intermediate species such as radicals or ions. We have looked for intermediate species in surface photodecomposition reactions using Raman spectroscopy. The only evidence we have of intermediates in the decomposition of pyridine or pyrazine is the appearance of a CN stretching mode near 2200 cm^{-1} (Figure 44). This frequency is substantially shifted from the 2113 cm^{-1} vibration observed for CN adsorbed on a silver electrode surface[185] and may indicate the presence of larger fragments such as CH_2=CHCN (ν_{CN} = 2222 cm^{-1}) on the surface.

Shown in Figures 42 and 43 are the formation energies of a

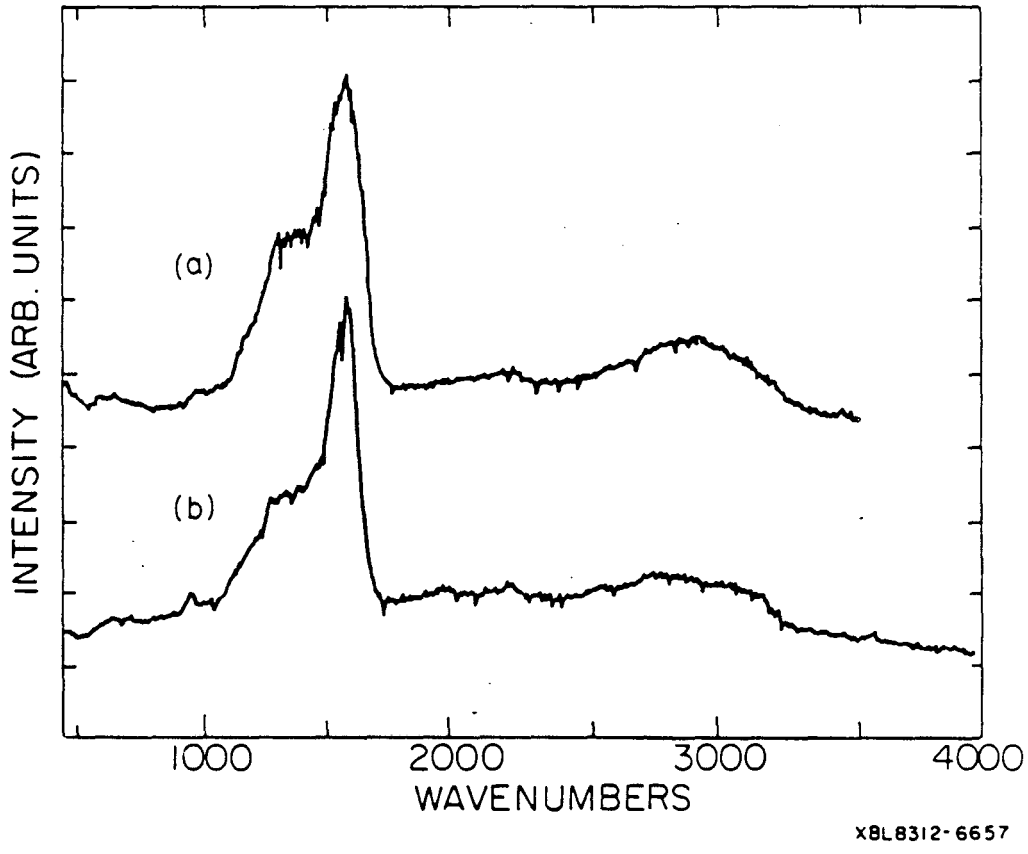

Figure 44. Raman spectra of photodecomposed pyrazine (a) and pyridine (b) using 406.7 nm excitation.

number of possible intermediate and product species in the photolysis of pyridine and pyrazine. Fragmentation may occur through multiphoton absorption into the ion continuum of states, followed by subsequent additional absorption steps and fragmentation. The formation of ionic fragments of pyridine has been studied by electron impact mass spectrometry[186] and by multiphoton ionization using 193 nm excitation.[187] The observation of charge-transfer excitations for pyridine and pyrazine adsorbed on silver[171] raises the possibility of fragmentation by excitation of a bonding electron into the silver continuum above the Fermi level for a molecule adsorbed directly at the surface. Jonsson et al.[188] indicate that excitation of a pyridine $1b_1$ electron (IP = 12.2 eV) from a strongly C-C bonding π orbital will break the ring.

Published reports of pyrazine photolysis are almost nonexistent. One of the few recent reports is the observation by Webb et al.[177] of fluorescence emission by cyanyl radicals following two photon absorption by pyrazine at 4.0 eV. The large number of relatively low energy radical fragments of pyrazine (Figure 43) indicates that radical formation is a likely fragmentation pathway for this molecule.

Benzaldehyde and Acetophenone Both benzaldehyde and acetophenone have also been well studied spectroscopically.[189] Although the molecules are very similar structurally and electronically, they exhibit strikingly different behavior photochemically in our experiments. Excitation for both molecules with 406.7 nm irradiation is probably two photon absorption into a $1A'$ ($\pi\pi^*$) state near 6 eV (Figure 45). This assignment is consistent

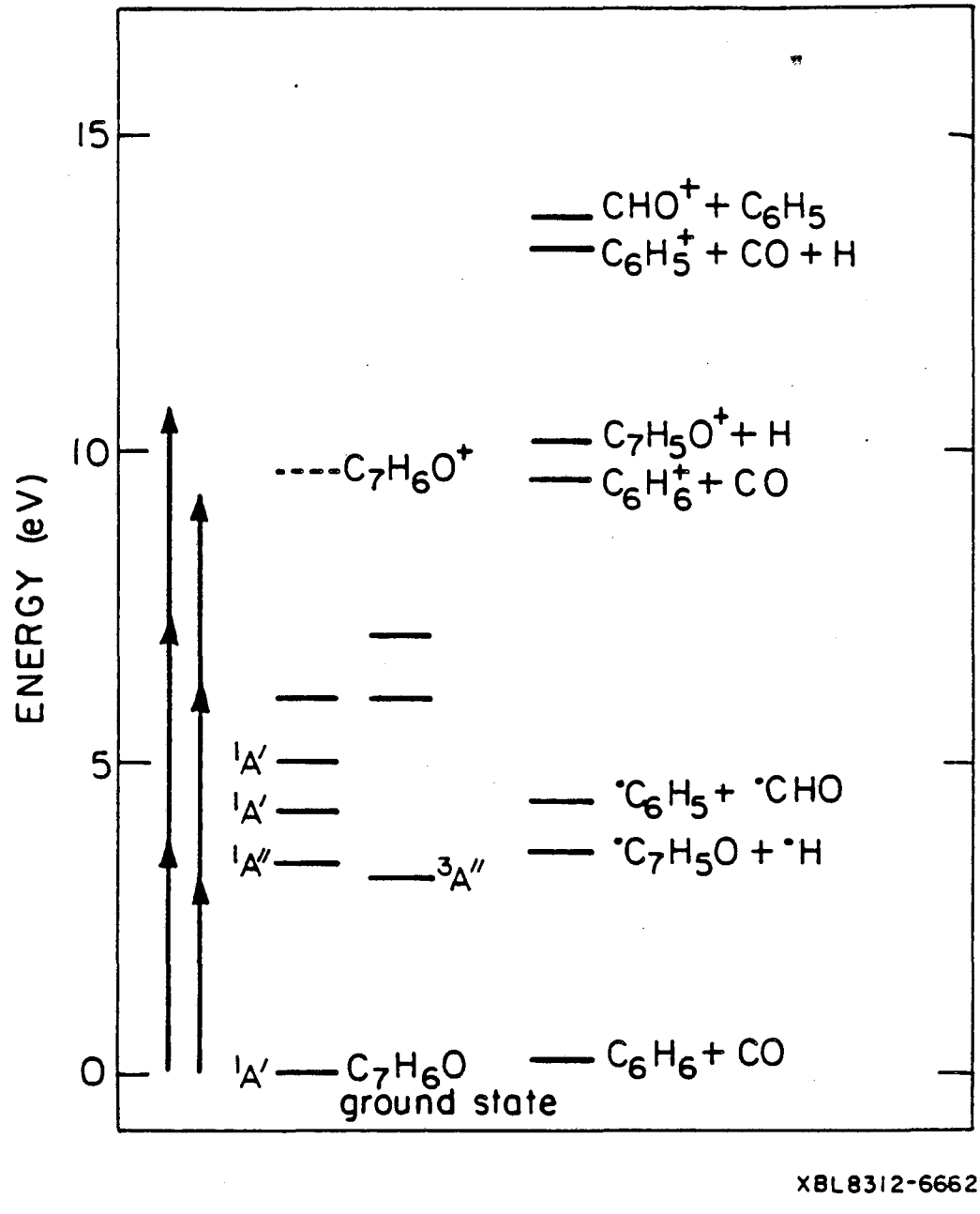

Figure 45. Energy levels of benzaldehyde and appearance potentials of possible fragmentation products.

with intensity dependence measurements for the photodecomposition of benzaldehyde which show an approximately quadratic dependence of rate on incident laser power. Acetophenone, however, shows no photofragmentation under our conditions.

The photochemistry of benzaldehyde has been investigated extensively by Berger et al..[190] They examined the photochemistry and phosphorescence emission of benzaldehyde for excitation into the first and second excited states (365 nm and 276 nm, respectively). For excitation into S_2, they found rapid population of two vibrationally excited triplet states which both dissociate at low pressure to form molecular benzene and CO. Collisional deactivation of these states yielded the lower vibrational levels of the lowest triplet state from which no photochemistry was observed. For excitation into S_1 no benzene or carbon monoxide formation was observed but benzaldehyde was consumed, leading apparently to polymer formation by a radical mechanism. The general features of this photochemical behavior were confirmed by Robin and Kuebler[191] who additionally found radical formation from excitation into S_3.

The photochemistry of acetophenone was found by Berger and Steel[192] to be qualitatively different than that of benzaldehyde as a function of excitation wavelength. For excitation into the S_1 ($n\pi^*$) state of acetophenone no photochemistry was observed. For excitation into S_2 ($\pi\pi^*$) rapid intersystem crossing was observed into a vibrationally excited triplet, which could then undergo decomposition to radicals at low pressure. At high pressures the excited state underwent collisional deactivation and photochemistry did not occur. The same type of collisional deactivation was observed for excitation

into S_3 of acetophenone.

Thus for excitation into highly excited singlet states, benzaldehyde and acetophenone both undergo decomposition to yield radicals. The difference between the two molecules appears to be that benzaldehyde undergoes a primary photochemical step at a far faster rate than the collision frequency to give radicals, while for acetophenone a second gas can quench free radical photochemistry by collisional deactivation. These gas phase photochemical results are consistent with the surface photochemistry we have observed for benzaldehyde and acetophenone. The faster fragmentation timescale of benzaldehyde may allow this pathway to continue to be important even in the presence of strong surface damping of the excited state where acetophenone is rapidly quenched, thus explaining the observed difference in fragmentation rates for these two molecules with two photon 406.7 nm excitation in our experiments.

The Raman spectra of benzaldehyde during photodecomposition at 406.7 nm and 350.7 nm show several interesting features (Figure 46). The peaks near 1000 cm^{-1} and 1180 cm^{-1} can be assigned to vibrational modes of adsorbed benzaldehyde. Although no new modes appear that can be assigned to surface intermediate species, the carbon mode that normally appears at 1350 cm^{-1} in other spectra of photofragmented molecules with 406.7 nm excitation is shifted. It appears at 1320 cm^{-1} in the 406.7 nm spectrum and at 1295 cm^{-1} in the 350.7 nm spectrum. This carbon peak in the 1300 cm^{-1} region is attributable to an in-plane A_{1g} mode of graphite which is silent for an infinite carbon layer but becomes active for small or imperfect layers due to relaxation of wavevector selection rules.[193] The shifts observed in

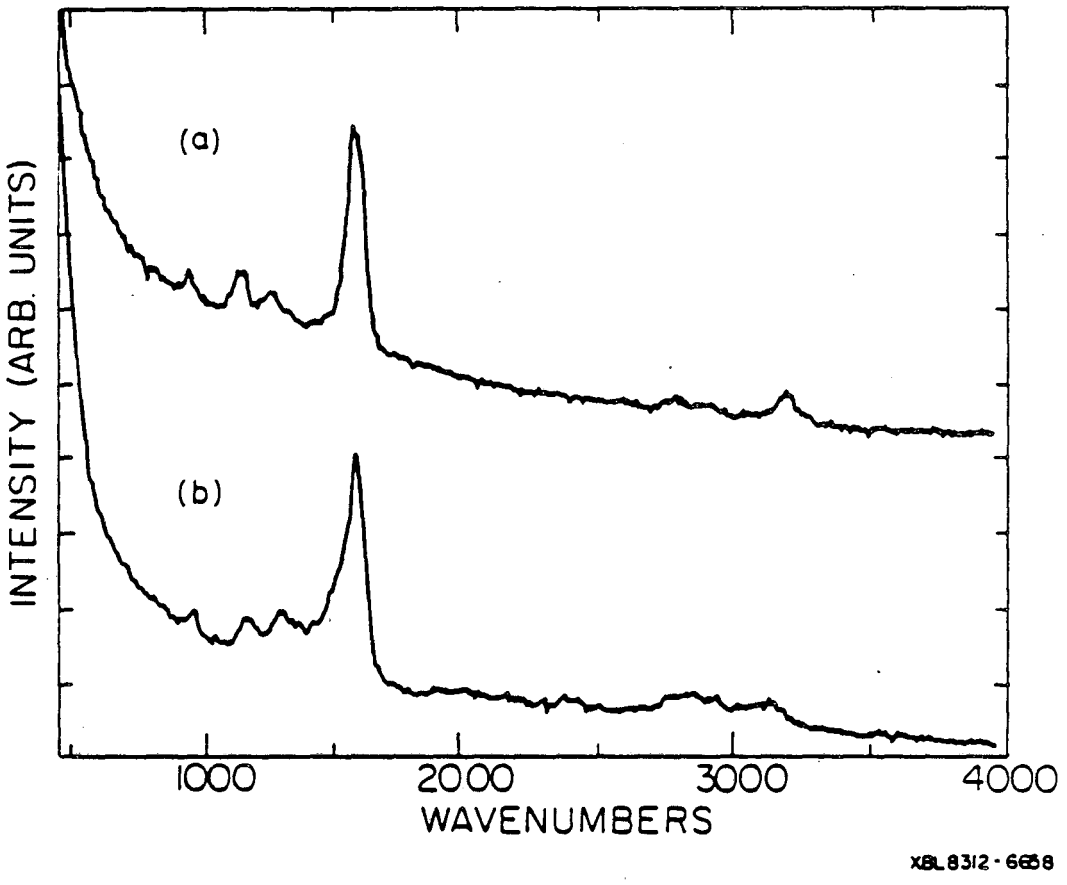

Figure 46. Raman spectra of photodecomposed benzaldehyde using (a) 350.7 nm excitation and (b) 406.7 nm excitation.

the benzaldehyde spectra are most probably due to differing surface carbon morphology.

Other Molecules Benzene, as mentioned in the preceding discussion, was one of the few aromatic molecules examined which did not decompose to any extent at 406.7 nm. The photochemistry of benzene has been examined extensively,[194] and while many isomers of benzene have been found to form upon excitation into lower singlet states, fragmentation has not been observed. Multiphoton ionization of benzene has also been studied extensively in both the gas[195,197] and liquid[196] phases. For excitation wavelengths near 400 nm, the ionization has been shown to be a three photon process with a two photon resonance at the $1B_{1u}$ state of benzene. Mass spectroscopy studies in the gas phase indicate that primarily the benzene ion is formed at low intensities, while substantial fragmentation is observed at higher intensities (approx. 10^{10} W cm^{-2}) resulting from absorption of up to nine photons.[197] Fragmentation of benzene thus appears to occur readily for sequential photon absorption by benzene ions, but not through neutral intermediates. Photochemistry under our conditions would depend on the generation and lifetime of benzene and fragment ions. If ionic intermediates are not sufficiently long-lived on the surface for further absorption of photons to occur, fragmentation to carbon would not be observed.

Aniline was found to decompose readily under the conditions of our study at 406.7 nm (Table 3). A survey of the energy levels of aniline (Figure 47) indicates that the lowest excited states of aniline are above the laser energy at 406.7 nm, but that there is a two photon resonant state at 6.1 eV. Aniline dissociation has been

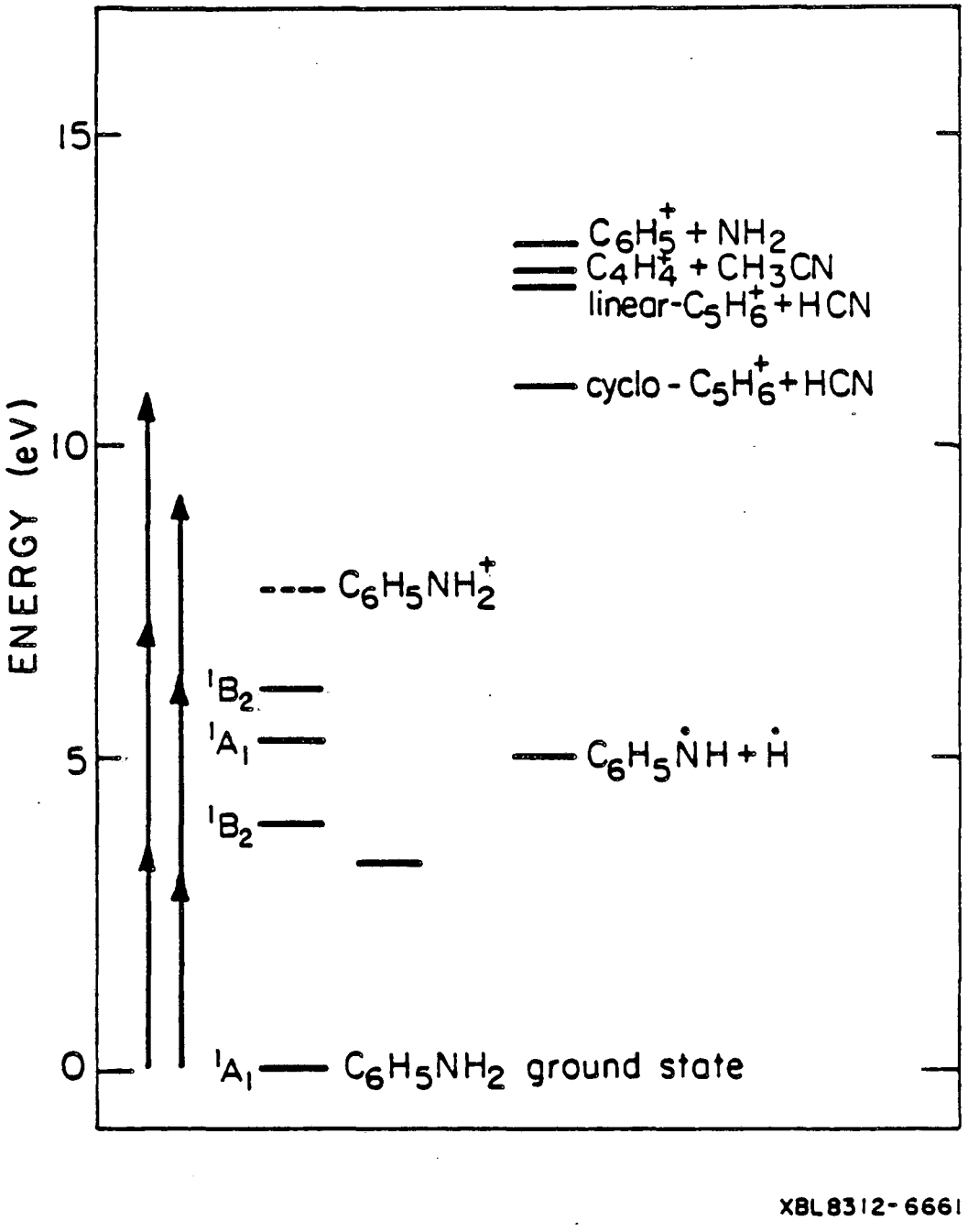

Figure 47. Energy levels of aniline and appearance potentials of possible fragmentation products.

studied by flash photolysis in solution[198] where anilino radical formation has been observed. Aniline cation radicals were found under the same conditions in higher dielectric constant solvents. Multiphoton ionization and fragmentation of aniline in the gas phase has also been observed[199,200] with an order of magnitude higher cross-section than that of benzene.[200] Photofragmentation under our conditions may occur by either of these mechanisms following resonant two photon absorption.

2. Decomposition at other wavelengths

As indicated in Table 4, photodecomposition rates were investigated for a number of molecules for excitation with both 406.7 nm and 350.7 nm light from a krypton laser. In general, with the exception of benzaldehyde and possibly benzene, the measured decomposition rate after correction for Raman detection efficiency (Table 3) was higher at 406.7 nm than at 350.7 nm. For one of the molecules studied, pyridine, decomposition rates were measured at several intermediate wavelengths (356.4 and 363.8 nm) and were found to be smoothly decreasing toward shorter wavelengths. Pyridine photodecomposition was also looked for at 457.9 nm and 514.5 nm - no decomposition was observed at these wavelengths for the same incident power as used in the UV experiments (20 mW). The photodecomposition rate is peaked near 400 nm, then, with a gradual decrease in rate at shorter wavelengths and a sharp falloff at longer wavelengths.

As mentioned earlier, the wavelength dependence of Raman enhancement on the surfaces used in this study were determined by measuring carbon 1580 cm^{-1} peak height at constant energy resolution for the various excitation wavelengths available. Raman enhancement

at 350.7 nm is a factor of 9 smaller than that observed at 406.7 nm, while the enhancement at 457.9 nm is a factor of 3 larger than that observed at 406.7 nm. If photodecomposition rate and Raman enhancement are controlled by the same mechanism then one should observe a decreasing photodecomposition rate as the exciting wavelength is changed from 406.7 nm to 350.7 nm and the Raman enhancement drops, provided that there are no dramatic changes in the cross-section for electronic excitation at these wavelengths. This appears to hold true for pyridine, pyrazine, and aniline - broad absorption peaks near 6 eV are observed for all these molecules. A sharp drop in decomposition rate at longer wavelengths is expected as there will no longer be a resonant two photon absorption.

An entirely different trend is seen, however, with benzaldehyde. The photodecomposition rate at 350.7 nm is 1.5×10^2 times faster than at 406.7 nm. Looking at the energy levels of benzaldehyde it can be seen that the energy of a single laser photon at 350.7 nm is now above the lowest singlet $n\pi^*$ transition. Berger, Goldblatt, and Steel[190] report that gas phase benzaldehyde undergoes polymerization via a radical mechanism upon excitation into S_1. We propose that in our surface experiments benzaldehyde undergoes decomposition also directly from the lowest excited singlet. This hypothesis is supported by laser power dependence studies of photodecomposition rates at 350.7 nm and 406.7 nm. At 406 nm the fragmentation rate depends on the square of the incident power for low laser powers, while at 350 nm the dependence becomes linear in laser power. Thus in this case fragmentation to carbon atoms begins as a result of single photon absorption with a higher absorption probability at the

intensities used in these experiments than that for two photon processes.

C. Temperature Dependence

Preliminary experiments were done to investigate the temperature dependence of pyridine photodecomposition on rough silver. Photodecomposition of pyridine on a surface maintained at 125 K showed an initial decomposition rate a factor of 15 larger than that observed when the surface was at 90 K. When the surface temperature was raised to 170 K no fragment carbon signal increase was observed, corresponding to desorption of molecules from the surface. Thermal desorption spectra for a monolayer coverage of pyridine adsorbed on the surface show a desorption temperature of 165 K (this corresponds to a physisorbed pyridine desorption peak reported by others;[201] higher temperature peaks in our spectra may be buried under background desorption from other surfaces in the vacuum chamber).

This preliminary data indicates that the reactions leading to surface carbon are thermally activated, possibly by activation of surface migration of intermediate species. A more detailed study of the temperature dependence of surface photofragmentation is necessary before any more definitive conclusions can be drawn.

D. Distance Dependence

In order to determine whether or not the photofragmentation process observed on our silver surfaces depends on distance from the surface in the same way as Raman enhancement, molecules of a

substance which showed surface photodecomposition (pyridine) were spaced varying distances from the silver surface with a layer of a substance which did not show any appreciable decomposition (benzene). The thickness of the spacer layers was determined by exposing the surface at 90 K to a timed exposure of the spacer molecule. The exposures were calibrated on a smooth silver surface by ellipsometry, which indicated a 10 ± 2 Å coverage of both benzene and pyridine for a 10 L exposure.

Photodecomposition rate was measured for a 20 L exposure of pyridine on rough silver with varying thicknesses of an intervening spacer layer. The results are depicted in Figure 48, where it is seen that the initial decomposition rate increases for 10 L and 20 L spacer layers but decreases again for thicker spacer layers. It is evident from these results that the mechanism responsible for enhancement of photofragmentation shows a component with a much more extended range from the surface than excited state damping by dipole coupling to surface modes. This topic will be discussed further in the following section.

IV. Discussion

A. Energy Damping vs. Photofragmentation

As discussed by Nitzan and Brus,[156] the observation of enhancement in photochemical reactions near a metal surface will depend on the interaction of two competing factors: enhanced accumulation of energy by the molecule due to interaction with the surface versus very effective transfer of energy from the molecule to

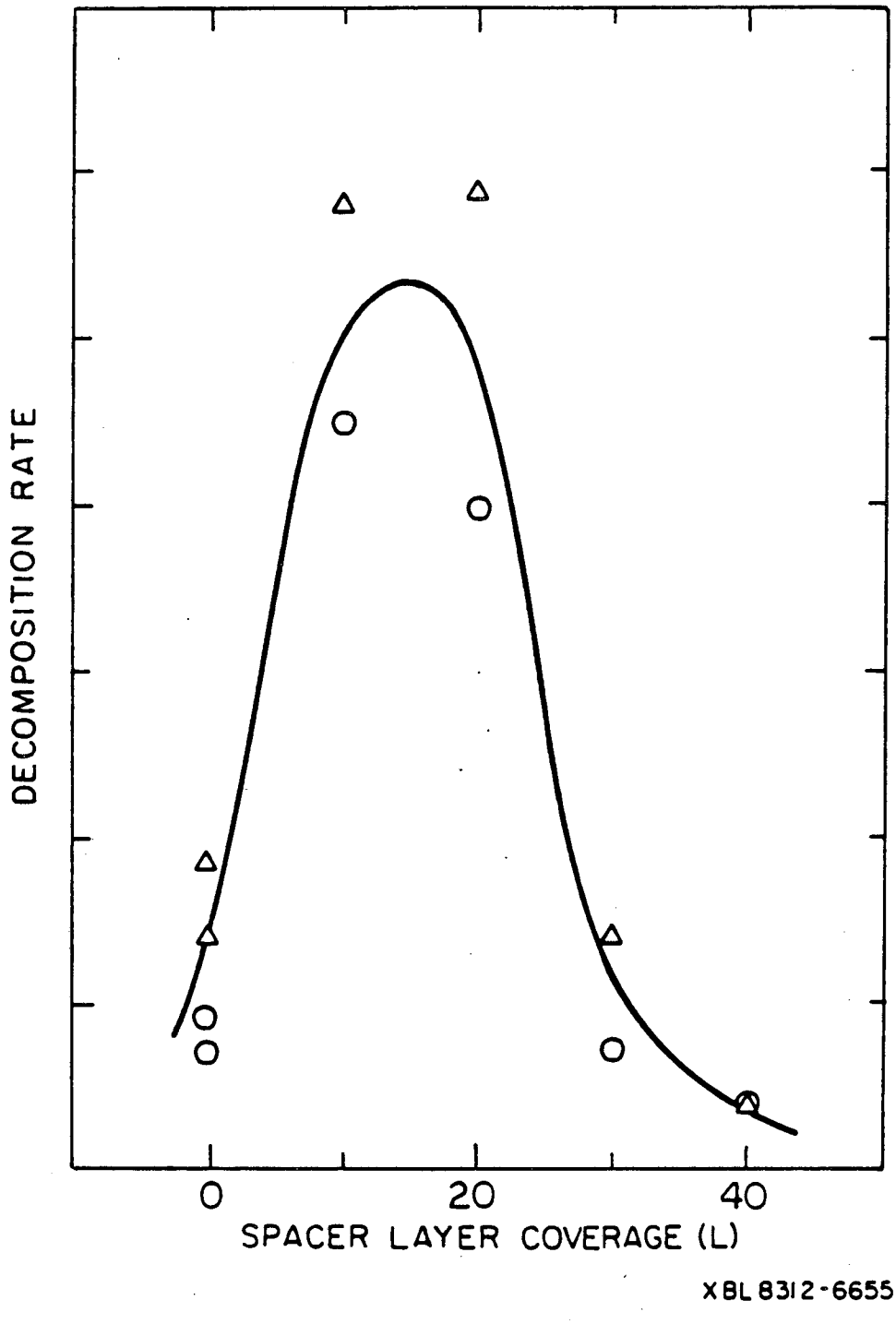

Figure 48. Photodecomposition rate for 20 L pyridine deposited on a benzene spacer layer of varying thickness with 406.7 nm excitation. The different symbols correspond to experiments on different areas of the same crystal.

the metal at short distances. Considering first the process of energy damping by the metal surface, it has been shown that the simple classical image formula for the nonradiative decay rate via dipole coupling

$$b = \frac{b_0 q \Theta}{4d^3} \mathrm{Im}\left[\frac{\epsilon_2 - \epsilon_1}{\epsilon_2 + \epsilon_1}\right] \tag{50}$$

predicts quantitatively the rate of energy damping for a molecule as close as 10 Å to a silver flat surface.[202] In this equation b_0 is the radiative decay rate, q is the quantum efficiency, d is the normalized surface separation, ϵ_1 and ϵ_2 are the dielectric and metal optical constants, respectively, and Θ is a dipole orientation parameter. Since the surfaces employed in our experiments are not flat, however, we must account for the deviation of these surfaces from a planar geometry in order to predict energy transfer rates accurately.

If the roughness features of the silver surfaces can be approximated as spheres, the energy transfer rate to resonant modes of the sphere can be calculated.[156,203,204] For cases where the molecule is very close to the surface of the sphere (d << sphere diameter), the calculated nonradiative energy transfer rate is given to a good approximation by the rate calculated for a molecule on a plane surface. Calculations of energy transfer rates to randomly rough surfaces have also been done using perturbation theory.[205] Rates an order of magnitude or more greater than those of flat surfaces have been calculated, but the applicability of these results

to surfaces with large scale roughness (> 100 Å) is questionable. For the purposes of energy transfer calculations, then, we will approximate our surfaces as being planar.

While classical dipole theory is adequate to describe energy transfer for distances greater than 5-10 Å from the surface, at shorter distances it is likely to break down.[206] In addition, for excited molecules very close to the surface where there is substantial metal-molecule wavefunction overlap the possibility of energy decay via electron exchange between the surface and the molecule must also be considered. These mechanisms, first summarized by Hagstrum,[207] are depicted schematically in Figure 49. Recent work[208] has attempted to determine the importance of electron exchange energy transfer mechanisms relative to image dipole coupling. We cannot presently make any estimates of the importance of these mechanisms for energy damping of excited molecules near our surfaces; however the interesting possibility of collecting and energy analyzing Auger electrons generated by these processes during laser irradiation could help answer this question.

An estimate of the consequences of ignoring these corrections to the image formula for calculating energy transfer rates for the type of system we are working with can be obtained from the work of Avouris and Demuth18 who have determined the lifetime of pyrazine adsorbed on Ag(111) from electron energy loss linewidths. They estimate the surface lifetime of the pyrazine $1B_{2u}$ state to be $5x10^{-15}$ sec for the first monolayer and $3x10^{-14}$ sec for the second layer, assuming their measured linewidths to be homogeneous. An image calculation of the lifetime gives a prediction of $1.1x10^{-15}$ sec

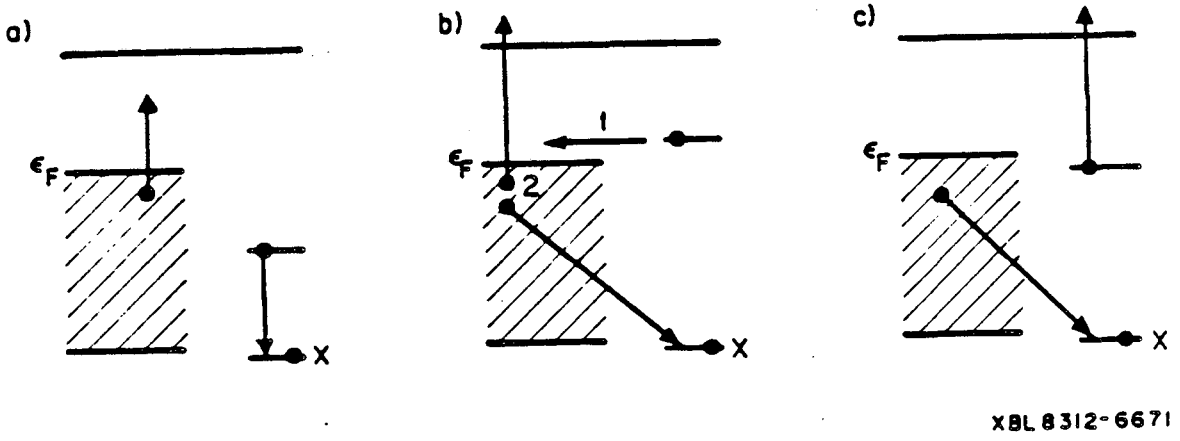

Figure 49. Energy decay mechanisms for an excited molecule near a metal surface. On the left of each part is shown the metal conduction band filled to the Fermi level ϵ_F, and on the right are two levels of an adsorbed molecule (the lower level X being the highest occupied level in the ground state). (a) Energy transfer by dipole coupling between the molecule and the metal, causing excitation of a metal electron-hole pair. (b) Resonant transfer (process 1) of an excited electron into an unfilled level of the metal conduction band. The resulting ion usually relaxes via Auger neutralization (process 2) where a metal electron fills the lower molecular level with ejection of a metal Auger electron. (c) For an excited state below the Fermi level, resonant transfer is inhibited and one step Auger deexcitation (Penning ionization) may take place.

for the first monolayer and 1.2×10^{-13} sec for the second layer. Comparing these values they find that the image formula overestimates the damping rate for the first layer by a factor of four and underestimates the damping of the second layer by a factor of four. Image dipole coupling thus appears to give a fairly good prediction of the surface lifetime, a perhaps fortuitous result of the infinity at d = 0 cancelling an underestimation of the decay rate very close to the surface due to non-inclusion of other decay channels. We will use the image formula, then, to obtain an order of magnitude estimate of energy transfer rates in the following discussion.

The dynamics of benzaldehyde surface photodecomposition from its lowest excited singlet state will now be examined in a calculation based on gas phase molecular properties and energy damping by dipole coupling to the surface. Radical formation occurs with a quantum yield of 0.4 in the gas phase, probably directly from the excited singlet since the addition of a triplet quencher does not affect the reaction.[198] The process must occur with a rate constant of at least 10^{12} sec^{-1}, the estimated intersystem crossing rate of benzaldehyde S_1.[209] The nonradiative relaxation of the excited state near a silver surface can be calculated using the image formula and the oscillator strength f = 0.00055[210] of the benzaldehyde S_1 excitation. The dielectric constant used for silver is $\epsilon_{Ag} = -0.59 + 0.90i$ determined ellipsometrically at 350 nm. The results, shown in Table 5, indicate that there may be substantial deactivation of the excited state on the timescale of the reaction for the first and possibly the second molecular layer. At distances of 10 Å or greater from the surface, though, the energy transfer rate appears to be much smaller

Table 5. Calculated surface lifetimes for benzaldehyde above a rough silver surface.

Distance from surface	τ_{nr} (energy transfer)
1.6 Å (1^{st} monolayer)	1.7×10^{-13} sec
5 Å	5.2×10^{-12} sec
10 Å	4.1×10^{-11} sec
20 Å	3.3×10^{-10} sec
30 Å	1.1×10^{-9} sec

than the reaction rate.

From the observed surface-molecule distance dependence of photodecomposition rate, it is clear that the distance dependence of enhanced photochemistry is quite different from that of surface Raman enhancement. Nitzan and Brus3 indicate that for the simple model of surface roughness as silver spheres the surface damping rate would be expected to decrease as d^{-3} (image dipole model) while the resonance induced local field enhancement would decrease as $(d + a)^{-3}$ where a is the sphere radius. Since the field enhancement will then decay more slowly as a function of separation than the surface damping, this model predicts a maximum in the photochemistry rate at some intermediate molecule-surface separation. Such an effect is seen in our studies where the pyridine photodecomposition rate is a maximum at a separation of 15-20 Å from the surface, as shown in Figure 48.

B. Decomposition Mechanism: Neutral or Ionic Pathway?

Most recent studies of molecule fragmentation in the gas phase have come from the rapidly expanding field of multiphoton ionization mass spectrometry. The general fragmentation process is usually interpreted in terms of three separate steps: (1) multiphoton excitation of the molecule to a resonant intermediate state, (2) ionization of the excited neutral molecule to the parent ion by absorption of another photon, and (3) fragmentation of the parent ion by absorption of one or more photons to yield a distribution of daughter ions.[211] The work of Boesl, Neusser, and Schlag[212] confirmed this for benzene by studying ionization and fragmentation patterns for light of different frequencies separated by time delays.

This is also the case for the multiphoton fragmentation of acetaldehyde where identical resonances in excitation wavelength were observed by monitoring parent and fragment ions.[213]

Recent multiphoton ionization-fragmentation studies of benzaldehyde[214] indicate that there is competition between two fragmentation pathways depending on the excited state manifold to which the molecule is excited. For excitation into S_2 with 266 nm light, competition is found to occur between multiphoton ionization of the parent molecule and dissociation into C_6H_6 and CO followed by multiphoton ionization of C_6H_6 which then fragments. Excitation into S_1 with 355 nm photons yields decomposition only by the first channel - ionization of the parent molecule followed by fragmentation. Thus from these experiments one must conclude that benzaldehyde apparently follows the same trend observed for many other molecules of parent molecule ionization with subsequent fragmentation.

Whetten et al.[215] have also recently studied multiphoton fragmentation of benzaldehyde. Their experiments consisted of measurements of total and fragment ion signal from a number of molecules as the wavelength was varied in the range of 275-295 nm. Results for benzaldehyde were a spectrum consisting largely of carbon atom two photon resonance ionization peaks. Analysis of the C+/total ion signal for benzaldehyde showed that more than eight times the background total ion signal is found at the carbon atom resonance lines. Thus at least part of the carbon atoms formed in this study must be produced by entirely neutral pathways. This surprising result is not inconsistent with the previously discussed data on multiphoton ionization-fragmentation of benzaldehyde, however, since

carbon neutrals could have been present in those experiments which were not ionized at the particular laser frequencies used and thus were not detected.

It appears from these results and the previously cited gas phase photochemical studies of benzaldehyde[190,191] that neutral decomposition from higher excited singlet states of benzaldehyde is a fairly efficient process, and that subsequent photon absorption to produce ionized molecules and fragments is not necessary to explain the observed fragmentation. Indeed, Antonov et al.[195] report that the benzaldehyde photoionization cross section is approximately two orders of magnitude lower than that observed for benzene at the wavelengths they have studied. In our experiments benzene does not decompose to any extent while benzaldehyde fragments readily. Thus we believe that photoionization is probably not an important mechanism in benzaldehyde fragmentation on silver surfaces.

For other molecules, however, the choice of fragmentation pathway is not as clear. For surface experiments, the resonant state in multiphoton absorption will have a greatly decreased lifetime due to energy transfer to the surface, except possibly in those cases where a two photon resonant state is not strongly dipole coupled to the ground state. In view of this, it becomes attractive to postulate excitation into an ionic continuum from which fragmentation or further absorption could occur. There is some recent evidence that ion formation by multiphoton absorption on metal surfaces may be a more favorable process than ionization in the gas phase.[216] Ion formation on the surface might be aided by direct excitation of molecular valence electrons into unoccupied metal orbitals above the

Fermi level as suggested by the observation of charge-transfer excitations for some molecules on silver.[171] At present we have no evidence for the presence of ionic intermediates in the fragmentation of aromatic molecules on silver. Experiments are currently underway to determine whether these intermediates can exist in the fragmentation pathway on rough silver.

V. Conclusion

During this investigation we have established that a variety of aromatic molecules undergo resonant absorption and decomposition on a rough silver surface. For two molecules studied (pyridine and benzaldehyde) laser power dependence studies with 406.7 nm light indicate that the absorption step is a two photon process. Energetic considerations make it likely that absorption by the other molecules studied is also a multiphoton process, except for benzaldehyde with 350.7 nm irradiation where photochemistry apparently occurs directly from the first excited singlet state following a one photon absorption.

The decomposition reaction pathway to surface carbon most likely occurs by a neutral pathway for benzaldehyde, since gas phase photochemistry takes place via radical formation and neutral fragmentation all the way to carbon atoms has been observed in multiphoton absorption experiments. Further study is necessary to determine whether rapid ionization preceding fragmentation as observed in most multiphoton fragmentation experiments in gases is a likely pathway for surface reactions of other molecules.

We have observed the presence of intermediate species in surface photofragmentation reactions using Raman spectroscopy. A CN stretching mode is seen in the Raman spectrum of pyridine and pyrazine during decomposition. The frequency of this mode is shifted substantially from that usually observed for CN adsorbed on silver, however, indicating that a larger fragment such as C_3H_3N (observed in gas phase multiphoton fragmentation of these molecules) may be the actual surface species observed. No additional Raman bands that could be assigned to surface intermediates were seen in the photofragmentation of benzaldehyde, but different Raman shifts for the surface carbon formed were observed for decomposition at different wavelengths. Hence different carbon structures may be formed by decomposition following absorption by a one or a two photon process.

Finally, studies of the distance dependence of decomposition rate by the use of spacer molecules shows a maximum decomposition rate at a separation of 15-20 Å from the surface. The surface distance dependence of Raman enhancement is markedly different, exhibiting a sharply peaked enhancement for the first adsorbed layer and a much smaller enhancement for several subsequent layers. This behavior is consistent with that predicted for an enhanced surface photochemical process where the different distance dependencies of damping by energy transfer to surface modes competes with enhanced energy absorption, resulting in a peak photochemical rate at some distance from the metal surface.

References

1. U. Fano and J.A. Stephens, Phys. Rev. B, 34, 438 (1986).

2. J. Schnitker, P.J. Rossky and G.A. Kenney-Wallace, J. CHem. Phys., 85, 2986 (1986); A. Wallqvist, D. Thirumalai and B.J. Berne, J. Chem. Phys., 85, 1583 (1986); M. Knapp, O. Echt, D. Kreisle and E. Recknagel, J. Chem. Phys., 85, 636 (1986).

3. Y.C. Chang and W.B. Berry, J. Chem. Phys., 61, 2727 (1974).

4. J.J. Huang and J.L. Magee, J. Chem. Phys., 61, 2736 (1974).

5. J. Holzl, and F.K. Schulte, in Solid Surface Physics, Springer Tracts in Modern Physics v. 85, ed. G. Hohler (Springer-Verlag, Berlin, 1979) p.1.

6. K. Hiraoka and W.H. Hamill, J. Chem. Phys., 56, 3185 (1972).

7. L. Sanche, J. Chem. Phys., 71, 4860 (1979).

8. K. Hiraoka and W.H. Hamill, J. Chem. Phys., 57, 3870 (1972).

9. I. Cheng and K. Funabashi, J. Chem. Phys., 59, 2977 (1973).

10. K. Hiraoka and M. Nara, Bull. Chem. Soc. Jpn., 54, 1589 (1981).

11. L. Sanche, G. Bader and L. Caron, J. Chem. Phys., 76, 4016 (1982).

12. K. Hiraoka, J. Phys. Chem., 85, 4008 (1981).

13. L.G. Caron and G. Bader, J. Chem. Phys., 80, 119 (1984).

14. K. Hiraoka and M. Nara, Bull. Chem. Soc. Jpn., 57, 2243 (1984).

15. K.D. Jordan and P.D. Burrow, Acc. Chem. Res., 11, 341 (1978).

16. M.H. Cohen and J. Lekner, Phys. Rev., 158, 305 (1967).

17. G. Perluzzo, L. Sanche, C. Gaubert and R. Baudoing, Phys. Rev. B, 4292 (1984).

18. P.J. Chantry, A.V. Phelps and G.J. Schulz, Phys. Rev., 152, 81 (1966).

19. G. Bader, G. Perluzzo, L.G. Caron and L. Sanche, Phys. Rev. B, 26, 6019 (1982).

20. B. Plenkiewicz, P. Plenkiewicz and J.-P. Jay-Gerin, Phys. Rev. B, 33, 5744 (1986).

21. T. Goulet and J.P. Jay-Gerin, Sol. St. Comm., 55, 619 (1985).

22. W. Pong and J.A. Smith, J. Appl. Phys., 44, 174 (1973).

23. P. Nielson, D.J. Sandman and A.J. Epstein, Sol. St. Comm., 17, 1067 (1975).

24. S.F. Lin, W.E. Spicer and B.H. Schechtman, Phys. Rev. B, 12, 4184 (1975).

25. S. Hino, N. Sato and H. Inokuchi, J. Chem. Phys., 67, 4139 (1977).

26. J.J. Ritsko, P. Nielson and J.S. Miller, J. Chem. Phys., 67, 687 (1977).

27. P. Pfluger, H.R. Zeller and J. Bernasconi, Phys. Rev. Lett., 53, 94 (1984).

28. V.V. Grechov, Chem. Phys. Lett., 96, 237 (1983).

29. S. Hino and H. Inokuchi, J. Chem. Phys., 70, 1142 (1979).

30. F. Gutman and L.E. Lyons, Organic Semiconductors, part A (Kreiger, Maladar, 1981) chp. 1.

31. R. Lesclaux and J. Joussot-Dubien, in Organic Molecular Photophysics, vol. 1, edited by J.B. Birks (Wiley, New York) p. 457.

32. J. Jortner, J. Chem. Phys., 30, 839 (1959).

33. J.L. Dye, Prog. Inorg. Chem., 32, 327 (1984).

34. K. Fueki, D.F. Feng and L. Kevan, J. Chem. Phys., 56, 5351 (1972).

35. K. Funabashi, I. Carmichael and W.H. Hamill, J. Chem. Phys., 69, 2652 (1978)., G.L. Hug and I. Carmichael, J. Phys. Chem., 86, 3410 (1982).

36. L. Kevan, Acc. Chem. Res., 14, 138 (1981).

37. R.M. Minday, L.D. Schmidt and H.T. Davis, J. Chem. Phys., 54, 3112 (1971).

38. K. Funabashi and T. Kajiwara, J. Phys. Chem., 76, 2726 (1972).

39. J.E. Willard, J. Phys. Chem., 79, 2966 (1975).

40. W.F. Schmidt, Can. J. Chem., 55, 2198 (1977).

41. A.A. Balakin and B.S. Yakovlev, Chem. Phys. Lett., 66, 299 (1979).

42. P. Krebs and M. Heintze, J. Chem. Phys., 76, 5484 (1982).

43. J.R. Miller, J. Phys. Chem., 79, 1070 (1975).

44. W.H. Hamill and K. Funabashi, Phys. Rev. B, 16, 5523 (1977).

45. A.C. Albrecht, Acc. Chem. Res., 3, 238 (1969).

46. E.M. Pugh and E.W. Pugh, Principles of Electricity and Magnetism, 2nd ed. (Addison-Wesley, Reading, MA, 1970) p. 178.

47. M.W. Cole and M.H. Cohen, Phys. Rev. Lett., 23, 1238 (1969).

48. C.C. Grimes and T.R. Brown, Phys. Rev. Lett., 32, 280 (1974).

49. P.M. Echnique and J.B. Pendry, J. Phys. C, 11, 2065 (1978).

50. D. Straub and F.J. Himpsel, Phys. Rev. Lett., 52, 1922 (1984).

51. S.L. Hulbert, P.D. Johnson, N.G. Stoffel, W.A. Royer and N.V. Smith, Phys. Rev. B, 31, 6815 (1985).

52. P.M. Echenique, F. Flores and F. Sols, Phys. Rev. Lett., 55, 2348 (1985).

53. J. Bausells, P.M. Echenique, Phys. Rev. B, 33, 1471 (1986).

54. S.N. Anisimov, A.I. Bolozdynya and V.N. Stekhanov, JETP Lett., 40, 829 (1984).

55. P.R. Antoniewicz, G.T. Bennett and J.C. Thompson, J. Chem. Phys., 77, 4573 (1982).

56. M.R. Belmont, Thin Solid Films, 22, 281 (1974).; 28, 149 (1975); 60, 341 (1979).

57. N.D. Lang, W. Kohn, Phys. Rev. B, 3, 1215 (1971).

58. J.D. Jackson, Electromagnetism, 2nd ed. (John Wiley, New York 1975) p. 36.

59. A. Kiejna, K.J. Wojciechowski, in Progress in Surface Science v.11, ed. S.G. Davison (Pergamon, New York, 1981) p. 293.

60. C. Herring and M.H. Nichols, Rev. Mod. Phys., 21, 185 (1949).

61. J.R. McDonald, and C.A. Barlow, J. Chem. Phys., 39, 412 (1963).

62. J. Topping, Proc. Roy. Soc. (London), A114, 67 (1927).

63. J.R. McDonald and C.A. Barlow, Surf. Sci., 4, 381 (1966); J. Chem. Phys., 44, 202 (1966).

64. L.D. Schmidt and R. Gomer, J. Chem. Phys., 45, 1605 (1966).

65. Z. Sidorski, I. Pelly, R. Gomer, J. Chem. Phys., 50, 2382 (1969).

66. C. Wang and R. Gomer, Surf. Sci., 91, 533 (1980).

67. P.W. Palmberg, Surf. Sci., 25, 598 (1971).

68. J.L. Taylor, D.E. Ibbotson and W.H. Weinberg, J. Chem. Phys., 69, 4298 (1978).

69. J.M. Heras and E.V. Albano, Appl. Surf. Sci., 7, 332 (1981).

70. A.M. Bradshaw and M. Scheffler, J. Vac. Sci. Tech., 16, 447 (1979).

71. P.R. Antoniewicz, Phys. Stat. Sol. B, 86, 645 (1978).

72. J. Mulliken, J. Am. Chem. Soc., 74, 811 (1952).

64. J.C.P. Mignolet, Disc. Faraday Soc., 8, 105 (1950).

74. B.E. Nieuwenhuys, O.G. van Aardenne and W.M.H. Sachtler, Chem. Phys., 5, 418 (1974).

75. C. Mavoryannis, Mol. Phys., 6, 593 (1963).

76. P.M. Gundry and F.C. Tompkins, Trans. Faraday Soc., 56, 846 (1960).

77. R.W. Gurney, Phys. Rev., 47, 479 (1935).

78. J.P. Muscat and D.M. Newns, J. Phys. C, 7, 2630 (1974).

79. N.D. Lang, Phys. Rev B, 4, 4234 (1971).

80. N.D. Lang and W. Kohn, Phys. Rev. B, 1, 4555 (1970).

81. H. Yamauchi and U. Kawabe, Phys. Rev B, 14, 2687 (1976).

82. E. Wimmer, A.J. Freeman, J.R. Hiskes and A.M. Karo, Phys. Rev. B, 24, 864 (1981).

83. E. Wimmer, H. Krakauer, M. Weinert and A.J. Freeman, Phys. Rev. B, 24, 864 (1981); H. Krakauer, M. Posternak and A.J. Freeman, Phys. Rev. B, 19, 1706 (1979).

84. W. Ning, C. Kailai, W. Dingsheng, Phys. Rev. Lett., 56, 2759 (1986).

85. E. Shustorovich, Sol. St. Comm., 38, 493 (1981); E. Shustorovich and R.C. Baetzold, Appl. Surf. Sci., 11/12, 693 (1982); R.C. Baetzold, J. Phys. Chem., 87, 3858 (1983).

86. J.C.P. Mignolet, Disc. Faraday Soc., 8, 105 (1950).

87. G.C. Smith, H.A. Padmore and C. Norris, Surf. Sci., 119, L287 (1982).

88. R.J. Behm, C.R. Brundle and K. Wandelt, J. Chem. Phys., 85, 1061 (1986).

89. T. Engel and R. Gomer, J. Chem. Phys., 52, 5572 (1970).

90. B.E. Nieuwenhuys, R. Bouwman and W.M.H. Sachtler, Thin Solid Films, 21, 51 (1974).

91. G. McElhiney, H. Papp and J. Pritchard, Surf. Sci., 54, 617 (1976).

92. A.G. Knapp and M.H.B. Stiddard, J. Chem. Soc. Faraday Trans. I, 68, 2139 (1972).

93. M. Abon, J. Billy, J.C. Bertolini and B. Tardy, Surf. Sci., 171, L387 (1986).

94. S.R. Kelemen and T.E. Fischer, Surf. Sci., 102, 45 (1981).

95. E. Schmiedl, P. Wissmann and E. Wittmann, Surf. Sci., 135, 341 (1983).

96. M. Abon, J. Billy, J.C. Bertolini and B. Tardy, Surf. Sci., 167 L187 (1986).

97. F.P. Netzer and J.U. Mack, Chem. Phys. Lett., 95, 492 (1983).

98. E.V. Albano, S. Daiser, R. Miranda and K. Wandelt, Surf. Sci., 150, 386 (1985).

99. G. Ertl, M. Neumann and K.M. Streit, Surf. Sci., 64, 393 (1977); P.R. Norton, J.W. Goodale and E.B. Selkirk, Surf. Sci., 83, 189 (1979).

100. P. Lange, D. Grider, H. Neff, J.K. Sass and R. Unwin, Surf. Sci., 118, L257 (1982).

101. M.P. Cox, J.S. Foord and R.M. Lambert, Surf. Sci., 129, 375 (1983).

102. R. Gomer, J. Chem. Phys., 29, 441 (1958); 443 (1958).

103. R. Gomer, J. Phys. Chem., 63, 468 (1959).

104. R. Gomer, Aust. J. Phys., 13, 391 (1960).

105. J.L. Gland and G.A. Somorjai, Surf. Sci., 41, 387 (1974).

106. G.L. Eesley, Phys. Lett., 81A, 193 (1981).

107. G.M. Goncher, C.A. Parsons, C.B. Harris, J. Phys. Chem., 88, 4200 (1984).

108. J.H. Bechtel, J. Appl. Phys., 46, 1585 (1975).

109. L.E. Firment and G.A. Somorjai, J. Chem. Phys., 66, 2901 (1977).

110. M. Chelvayohan and C.H.B. Mee, J. Phys. C, 15, 2305 (1982).

111. S.N. Levine, Quantum Physics of Electronics, (Macmillan, 1965) p. 137.

112. C.T.Aw, H.H. Huang, and E.L.K. Tan, J. Chem. Soc., Perkin Trans. II, 11, 163 (1970). T. Abe, Bull. Chem. Soc. Jpn., 40, 1571 (1967).

113. S.R. Kelemen, A. Kaldor, Chem. Phys. Lett., 73, 205 (1980).

114. A.A. Maryott, and E.R. Smith, Table of Dielectric Constants of Pure Liquids, NBS Circular 514 (1951).

115. C.N. Berglund and W.E. Spicer, Phys. Rev., 136, A1044 (1964).

116. J.E. Demuth, K. Christmann and P.N. Sanda, Chem. Phys. Lett., 76, 201 (1980).

117. F. Mulder and G. Van Dijk, Mol. Phys., 38, 577 (1979).

118. J.E. Demuth and P.N. Sanda, Phys. Rev. Lett., 47, 57 (1981).

119. R. Li and E.C. Lim, J. Chem. Phys., 57, 605 (1972).

120. K. Sushida, M. Fujita, T. Takemura and H. Baba, J. Chem. Phys., 78, 588 (1983).

121. S. Gartenhaus, Physics: Basic Principles v.II (Holt, Rinehart and Winston, New York, 1975) p. 685.

122. R. Becker, Electromagnetic Fields and Interactions (Dover, and Blaisdell Publishing Co., New York, 1964) p. 75.

123. J.D. Jackson, private communication.

124. J.K. Brown, private communication.

125. G.E. Forsythe, M.A. Malcolm and C.B. Moler, Computer Methods for Mathematical Computations (Prentice-Hall, Englewood Cliffs, NJ, 1977) p. 129.

126. L. Onsager, Phys. Rev., 54, 554 (1938).

127. For example see K.M. Hong and J. Noolandi, J. Chem. Phys., 68, 5163 (1978); 69, 5026 (1978).

128. M. Eichorn, F. Willig, K.-P. Charle and K. Bitterling, J. Chem. Phys., 76, 4648 (1982).

129. K.-P. Charle and F. Wittig, Chem. Phys. Lett., 57, 253 (1978).

130. T.W. Scott, J. Phys. Chem., 90, 1739 (1986).

131. D.L. Dexter, J. Lumin., 18/19, 779 (1979).

132. Extended Abstracts: Laser Chemical Processing of Semiconductor Devices, ed. F.A. Houle, T.F. Deutsch and R.M. Osgood, Jr., (Materials Research Society, Boston, 1984).

133. P.M. Whitmore, H.J. Robota and C.B. Harris, J. Chem. Phys., 77, 1560 (1982).

134. P.M. Whitmore, A.P Alivisatos and C.B. Harris, Phys. Rev. Lett., 50, 1092 (1983).

135. R.R. Chance, A. Prock and R. Silbey, Adv. Chem. Phys., 37, 1, S.A. Rice and I. Prigogine, eds. (Wiley-Interscience, New York, 1978).

136. J.E. Demuth and P.N. Sanda, Phys. Rev. Lett., 47, 57 (1981); Ph. Avouris and J.E. Demuth, J. Chem. Phys., 75, 4783 (1981); N.J. DiNardo, Ph. Avouris and J.E. Demuth, J. Chem. Phys., 81, 2169 (1984); Ph. Avouris and J.E. Demuth, Surf. Sci., 158, 21 (1985).

137. H.J. Robota, P.M. Whitmore and C.B. Harris, J. Chem. Phys., 76, (1982).

138. W. Dietsche, Th. Rapp and H.C. Basso, J. Appl. Phys., 59, 1431 (1986).

139. A.P. Alivisatos, Ph.D. thesis, Univ. of California, (1986).

140. UV Atlas of Organic Compounds Vol III, (Plenum Press, New York, 1967) p. E4/2.

141. R. Jankowiak, K.D. Rockwitz and H. Bassler, J. Phys. Chem., 87, 552 (1983).

142. D.E. Aspnes and A.A. Studna, Appl. Phys. Lett., 39, 316 (1981).

143. H.J. Robota, Ph.D. thesis, Univ. Ca. Berkeley (1982).

144. A. Bree and L.E. Lyons, J. Chem. Soc., 5206 (1960).

145. R. Eiermann, G.M. Parkinson, H. Bassler and J.M. Thomas, J. Phys. Chem., 85, 313 (1982).

146. E. Hertel and H.W. Bergk, Z. Phys. Chem., 33 B, 319 (1936).

147. J.A. Katul and A.B. Zahlan, J. Chem. Phys., 47, 1012 (1967).

148. G. Fournie, F. Dupuy, M. Martinaud, G. Nouchi and J.M. Turlet, Chem. Phys. Lett., 16, 332 (1972).

149. M. Martinaud and Ph. Kottis, J. Phys. Chem., 82, 1497 (1978).

150. H.E. Hallam, Vibrational Spectroscopy of Trapped Species, (Wiley Interscience, London, 1973) p.56.

151. J.W. Sidman, J. Chem. Phys., 25, 122 (1956).

152. A. Amirav, U. Even and J. Jortner, J. Chem. Phys., 75, 3770 (1981).

153. T. Sakurai and S. Hayakawa, Jap. J. Appl. Phys., 13, 1733 (1974).

154. B.E.Koel, J.M.White, J.L.Erskine, and P.R.Antoniewicz, in Interfacial Photoprocesses: Energy conversion and Synthesis, ed. M.S.Wrighton (ACS, Washington, D.C., 1980) p.27.

155. T.J.Chuang, Surf.Sci.Reports 3, 1 (1983).

156. A.Nitzan and L.E.Brus, J.Chem.Phys. 75, 2205 (1981).

157. G.M.Goncher and C.B.Harris, J.Chem.Phys., 77, 3767 (1982).

158. S.Garoff, D.A.Weitz, and M.S.Alvarez, Chem.Phys.Lett. 93, 283 (1982).

159. C.J.Chen and R.M.Osgood, Phys.Rev.Lett. 50, 1705 (1983) and Appl.Phys. A 31, 171 (1983).

160. J.Gersten and A.Nitzan, J.Chem.Phys. 73, 3023 (1980) and J.Chem.Phys. 75, 1139 (1981).

161. C.K.Chen, A.R.B.deCastro, and Y.R.Shen, Phys.Rev.Lett. 46, 145 (1981).

162. H.J.Robota, P.M.Whitmore, and C.B.Harris, J.Chem.Phys. 76, 1692 (1982).

163. E.Kretschman, T.A.Callcott, and E.T.Arakawa, Surf.Sci. 91, 237 (1980).

164. R.M.A.Azzam and N.M.Bashara, Ellipsometry and Polarized Light (NorthHolland, New York, 1977) p.361.

165. B.J.Messinger, K.U.von Raben, R.K.Chang, and P.W.Barber, Phys.Rev.B 24, 649 (1981).

166. I.Pockrand and A.Otto, Appl.Surf.Sci., 6, 362 (1980).

167. J.C.Tsang, J.E.Demuth, P.N.Sanda, and J.R.Kirtley, Chem.Phys.Lett. 76, 54 (1980).

168. N.Wada, P.J.Gaczi, and S.A.Solin, J.Non-Cryst.Solids 35, 543 (1980).

169. S.S.Kelemen and I.E.Wachs, Surf.Sci. 97, L370 (1980).

170. J.E.Rowe, C.V.Shank, D.A.Zwemer, and C.A.Murray, Phys.Rev.Lett. 44, 1770 (1980).

171. Ph.Avouris and J.E.Demuth, J.Chem.Phys. 75, 2205 (1981).

172. T.F.Heinz, C.K.Chen, D.Ricard, and Y.R.Shen, Chem.Phys.Lett. 83, 180 (1981).

173. C.K.Chen, T.F.Heinz, D.Ricard, and Y.R.Shen, Phys.Rev. B 27, 1965 (1983).

174. A.M.Glass, A.Wokaun, J.P.Heritage, J.E.Bergman, P.F.Liao, and D.F.Olson, Phys.Rev. B 24, 4906 (1981).

175. K.K.Innes, J.P.Byrne, and I.G.Ross, J.Mol.Spectr. 22, 125 (1967).

176. P.Esherick, P.Zinsli, and M.A.El-Sayed, Chem.Phys. 10, 415 (1975).

177. J.D.Webb, K.M.Swift, and E.R.Bernstein, J.Mol.Struct. 61, 285 (1980).

178. R.E.Turner, V.Vaida, C.A.Molini, J.O.Berg, and D.H.Parker, Chem.Phys. 28, 47 (1978).

179. J.O. Berg, D.H. Parker, and M.A. El-Sayed, Chem. Phys. Lett., 56, 28, 47 (1978).

180. M.B.Robin, Higher Excited States of Polyatomic Molecules, vol.1 (Academic Press, New York, 1975) ch. II.C.

181. M.Hackmeyer and J.L.Whitten, J.Chem.Phys. 54, 3739 (1971).

182. W.R.Eadt, W.A.Goddard III, and T.H.Dunning,Jr., J.Chem.Phys. 65, 438 (1976).

183. R.H.Linnel and W.A.Noyes,Jr., J.Am.Chem.Soc. 73, 3986 (1951).

184. E.Mathias and J.Heiklen, Mol.Photochem. 4, 483 (1972).

185. J.Billman, G.Kovacs, and A.Otto, Surf.Sci. 92, 153 (1980).

186. H.D.Eland and J.Berkowitz, Int.J.Mass Spectrom.Ion Phys. 28, 297 (1978).

187. M.Seaver, J.W.Hudgens, and J.J.DeCorpo, Int.J.Mass Spectrom.Ion Phys. 34, 159 (1980).

188. B.-O.Jonsson, E.Lindholm, and A.Skerbele, Int.J.Mass Spectrom.Ion Phys. 3, 385 (1969).

189. R.Shimada and L.Goodman, J.Chem.Phys. 43, 2027 (1965).

190. M.Berger,I.L.Goldblatt, and C.Steel, J.Am.Chem.Soc. 95, 1717 (1973).

191. M.B. Robin and N.A. Kuebler, J. Am. Chem. Soc., 97, 4822 (1975).

192. M.Berger and C.Steel, J.Am.Chem.Soc. 97, 4817 (1975).

193. F.Tuinstra and J.L.Koenig, J.Chem.Phys. 53, 1126 (1970).

194. N.J.Turro, Modern Molecular Photochemistry (Benjamin/Cummings, Menlo Park, 1978) ch. 11,12.

195. V.S.Antonov, V.S.Letokhov, and A.N.Shibanov, Appl.Phys. 22, 293 (1980). P.M.Johnson, J.Chem.Phys. 64, 4143 (1976). H.Kuhlewind, H.J.Neusser, and E.W.Schlag, Int.J.Mass Spectrom. Ion. Phys., 51, 255 (1983). K.R.Newton and R.B.Bernstein, J.Phys.Chem. 87, 2246 (1983).

196. T.W.Scott, C.L.Braun, and A.C.Albrecht, J.Chem.Phys. 76, 5195 (1982).

197. L.Zandee and R.B.Bernstein, J.Chem.Phys. 70, 2574 (1979).

198. A.Berthelon, P.Meallier, and B.Pouyet, J.Chim.Phys. 72, 8 (1975).

199. C.T.Rettner and J.H.Brophy, Chem.Phys. 56, 53 (1981).

200. U.Boesl, H.J.Neusser, and E.W.Schlag, Chem.Phys. 55, 193 (1981).

201. T.J.Chuang and H.Seki, Phys.Rev.Lett. 49, 382 (1982).

202. P.M.Whitmore, H.J.Robota, and C.B.Harris, J.Chem.Phys. 76, 740 (1982).

203. J.Gersten and A.Nitzan, J.Chem.Phys. 75, 1139 (1981).

204. R.Ruppin, J.Chem.Phys. 76, 1681 (1982).

205. J.Arias, P.K.Aravind, and H.Metiu, Chem.Phys.Lett. 85, 404 (1982).

206. Ph.Avouris, D.Schmeisser, and J.E.Demuth, J.Chem.Phys. 79, 488 (1983).

207. H.D.Hagstrum, Phys.Rev. 96, 336 (1954).

208. B.N.J.Persson and Ph.Avouris, J.Chem.Phys. 79, 5156 (1983).

209. Y.Hirata and E.C.Lim, J.Chem.Phys. 72, 5505 (1980).

210. K.Inuzuka and T.Yokota, Bull.Chem.Soc.Jap. 38, 1055 (1965).

211. R.B.Bernstein, J.Phys.Chem. 86, 1178 (1982).

212. U.Boesl, H.J.Neusser, and E.W.Schlag, J.Chem.Phys. 72, 4327 (1980).

213. G.J.Fisanick, T.S.Eichelberger, B.A.Heath, and M.B.Robin, J.Chem.Phys. 72, 5571 (1980).

214. J.J.Yang, D.A.Gobell, R.S.Pandolfi, and M.A.El-Sayed, J.Phys.Chem. 87., 2255 (1983).

215. R.L.Whetten, K.-J.Fu, R.S.Tapper, and E.R.Grant, J.Phys.Chem. 87, 1484 (1983).

216. R.B.Opsal and J.P.Reilly, Chem.Phys.Lett. 99, 461 (1983).

Appendix. Fortran Programs

Program 1. Electron trajectories near a dielectric-covered surface

```
c Calculates the image trajectory of an electron a distance d from a
c dielectric coated (dielec. const. =e, thickness =th) conductor
c interface.  The solution was provided by J.D. Jackson, and is
c different for d>th, and d<th.  Each case involves an infinite
c integral which is evaluated by integrall.  The x(distance) vs t
c integration is done by integral2 using the energy conservation
c equation.  All integrations are performed with a 24th order
c quadature technique provided by J.K. Brown using weighting factors
c in file wa.

      program fourord
      real*8 m,et,ke,pe,x0,v0,value,rat,vel
      real*8 b,f,th,e,eti,t,xm,d,x2,t2,x1,ped
      double precision abc(24),wgt(24)
      integer  i,j
      common/arr/ abc,wgt
      common/var/ m,f,x0,b,eti,e,th,pe,vel
      m=9.11d-31
      b=2.307d-28
      write(6,15)
   15 format(' input th,e,x0,v0,f :')
      read(5,25) th,e,x0,v0,f
   25 format(5d15.8)
      write(6,25)th,e,x0,v0,f
      t=0.d0
      open(1,file='wa',status='old')
      do 100 i=1,24
  100 read(1,*) abc(i),wgt(i)
      close (1)
      call integrall(x0,value)
   50 eti=0.5d0*m*v0**2 - b*(1.d0/(2.d0*x0) + 2.d0*(e-1.d0)*value)
      x2=x0
      do 60 i=-1,9
      xm=x0*1.d1**(i-1)
      do 60 j=1,9
      x1=x2
      x2=x0+xm*j
c     write(6,*)x1,x2
      call integral2(x1,x2,t2,i+2)
      t=t+t2
      ke=.5d0*m*vel**2
      if (e .ne. 1.d0) go to 52
      value=1.d0
      go to 53
   52 call integrall(x2,value)
   53 ped=-b*(1.d0/(2.d0*x2) + 2.d0*(e-1.d0)*value)
      pe=ped - f*(x2-x0)
      et=pe+ke
```

Program 1, continued

```
        if (x2 .eq. x0) go to 45
c       write(6,*)pe,f*(x2-x0),x2,x0
        rat=dabs(ped/(f*(x2-x0)))
   45   write(6,35)t,x2,rat,ke,et,dlog10(t),dlog10(x2)
   35   format(' time=',e13.6,5x,' x=',e13.6,5x,'f(im)/f(g)=',e13.6,/
     +  '   ke=',e13.6,5x,'et=',e13.6/'lgt=',e13.6,5x,'lgx=',e13.6/)
        if (t2 .eq. 0.d0)go to 70
   60   continue
        stop
   70   write(6,80)
   80   format('electron captured by surface')
        stop
        end

        subroutine integral1(d,tsum)
c       implicit double precision(a-h,o-z)
        double precision sum,xmin,xmax,xlmax,xlmin,tsum,stp,vel
        double precision abcis(24),weight(24),abc(24),wgt(24)
        double precision func1,func2
        real*8 m,et,pe,ke,x0,eti
        real*8 d,b,f,th,e
        integer i,j
        common/var/ m,f,x0,b,eti,e,th,pe,vel
        common/arr/ abc,wgt
c       write(6,10)d
   10   format('evaluate integral 1',d15.8)
        stp=1.d0/d
        tsum=0.d0
        xlmax=0.d0
        xlmin=0.d0
        do 30 j=1,10000
        xlmin=xlmax
        xlmax=xlmax+stp
        call d01bcf(xlmin,xlmax,weight,abcis,abc,wgt)
        sum=0.d0
        do 200 i=1,24
        if (d .ge. th) go to 25
        sum=sum+weight(i)*func2(abcis(i),d)
        go to 200
   25   sum=sum+weight(i)*func1(abcis(i),d)
  200   continue
        tsum= tsum + sum
        if (sum/tsum .gt. 1.d-6) go to 30
c       write(6,32)j,xlmax,tsum,sum
        return
   30   continue
   32   format(x,i6,x,'xmax',d15.8,2x'infinite integral=',2d15.8)
        write(6,45)
   45   format('no convergence for infinite int.')
        return
        end
```

Program 1. continued

```
      double precision function func1(x,d)
c     implicit double precision(a-h,o-z)
      double precision x,d,th,e,m,f,x0,b,eti,pe,vel
      common/var/ m,f,x0,b,eti,e,th,pe,vel
      func1=dexp(-x*(2.d0*d-th))*dsinh(x*th)/(e+dtanh(x*th))
      return
      end

      double precision function func2(x,d)
c     implicit double precision(a-h,o-z)
      double precision x,d,th,m,f,x0,eti,e,b,pe,vel
      common/var/ m,f,x0,b,eti,e,th,pe,vel
      func2=dexp(-x*d)*dsinh(x*d)/(e+dtanh(x*th))
      return
      end

      subroutine d01bcf(a,b,weight,abcis,abc,wgt)
      double precision weight(24),abcis(24),a,b
      real*8 abc(24),wgt(24)
      double precision d,e
      integer i
      d=(b-a)/2.d0
      e=(a+b)/2.d0
      do 100 i=1,24
      abcis(i)=d*abc(i)+e
100   weight(i)=wgt(i)*d
      return
      end

      subroutine integral2(xmin,xmax,tsum,int)
c     implicit double precision(a-h,o-z)
      double precision sum,xmin,xmax,xlmax,xlmin,tsum,vel
      double precision abcis(24),weight(24),abc(24),wgt(24),stp
      double precision func
      real*8 m,eti,pe,ke,value,x0
      real*8 b,f,th,e
      integer i,j,k,int
      common/var/ m,f,x0,b,eti,e,th,pe,vel
      common/arr/abc,wgt
c     write(6,10)
   10 format(/'evaluate integral 2'/)
      stp=(xmax-xmin)/5.d0
      tsum=0.d0
      xlmax=xmin
      do 30 j=1,5
      xlmin=xlmax
      xlmax=xlmax+stp
      call d01bcf(xlmin,xlmax,weight,abcis,abc,wgt)
c     write(6,*)xlmin,xlmax,(abcis(k),k=1,24)
      sum=0.d0
      do 200 i=1,24
c     write(6,*)j,i
```

Program 1. continued

```
        if (e .ne. 1.d0) go to 24
        value=1.d0
        go to 25
   24   call integrall(abcis(i),value)
   25   sum=sum+weight(i)*func(abcis(i),value)
c       write(6,40)sum,abcis(i)
  200   continue
   30   tsum= tsum + sum
c  30   write(6,40) tsum,xlmax
   40   format(10x'time=',d15.8,5x,'x=',d15.8)
        return
        end

        double precision function func(d,value)
c       implicit double precision(a-h,o-z)
        double precision d,th,e,value,m,f,x0,b,eti,pe,vel,diff
        common/var/ m,f,x0,b,eti,e,th,pe,vel
   5    pe=-b*(1.d0/(2.d0*d) + 2.d0*(e-1.d0)*value)-f*(d-x0)
        diff=eti-pe
        if (diff .ge. 0.) go to 10
        write(6,*)'sqrt of neg number  ',diff
   10   func=1.d0/dsqrt((2.d0/m)*diff)
        vel=1.d0/func
        return
        end
```

Program 1. file 'wa'

```
-0.9951872199970214      1.2341229799987246E-02
-0.9747285559713095      2.8531388628933663E-02
-0.9382745520027328      4.4277438817419818E-02
-0.8864155270044010      5.9298584915436789E-02
-0.8200019859739029      7.3346481411080309E-02
-0.7401241915785544      8.6190161531953274E-02
-0.6480936519369756      9.7618652104113890E-02
-0.5454214713888395      0.1074442701159656
-0.4337935076260453      0.1155056680537256
-0.3150426796961635      0.1216704729278034
-0.1911188674736165      0.1258374563468283
-6.4056892862605998E-02  0.1279381953467521
 6.4056892862605274E-02  0.1279381953467522
 0.1911188674736160      0.1258374563468283
 0.3150426796961630      0.1216704729278034
 0.4337935076260448      0.1155056680537256
 0.5454214713888391      0.1074442701159657
 0.6480936519369751      9.7618652104113987E-02
 0.7401241915785539      8.6190161531953413E-02
 0.8200019859739024      7.3346481411080477E-02
 0.8864155270044007      5.9298584915436968E-02
 0.9382745520027324      4.4277438817420068E-02
 0.9747285559713092      2.8531388628934019E-02
 0.9951872199970209      1.2341229799988377E-02
```

Program 2. Electron trajectories for screening model

```
c Calculates the image trajectory of an electron a distance x from a
c conductor and a distance y from another electron itself dl from the
c metal. (x is distance perpendicular to surface, y parallel). The
c electron at (x,y) feels its own image force, as well as forces from
c both the other electron and image. There is also a constant force
c f perpendicular to the surface. Calculations performed with a
c fourth order Runge-Kutta technique given in "Computer Methods for
c Mathematical Computations" by G.E.Forsythe,M.A.Malcolm,C.B.Moler.

      program integ
      external slope
c     implicit double precision (a-z)
      real*8 t,y(4),tout,relerr,abserr,m,te,pe,ke,x0
      real*8 tfinal,tprint,b,f,work(39),dl
      integer iwork(5),iflag,neqn,i
      common /block1/ b,f,m,te,pe,ke,dl,x0
      neqn=4
      b=2.307d-31
      m=9.11d-31
      write(6,15)
   15 format(' input x0,y0,vx0,vy0,dl,f :')
      read(5,25) y(1),y(2),y(3),y(4),dl,f
   25 format(6d15.8)
   26 format(2(3d15.8/))
      write(6,26) y(1),y(2),y(3),y(4),dl,f
      x0=y(1)
      t=0.d0
      tout=t
      iflag=1
      abserr =0.d0
      relerr=1.d-9
      tprint=1.d-13
      tfinal=1.d-12
      do 100 i=1,9
   10 call rkf45(slope,neqn,y,t,tout,relerr,abserr,iflag,work,iwork)
      call energy(y)
      write(6,35)t,y(1),y(2),pe,ke,te,dlog10(t),dlog10(y(1))
   35 format(' time=',e13.6,5x,' x=',e13.6,5x,'y=',e13.6,5x
     + /'   pe=',e13.6,5x,'ke=',e13.6,5x,'te=',e13.6,5x,
     + /'  lgt=',e13.6,5x,'lgx=',e13.6/)
   97 go to (80,20,30,40,50,60,70,80) iflag
   20 if (t .ge. tfinal) goto 102
      tout=t+tprint
      go to 10
   30 write(6,45)
   45 format('iflag=3')
      go to 10
   40 write(6,55)
   55 format('iflag=4')
      go to 10
   50 write(6,65)
   65 format('iflag=5')
```

Program 2, continued

```
      abserr = 1.d-9
      go to 10
   60 write(6,75)
   75 format('tolerances reset in integ3')
      relerr = 10.*relerr
      abserr=abserr+10.d0
      write(6,76)relerr,abserr
   76 format(2d15.8)
      iflag=2
      go to 10
   70 write(6,85)
   85 format('iflag=7')
      iflag=2
      goto 10
   80 write(6,81)
   81 format(14H improper call)
  102 continue
      tprint=1.d-16*1.d1**(i)
      tfinal=1.d-15*1.d1**(i)
      tout=t+tprint
  100 continue
  101 stop
      end

      subroutine slope(t,y,yp)
c     implicit double precision (a-z)
      real*8 t,y(4),yp(4),m,dl,b,f,pe,te,ke,dp,dm,da,db,x0
      common /block1/ b,f,m,te,pe,ke,dl,x0
      dp=y(1)+dl
      dm=y(1)-dl
      da=(y(2)**2+dp**2)**1.5
      db=(y(2)**2+dm**2)**1.5
      yp(1)=y(3)
      yp(2)=y(4)
      yp(3)=(b/m)*(-1.d0/(4.d0*y(1)**2)+dm/db-dp/da)+f/m
      yp(4)=(b/m)*(y(2)/db-y(2)/da)
      return
      end

      subroutine energy(y)
c     implicit double precision (a-z)
      real*8 y(4),m,dl,b,f,pe,te,ke,dp,dm,da,db,x0
      common /block1/ b,f,m,te,pe,ke,dl,x0
      dp=y(1)+dl
      dm=y(1)-dl
      da=dsqrt(y(2)**2+dp**2)
      db=dsqrt(y(2)**2+dm**2)
      pe=b*(-1.d0/(4.d0*y(1))+1.d0/db-1.d0/da)-f*(y(1)-x0)
      ke=0.5d0*m*(y(3)**2+y(4)**2)
      te=pe+ke
      return
      end
```

Program 3. Electron diffusion model

```
c This program calculates the 1-dimensional random walk of an
c electron through a series of nlay layers.  In this case the first
c and last layer represent the surface and detector, respectively.
c p,d are the population of the prompt and delayed populations,
c respectively, of each layer.  pp,pd,dd are the matrices which
c describe the transfer probability of the prompt→prompt,
c prompt→delayed, and delayed→delayed populations, respectively.

      implicit double precision (a-h,o-z)
      dimension dd(22,22),pd(22,22),pp(22,22),od(22)
      dimension op(22),p(22),d(22)
      character*9 filnam
      write(6,*)'enter filename'
      read(5,5) filnam
 5    format(a9)
      write(6,*)'enter # steps to leave laser on'
      read(5,*) lz
      write(6,*)'enter 1 to see prob. matrices or 0 to skip'
      read(5,*) ma
      nlz=1
      nlay=22
      nly2=nlay-2
      do 20 i=1,nlay
      od(i)=0.
      op(i)=0.
      p(i)=0.
      d(i)=0.
      do 20 j=1,nlay
      dd(i,j)=0.
      pd(i,j)=0.
20    pp(i,j)=0.
      do 30 i=1,nly2
      pp(i+2,i+1)=0.7
      pd(i+1,i+1)=0.3
      dd(i+1,i+1)=1./3.
      dd(i,i+1)=1./3.
30    dd(i+2,i+1)=1./3.
      pp(2,1)=1.0
      pp(nlay,nlay)=1.0
      dd(1,1)=1.0
      dd(nlay,nlay)=1.0
      k=0
      op(1)=1.0
      num =0
      open(7,file=filnam,status='new',form='formatted')
      write(7,*) 200
      if (ma .eq. 0) go to 40
      write(6,70) k,0.,(op(i),i=1,nlay)
      do 35  k=1,nlay
35    write(6,70) k,0.,(pp(k,i),i=1,nlay)
      do 36  k=1,nlay
```

Program 3. continued

```
   36    write(6,70) k,0.,(pd(k,i),i=1,nlay)
         do 37  k=1,nlay
   37    write(6,70) k,0.,(dd(k,i),i=1,nlay)
   40    do 90 l=1,200
         do 80 k=1,50
         if (num .gt. lz) go to 100
         do 60 i=1,nlay
         rp=0.
         rd=0.
         do 50 j=1,nlay
         rd=dd(i,j)*od(j) + pd(i,j)*op(j) + rd
   50    rp=pp(i,j)*op(j)+rp
         d(i)=rd
   60    p(i)=rp
         num=(l-1)*50+k
         sig=d(nlay)+p(nlay)
         dsig=sig-(od(nlay)+op(nlay))
         if (nlz .ne. 0) nel=num
         dsign=dsig/nel
         sign=sig/nel
         do 65 i=1,nlay
         op(i)=p(i)
   65    od(i)=d(i)
         op(1)=op(1)+1.0*nlz
         if (l .gt. 1 .or. k .gt. 10) go to 80
         write(6,71) num,sig,sign,dsign,(p(i),i=1,nlay)
c        write(6,71) -1,-1.,-1.,-1.,(d(i),i=1,nlay)
         if( nlz .eq. 0) write(7,*)num,dsign
   70    format(i5,5x,e12.6/,6(4(e12.6,5x)/)//)
   71    format(i5,3(5x,e12.6)/,6(4(e12.6,5x)/)//)
   80    continue
         write(6,71) num,sig,sign,dsign,(p(i),i=1,nlay)
c        write(6,71) -1,-1.,-1.,1.,(d(i),i=1,nlay)
         if( nlz .eq. 0) write(7,*)num,dsign
   90    continue
         close(7)
         stop
c  laser turned off
  100    pp(1,1)=1.0
         pp(2,1)=0.0
         nlz=0
         num=0
         lz=100000
         go to 40
         end
```

Program 4. Photoyield vs. Coverage prediction by the Topping model

```
c This program uses the Topping equation and the square dependence
c bewteen the photoyield and the work function to generate a plot of
c photoemission yield vs. coverage. Required inputs are the observed
c yield at Θ=0 in desired units, (φ - hν) in eV, the dipole moment in
c Debye, the polarizability in Å^3, and the coverage of one monolayer
c in molecules/cm^2.

      PROGRAM TOPPLT
      REAL N
      DIMENSION X(500),Y(500)
      NPTS=500
      DATA YES/'Y'/
 25   WRITE (5,30)
 30   FORMAT ('$ENTER J(0),DEL(EV) : (F12.6)  ')
      READ(5,40)Y0,DEL
 40   FORMAT (2F12.6)
      WRITE (5,50)
 50   FORMAT ('$ENTER U(D),AL(A3) : (F12.6)  ')
      READ (5,40)U,AL
      WRITE(5,70)
 70   FORMAT('$ENTER N0(/CM2) : (E12.6)  ')
      READ (5,60) N
 60   FORMAT (E12.6)
      A=2.*3.142*4.803E-10*U*1.E-18*(1./SQRT(N))
      B=N**(-1.5)
      C=9.*AL*1.E-24
      D=DEL*1.602E-12
      DO 120 I=1,500
      X(I)=(I-1)/50.
      E=B+C*SQRT(X(I)**3)
      F=A*X(I)/E
      G=(D-F)**2
120   Y(I)=(Y0/D**2)*G
125   CALL PLOTGY(500,X,Y,-1,1,0)
      WRITE (5,127)
127   FORMAT ('$DO YOU WANT TO CHANGE WINDOW VALUES?:')
      READ(5,131) ANS
      IF (ANS .EQ. YES) GO TO 125
      WRITE (5,130)
130   FORMAT('$DO YOU WANT TO CHANGE PARAMETERS: ')
      READ(5,131) ANS
131   FORMAT (A1)
      IF (ANS .EQ. YES) GO TO 25
      STOP
      END
```

This report was done with support from the Department of Energy. Any conclusions or opinions expressed in this report represent solely those of the author(s) and not necessarily those of The Regents of the University of California, the Lawrence Berkeley Laboratory or the Department of Energy.

Reference to a company or product name does not imply approval or recommendation of the product by the University of California or the U.S. Department of Energy to the exclusion of others that may be suitable.

LAWRENCE BERKELEY LABORATORY
TECHNICAL INFORMATION DEPARTMENT
UNIVERSITY OF CALIFORNIA
BERKELEY, CALIFORNIA 94720